Nano-structured Materials for Optoelectronic Devices

Guangru Li

Cavendish Laboratory

University of Cambridge

Queens' College

This dissertation is submitted for the degree of

Doctor of Philosophy

December 2015

Declaration

This dissertation is the result of my own work and includes nothing which is the outcome of work done in collaboration except where specifically indicated in the text. I declare that no part of this work has been submitted for a degree or other qualification at this or any other university. This dissertation does not exceed the word limit of 60,000 words set by the Degree Committee of the Faculty of Physics &Chemistry.

Guangru Li

December 2015

To my Family

Abstract

This thesis is about new ways to experimentally realise materials with desired nano-structures for solution-processable optoelectronic devices such as solar cells and light-emitting diodes (LEDs), and examine structure-performance relationships in these devices.

Short exciton diffusion length limits the efficiency of most exciton-based solar cells. By introducing nano-structured architectures to solar cells, excitons can be separated more effectively, leading to an enhancement of the cell's power conversion efficiency. We use diblock copolymer lithography combined with solvent-vapour-assisted imprinting to fabricate nano-structures with 20-80 nm feature sizes. We demonstrate nanostructured solar cell incorporating the high-performance polymer PBDTTT-CT. Furthermore, we demonstrated the patterning of singlet fission materials, including a TIPS-pentacene solar cell based on ZnO nanopillars.

Recently perovskites have emerged as a promising semiconductor for optoelectronic applications. We demonstrate a perovskite light-emitting diode that employs perovskite nanoparticles embedded in a dielectric polymer matrix as the emissive layer. The emissive layer is spin-coated from perovskite precursor/polymer blend solution. The resultant polymer-perovskite composites effectively block shunt pathways within the LED, thus leading to an external quantum efficiency of 1.2%, one order of magnitude higher than previous reports.

We demonstrate formations of stably emissive perovskite nanoparticles in an alumina nanoparticle matrix. These nanoparticles have much higher photoluminescence quantum efficiency (25%) than bulk perovskite and the emission is found to be stable over several months.

Finally, we demonstrate a new vapour-phase crosslinking method to construct full-colour perovskite nanocrystal LEDs. With detailed structural and compositional analysis we are able to pinpoint the aluminium-based crosslinker that resides between the nanocrystals, which enables remarkably high EQE of 5.7% in $CsPbI_3$ LEDs.

Acknowledgement

My intention to apply to Cambridge can be traced back to a plenary talk I attended in a conference in Xi'an China, which mentioned the pioneering polymer light-emitting diode invention made by the Cavendish Laboratory in 1990s. My applications finally placed me under supervision of Professor Neil Greenham, in Queens' College. I also got a scholarship from Gates Cambridge Trust to cover my full expenses during the PhD.

This period in Cambridge has been so surreal maybe due to the town's historical nature and so rewarding that I've experienced so much. My involvement in multi-culture college/Gates/department communities enriches my life and work values. My collaborations with smart colleagues on cutting-edge research have been very exciting and valuable experience.

Firstly I want to express my gratitude to Professor Neil Greenham, for accepting me as a PhD student, for offering a comfortable and safe lab environment, and for being supportive in my 4-year ups and downs of research.

Then I want to thank these who undertook the responsibility of lab maintenance. I thank Richard Gymer for patiently answering enquiries, and repairing all the sadly broken equipment. I thank Dr. Yury Alaverdyan, Duncan Bulman, and Roger Bourne for maintaining the nano-science clean room. I thank Dr. Radoslav Chakalov, Roger Beadle for assistance with lab inquiries. I thank Jean Philips, Emily Heavens-Ward and Alison Barker for ordering lab consumables.

I want to thank a few people for helping me start my PhD. Dr. Demet Asil was the trainer of my 1st-year device-fabrication training. Dr. Sven Huettner helped me set up the solvent-vapour imprinting kit. Dr. Yury Alaverdyan suggested the method of

colloidal patterning. Le Yang supplied PbSe nanocrystals and assumed relevant device work.

Then I want to thank the people who help or collaborate on a few key projects:

In the first perovskite LED project, Dr Lang Jiang provided a key polymer. Dawei Di had initial discussions with me; Jonathan Lim acquired XRD spectra; May Ling Lai synthesised methylamonium-based perovskite precursors. Dr. Zhi-Kuang Tan discussed the work with me constantly and was helpful all along. I also thank Dr. Qilei Song for supplying nano-porous polymers for testing.

On the alumina nano-particle/perovskite composite project, thanks to Dr. Zhi-Kuang Tan for his initial observation of PL enhancement in alumina-perovskite composites. The TCSPC measurement was done with Dawei Di. May Ling Lai supplied perovskite material. Jonathan Lim acquired XRD spectra.

In the $CsPbX_3$ nano-crystal LED project, Dr. Zhi-Kuang Tan initiated the project and guided and supported me all along. Nathaniel J. L. K. Davis, Tom C. Jellicoe and I synthesized perovskite material. Sai Bai synthesized ZnO nanoparticles. Florencia Wisnivesky Rocca Rivarola acquired TEM data, and analysed EELS data together with Dr. Francisco de la Peña. Dr. Shaocong Hou and I acquired FTIR data. I would also thank the Cambridge Philosophical Society for a Studentship and the Board of Graduate Studies for a Lundgren Award supporting me to finish up this project.

I want to further thank my friends in the wider Cambridge community, who have recharged me continuously in person and who I can’t list completely. The Chinese community share with me the same language and culture. The Gates Cambridge community, with its members from widely different backgrounds, has never stop surprising, inspiring and comforting me. My badminton friends have kept me excising my physical power and in good health.

Finally I want to express my gratitude to my family, especially to my parents who provided me unconditional understanding and support.

List of abbreviations and acronyms

AFM	Atomic force microscopy
ALD	Atomic layer deposition
DMF	Dimethylformamide
EELS	Electron energy loss spectroscopy
EL	Electroluminescence
EM	Electron microscope or electron microscopy
EQE	External quantum efficiency
F8	Poly(9,9-dioctylfluorene)
FWHM	Full width at half maximum
FTIR	Fourier transform infrared spectroscopy
HAADF-STEM	High angle annular dark field scanning transmission electron microscopy
HRTEM	High resolution transmission electron microscopy
ICP	Inductively coupled plasma
IQE	Internal quantum efficiency
ITO	Indium tin oxide
LED	Light-emitting diode
$MAPbX_3$	Methylammonium lead tri-halide
NMP	N-methy1-2-pyrrolidone
NP	Nanoparticle
OA	Oleic acid
OLED	Organic light-emitting diode
OLA	Oleylamine
P3HT	Poly(3-hexylthiophene-2, 5-diyl)
PBDTTT-CT	2,6-Bis(trimethyltin)-4,8-bis(5-(2-ethylhexyl)thiophen-2-yl)benzo[1,2-b :4,5-b']dithiophene
PCBM	Phenyl-C61-butyric acid methyl ester

PDI	Polydispersity index
PEDOT-PSS	Poly(3,4-ethylenedioxythiophene) polystyrene sulfonate
PeLED	Perovskite light-emitting diode
PFPE	Perfluoropolyether
PFPE-DMA	Perfluoropolyether dimethacrylate
PIP	PI2525 polyimide precursor
PL	Photoluminescence
PLQE	Photoluminescence quantum efficiency
QD	Quantum dot
QLED	Quantum dot light-emitting diode
RIE	Reactive ion etching
SEM	Scanning electron microscopy
STEM	Scanning transmission electron microscopy
TEM	Transmission electron microscopy
TFB	Poly[(9,9-dioctylfluorenyl-2,7-diyl)-co-(4,4′-(N-(4-sec-butylphenyl)diphenylamine)]
TIPS-pentacene	6,13-Bis(triisopropylsilylethynyl)pentacene
TMA	Trimethylaluminum
UV-vis	Ultraviolet-visible spectroscopy
XPS	X-ray photoelectron spectroscopy
XRD	X-ray diffraction

TABLE OF CONTENT

Chapter 1

Introduction

1.1 Motivations

1.1.1 Sustainable and green energy supply

According to energy survey of World Energy Council for the year 2013, 82% of world energy is supplied by fossil fuels [1], which accounts for 80 wt % of CO_2 emissions in the world and is the major cause of Global Warming [2]. Burning of fossil fuels also causes air, water and land pollution. Fossil fuel is a non-renewable and unevenly distributed resource, e.g. most of world's petroleum oil reserve is in Middle East [3].

Sustainable and green energy refers to biomass, solar energy, wind energy etc. Solar energy is an important energy source because the amount of solar energy reaching the earth's surface per year equates 5 times the known fossil fuel reserves and is distributed more evenly than fossil fuels over the world.

Exciton-based solar cells are made from materials that are of low cost and processed with simple steps at low temperature. In this thesis, we are interested to include nano-scale components in these cells to tackle the limitation of short exciton-diffusion length.

1.1.2 Authentic-colour presentation in low-cost display

Since the first invention of artificial display, there happens a revolution from black-white/colour CRT (cathode ray tube), LCD (liquid crystal display), LED (light-emitting diodes), e-ink (electrophoretic ink) to futuristic technology such as holographic display.

The current competitive technology to replace LCD is OLED and QLED. OLED offers perfect black (by turning off the emitting pixels) and true-to-life colour. However, the OLED displays use thermal-evaporated small molecules, and thereby are very expensive to produce uniformly in large area (The price of an OLED TV is ten times the price of LCD TV at the moment). QLED offers purer colour than OLED. However, the QLED displays use core-shell-structure quantum dots, which are synthesised by hot-injection method and are difficult to produce in large quantity and under well control.

Perovskites have recently emerged as an interesting new semiconductor for optoelectronic application. We will show in this thesis, perovskite LEDs offer the benefits of: colour purity as good as quantum dot LEDs, full-visible-colour range, efficiency comparable with some of the best QLED and OLED technology and large-scale-compatible processing.

1.2 Nanotechnology, nanoscience and their relevance to this thesis

What would the properties of materials be if we could really arrange the atoms the way we want them? They would be very interesting to investigate theoretically. I can't see exactly what would happen, but I can hardly doubt that when we have some control of the arrangement of things on a small scale we will get an enormously greater range of possible properties that substances can have, and of different things that we can do.

Richard Feynman, There's Plenty of Room at the Bottom" Dec. 29 1959.

The idea of nano was mentioned in the above speech by Feynman in 1959. The word 'nanotechnology' was firstly used by K. Eric Drexler in 1986 [1].

The Royal Society and the Royal Academy of Engineering give the definition of nanoscience and nanotechnology [4]:

“ Nanoscience is the study of phenomena and manipulation of materials at atomic, molecular and macromolecular scales, where properties differ significantly from those at a large scale.

Nanotechnologies are the design, characterization, production and applications of structures, devices and systems by controlling shape and size at the nanometre scale. ”

The sizes of nano-materials are from ~100 nm (200-2000 atoms) to below 1 nm (2-10 atoms) fabricated by different nano-manipulation techniques. The field of nanoscience/nanotechnology is flourishing and nanotechnology is now a powerhouse in the manufacturing industry.

Discoveries and inventions in nanoscience include new materials, and furthermore lead to new phenomenon and applications. For example, quantum dots [5], due to the quantum confinement effect, show high PLQE and tuneable emission colour, therefore are promising for optoelectronics application. They are also useful for drug delivery because of their small size and large surface area. For another example Nanotubes and carbon nano-fibers are used in high-end sports or construction equipment, due to their light weight and high mechanical strength [6]. Thirdly, nano-imprinting, a nano-fabrication method, is employed to fabricate nano-scale data storage device[7, 8].

In this thesis, we are specifically interested in nanomaterials applied in optoelectronics. We want to understand the desired nano-design that improves the performance of optoelectronic devices (solar cells and light-emitting diodes (LEDs)). The nano-fabrication tools used in this thesis include nano-patterning, nano-composite, nano-colloidal and atomic layer deposition. We characterized our nanomaterials by electron microscopy, x-ray diffraction and atomic force microscopy.

In chapter 2, we introduce the operation of LEDs and exciton-based solar cells. We briefly introduce the properties of conjugated polymers and singlet fission materials. We elucidate the current research status of perovskite materials for light-emitting purposes.

In chapter 3, we explain the common experimental methods used throughout this thesis.

In chapter 4, we extend nano-patterning methods to a wider range of materials, and construct prototype nano-structured solar cells. In chapter 5 we explore a one-step method to embed perovskite nanocrystals in a flexible polymer matrix for LED applications. In chapter 6, we synthesis emissive perovskite nanocrystals in an alumina matrix; in chapter 7, we study a vapour-based passivation and cross-linking effect to perovskite nanoparticle films, for LED application.

In chapter 8, we propose future work.

References

1. Frei, C., Whitney, R., Schiffer, H.-W., Rose, K., Rieser, D.A., Al-Qahtani, A., Thomas, P., Turton, H., Densing, M., and Panos, E., *World energy scenarios: Composing energy futures to 2050*. 2013, Conseil Francais de l'energie, 12 rue de Saint-Quentin, 75010 Paris (France). Publishded on website: www.worldenergy.org
2. Houghton, J.T., *Climate change 1995: The science of climate change: contribution of working group I to the second assessment report of the Intergovernmental Panel on Climate Change*. Vol. 2. Cambridge University Press, (1996)
3. Deffeyes, K.S., *Hubbert's peak: the impending world oil shortage (New Edition)*. Princeton University Press, 2008
4. Dowling, A., Clift, R., Grobert, N., Hutton, D., Oliver, R., O'neill, O., Pethica, J., Pidgeon, N., Porritt, J., and Ryan, J., *Nanoscience and nanotechnologies: opportunities and uncertainties.* London: The Royal Society & The Royal Academy of Engineering Report, 61-64(2004).
5. Leutwyler, W.K., Bürgi, S.L., and Burgl, H., *Semiconductor clusters, nanocrystals, and quantum dots.* Science, **271**, 933-937(1996).
6. Treacy, M.J., Ebbesen, T., and Gibson, J., *Exceptionally high Young's modulus observed for individual carbon nanotubes.* Nature, 381, 678-680 (1996).
7. Chou, S.Y., Krauss, P.R., and Renstrom, P.J., *Imprint of sub-25 nm vias and trenches in polymers.* Applied Physics Letters, **67,** 3114-3116(1995).
8. Chou, S.Y., Krauss, P.R., and Renstrom, P.J., *Nanoimprint lithography.* Journal of Vacuum Science & Technology B, **14**, 4129-4133 (1996).

Chapter 2

Background

2.1 Overview

Nano-structured materials are crucial in the success of the semiconductor industry. For example, the emission layer of a III-nitride LED is fabricated by inserting nanometer-thick $In_xGa_{1-x}N$ quantum wells between two wider-bandgap semiconductor layers. This configuration confines the wavefunction of electrons and holes in a very thin layer with thickness of a few nanometers, thus enables highly efficient electron-hole recombination and electroluminescence and has led to the commercialization of this class of LEDs [1, 2].

As another example, the active layer of a polymer solar cell consists of a bulk heterojunction (BHJ) that is a blend of organic semiconductors having phase-separation on the correct scale, in order to enable efficient exciton separation. Researchers have been able to realise BHJ polymer solar cells with power conversion efficiencies (PCE) of up to ~10% [3, 4][5], compared with PCE of less than 1% in planar polymer solar cells.

In this background chapter, we introduce the basics of solar cells and light-emitting diodes. We explain why we are interested in nano-structured solar cells and nano-structured light-emitting diodes. Specifically we explain the properties of halide perovskites that are newly investigated for optoelectronic applications.

2.2 Exciton-based solar cells and the role of the active layer morphology

2.2.1 Brief introduction to exciton-based materials

In exciton-based material, photo-excitation produce bound electron-hole pairs named as excitons. The excitons are bound because they have exciton binding energies larger than thermal excitation energy at room temperature. Bound excitons do not contribute to electricity generation unless they can travel to an energy-offset interface where they can be separated to make free electrons and holes.

Organic semiconductors always have large exciton binding energies because of their small dielectric constant (2-3). In low-dimension materials such as semiconductor quantum dots which have high dielectric constant, exciton binding energy is high, because special confinement enhances the columbic attraction within excitons.

Exciton-based materials include organic semiconductors, semiconductor quantum dots, and many other low-dimensional materials. They are valuable for photovoltaic applications because these materials are of low cost, easily processable or environmental friendly.

We brief introduce conjugated polymers here (more details can be found in the literature [6-11]). Conjugated polymers are polymers that consist of at least of one backbone chain of alternating double- and single-bonds. According to orbital energy theory, in an insulating polymer (Figure 2.1(A)), the carbon atoms have tetrahedrally directed sp^3 hybridised covalent bonds to the adjacent atoms, and all of the bonds are localized. In comparison, in conjugated polymers (Figure 2.1(B)) the carbon atoms bond to the neighbouring atoms by three degenerate sp^2 orbitals and a $p_z$orbital. The sp^2 orbitals consist of hybridised 2s, $2p_x$ and $2p_y$ orbitals overlapping head-to-head to form σ-bonds; the $p_z$orbital is perpendicular and to the plane of the three sp^2 orbitals, and overlaps side-to-side to form π-bonds [6]. The illustration of σ-bonds and π-bonds are shown in Figure 2.1 (C). σ-bonds are stronger than π-bonds, and are important to construct a stable backbone structure. The electrons in the π-bonds, named π electrons, can decouple from the backbone and transport along the conjugated backbones.

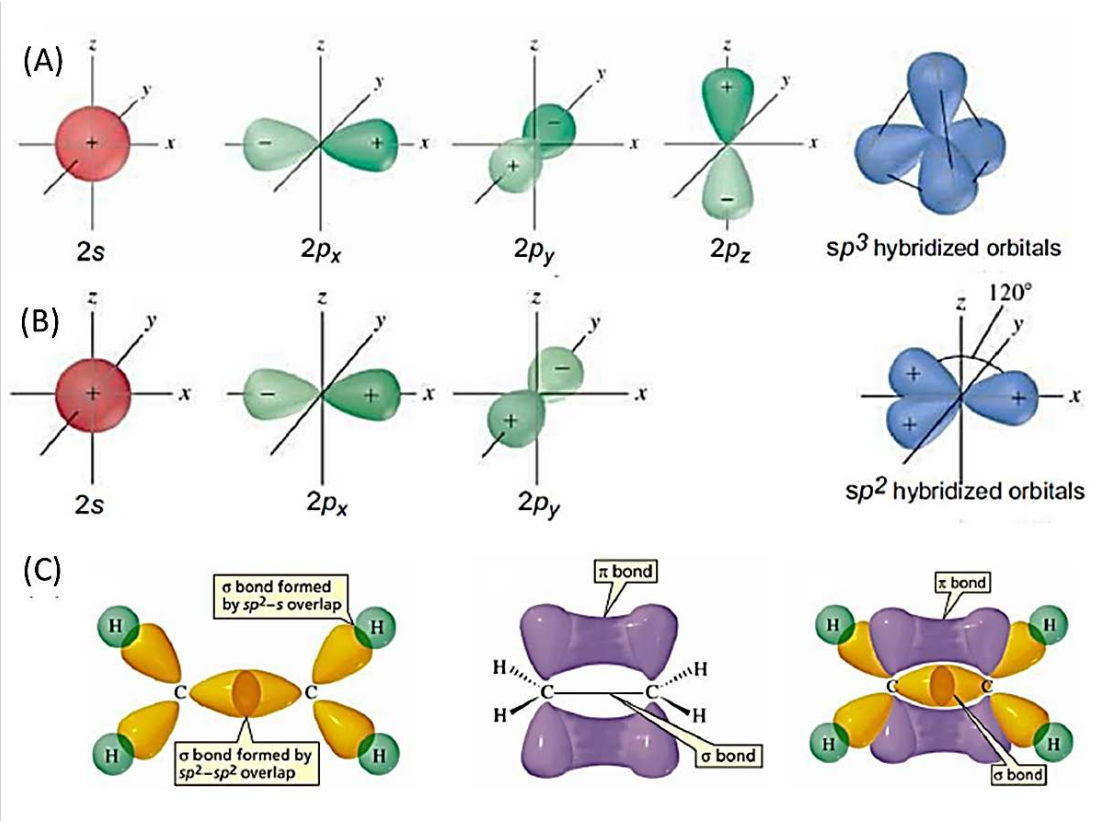

Figure 2.1 (A) Illustration of sp^3 hybridization of carbon electron orbitals. (B) Illustration of sp^2 hybridization of carbon electron orbitals. (C) Illustrations of the double bonds consisting of an σ bond formed by sp^2 orbitals and a π bond by p_z orbitals. The picture is reproduced from [10].

The electronic structure of conjugated system can be described with the Hückel Molecular Orbital (HMO) method, which uses a linear combination of atomic orbitals and molecular orbitals to determine the energy level of π electrons in conjugated hydrocarbon system. Figure 2.2 (A) illustrates the energy levels of the conjugated system at ground state. The highest fully occupied energy level by π electrons is named HOMO (highest occupied molecular orbital); the lowest unoccupied energy level is named LUMO (lowest unoccupied molecular orbital). The band gap of the conjugated polymer is defined by the difference of HOMO and LUMO. While the bandgap of a conjugated polymer can be influenced by the geometrical structure of the polymer chain, the absorption and the emission is often from the localized conjugation site named chromophore.

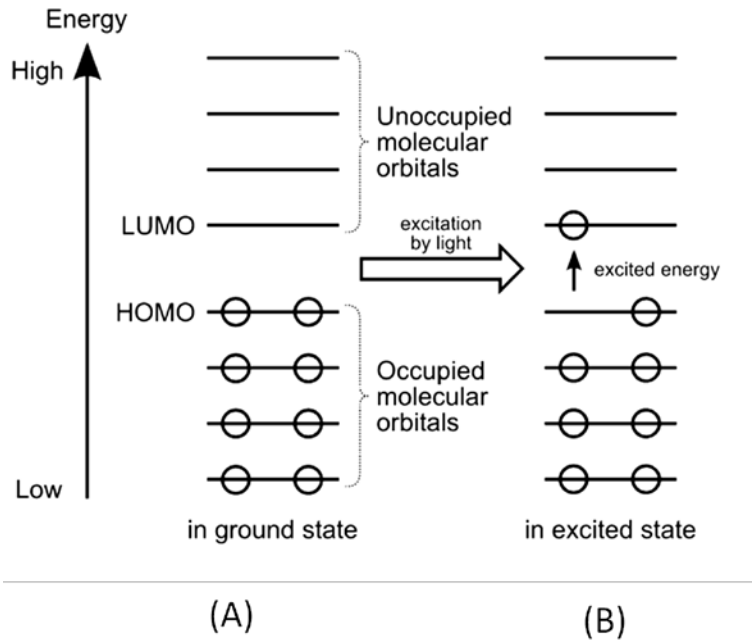

Figure 2.2 Illustration of electronic structure in conjugated system (A) at ground state; (B) at excitation state.

As shown in Figure 2.2 (B), photo-excitation in conjugated polymers promotes an electron from HOMO to LUMO and leaves a vacancy (a hole) in HOMO. The electron and the hole are bound by Coulombic attraction together, forming a quasi-particle named an exciton. Exciton can generate on a single polymer chain or across two polymer chains. Due to spin-conservation, the photo-excited excitons are singlets. Due to the low dielectric constants, excitons in polymers are tightly bonded exciton (Frenkel excitons) with binding energy of ~0.4-0.5 eV. Due to this high binding energy, the separation of excitons requires a heterojunction interface having adequate energy offset. These excitons need to diffuse to the heterojunction before being separated. There are three types of energy transfer mechanism that are responsible for exciton diffusion, cascade energy transfer, Förster transfer, Dexter transfer [12]. Cascade energy transfer involves the emission and absorption of a photon between two molecules. Förster transfer is a non-radiative energy transfer mediated by Coulombic coupling of electromagnetic field between two molecules. It only applied for emissive polymer, and the transfer occur over a length scale of 1-10 nm. Dexter energy transfer is the physical exchange of electrons, it can occur for non-radiative polymers, and usually occurs in the length scale of 0.1-1 nm. The exciton

diffusion length L_D describes the characteristic distance over which the exciton diffuse before decay, and is typically ~5-10 nm in conjugated polymers.

In optoelectronic devices, two types of heterojunctions are most used. As shown in Figure 2.3, in type I heterojunction, exciton transfer from large bandgap semiconductor to small bandgap semiconductor usually takes place; in type II heterojunction, exciton separation can happen, leaving an electron in the acceptor semiconductor and a hole in the donor semiconductor. The electron and hole, are still interacting each other, and may form a geminate pair which is named a charge-transfer (CT) state [13]. This CT state needs to compete with several processes such as non-radiative recombination and back transfer before being separated to a free electron and a free hole.

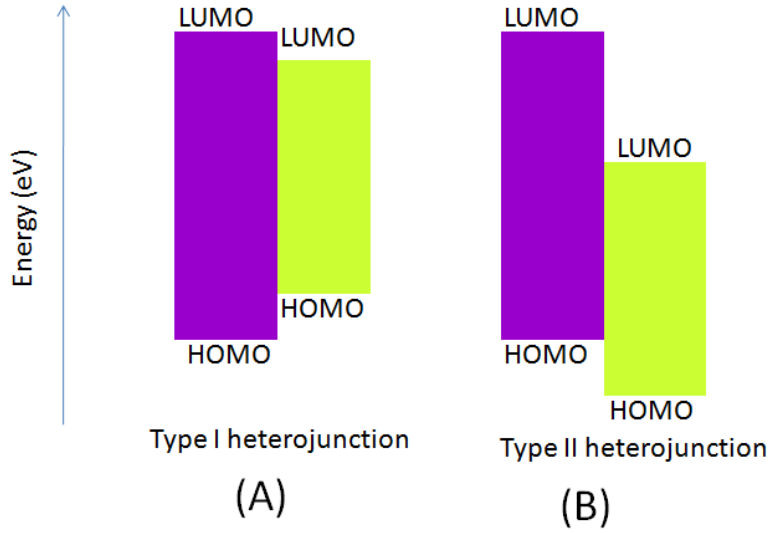

Figure 2.3 Illustration of band alignment of (A) type I heterojunction (B) type II heterojunction.

The free electrons and holes are localized on the polymer chains and their existence can result in a different chain configuration which is named a polaron. The energy of the polaron reside between the HOMO and the LUMO levels. The transport of polarons in polymer film can be described by a hopping process, in which both the charge and the chain distortion are moved [14, 15]. The free electrons and holes transported to the electrode and finally produce external current after being collected.

Conjugated polymers related to this thesis is PBDTTT-CT (See Chapter 4).

2.2.2 Singlet fission materials for solar cells

A singlet is an anti-symmetric quantum state of a system with a spin quantum number of 0, thus allowing one value of spin component; a triplet is a symmetric quantum state of a system with a spin quantum number of 1, thus allowing there are three values of the spin component, -1, 0, +1. In organic semiconductors, the dielectric constant is low, so the coulomb and exchange interactions between the electrons in the molecular orbital are significant. The former lowers the energy of a singlet or triplet both by the same amount, while the latter increases the singlet state energy and lowers the triplet state energy [16, 17], thus making the singlet energy larger than the triplet energy.

Singlet fission is a spin-allowed process in which a singlet exciton converts to two triplet states [18], as Figure 2.4 (A). Using singlet fission materials, one photon can generate two triplets, which can be separated into two pairs of electrons and holes, thus the theoretical efficiency is higher compared to conventional solar cell. Figure 2.4 (B) shows the theoretical power conversion efficiency of a single junction solar cell with singlet fission material and conventional material. Of all the singlet fission materials, pentacene is particularly interesting due to the energy of its triplet state (0.86 eV) being less than half the energy of singlet state (1.83 eV), and thus singlet fission in pentacene is more favourable. Pentacene film shows a triplet yield close to 200% and a ultrafast dynamics on a time scale of ~80 fs [19, 20]. 6,13-Bis(triisopropylsilylethynyl) pentacene (TIPS-pentacene) is a derivative of pentacene to improve its solubility. In TIPS-pentacene film, singlet fission occurs on a time scale of 1 ps with a triplet yield of 144% [21].

Because most of singlet fission material is large band-gap materials, to make full use of the solar spectrum, a tandem structure consisting of a large-band-gap singlet fission material and a small-band-gap material is usually preferred to maximize the efficiency of a singlet fission solar cell. The tandem structure is either series which the current generated from the two sub-cells needs to be matched, or parallel when the voltage produced from the two sub-cells needs to be matched. The singlet fission material is ideal for parallel tandem solar cell, because the open-circuit voltage is appropriate half of the bandgap in singlet fission cell, which makes it easier to match the voltage from the small-band-gap cell. As Figure 2.4(B) shows, either

type of a singlet fission tandem solar cell has an efficiency limit of ~45%, comparing to a non-singlet-fission single junction cell with an efficiency limit of ~33%.

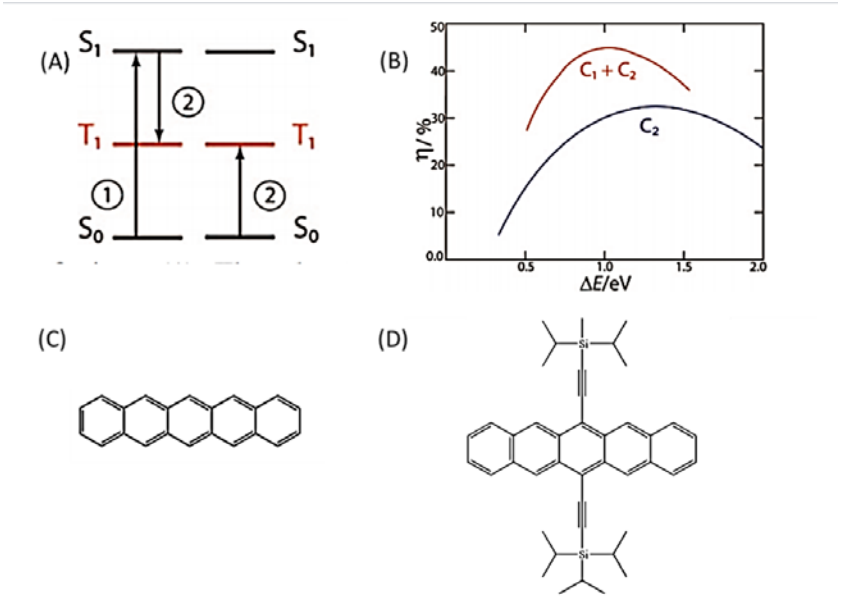

Figure 2.4 (A) Singlet fission ① the chromophore on the left undergoes an initial excitation to S_1; ② the excited chromophore share its energy with the one on the right, creating a T_1 on each other. (B) Theoretical efficiency as a function of the absorbance-material band gap for singlet fission solar cell (red curve) and conventional solar cell (blue curve). C_2 refers to traditional materials, C_1+C_2 refers to using singlet fission materials C_1 to absorb short wavelength light, and C_2 to absorb other wavelengths. The graphs are reproduced from [18]. Chemical structure of (C) pentacene, (D) TIPS-pentacene.

2.2.3 Principles of solar cells and active layer morphology

A photovoltaic solar cell is a device that converts energy of the incoming light directly to electricity by the photovoltaic effect. The device structure of a typical bi-layer organic solar cell is illustrated in Figure 2.5(A). The top electrode is a high workfunction metal such as indium tin oxide (ITO), silver and gold. The donor and acceptor materials are selected to form type II heterojunction at the interface (Figure 2.5(B)). The bottom electrode is a low work-function metal such as aluminium and calcium. The energy diagram is shown in figure 2.5 (B). Excitons are first excited by the incoming light. They are bound until they reach the donor/acceptor interface, where they separate via CT states into free electrons in the acceptor and free holes in

the donor. The free electrons and the free holes then transport through the acceptor and donor pathways respectively to the electrodes, and thus become an output current.

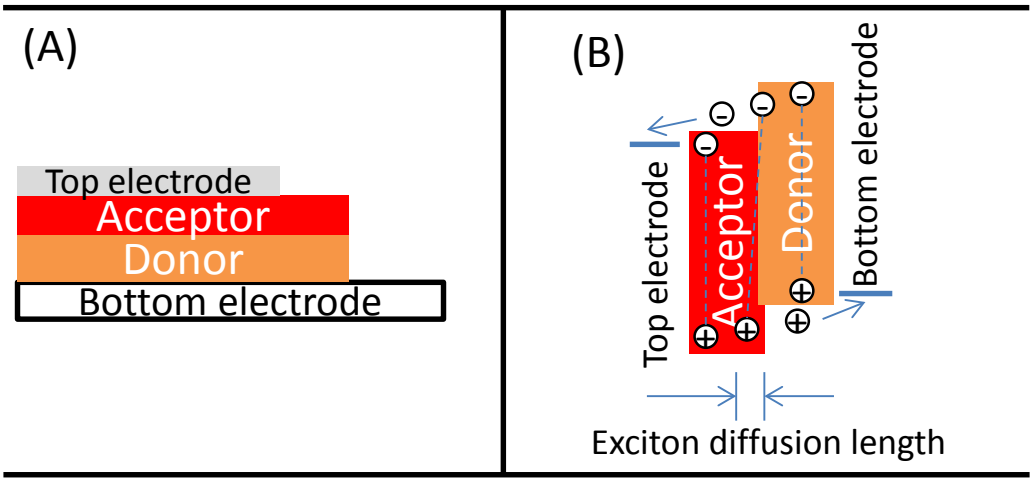

Figure 2.5 (A) Device structure of a bilayer solar cell. (B) Energy diagram of a bilayer solar cell.

The performance of a photovoltaic solar cell is evaluated by these parameters: open-circuit voltage (V_{oc}), short-circuit current (I_{sc}), fill factor (FF), power conversion efficiency (PCE) and external quantum efficiency (EQE). A typical light I-V curve of a solar cell is shown in Figure 2.6(A). Three parameters are defined on this curve: V_{oc}, I_{sc} and FF. The PCE is given by the following equation:

$$\mathrm{PCE} = \frac{\mathrm{I_{SC}} \times \mathrm{V_{OC}} \times \mathrm{FF}}{\mathrm{P_{in}}},$$

where $\mathrm{P_{in}}$ is the power of the incoming light, $\mathrm{FF} = (\mathrm{I_{MPP}} \times \mathrm{V_{MPP}})/(\mathrm{I_{SC}} \times \mathrm{V_{OC}})$, and MPP is the operation point that gives maximum output power.

EQE is defined by the percentage of incoming photons that are converted to output current. It is measured as a function of wavelength, and a typical EQE spectrum is illustrated in Figure 2.2 (B).

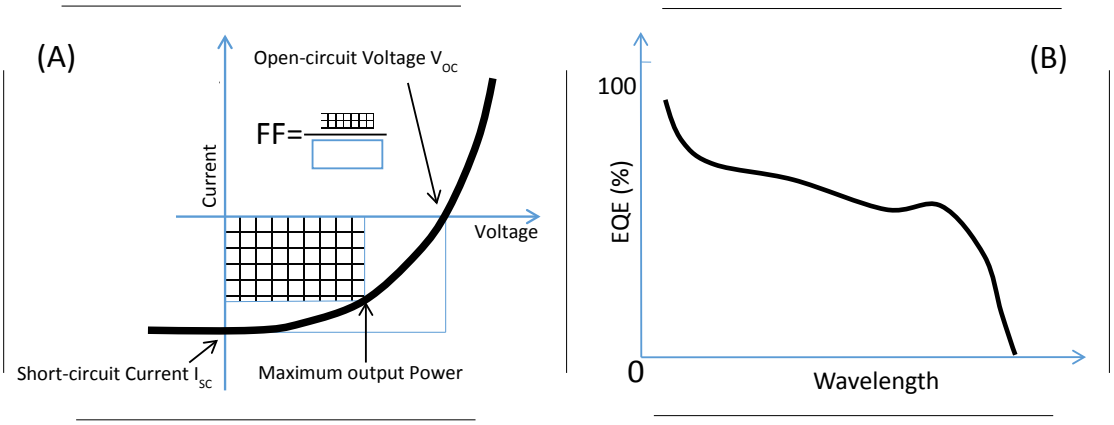

Figure 2.6 (A) Illustration of a current-voltage curve of a solar cell. (B) Illustration of an EQE spectrum of a solar cell.

In most exciton-based solar cells, the exciton diffusion length (~5 nm) is shorter than the light absorption length. In a bi-layer solar cell with thickness matching the absorption length, photo-generated excitons tend to recombine and are lost before reaching the interface. To tackle this limitation, the bulk heterojunction was invented [22]. Donor and acceptor materials are blended to form the active layer, in order to increase the chance of excitons reaching donor/acceptor interfaces. The morphology of the donor and acceptor components in the active layer strikingly influences the performance of polymer solar cells [23]. An ideal active layer should have a donor/acceptor morphology with phase-separation on the correct scale, to allow photo-generated excitons to transport to interface within the distance of exciton diffusion length. Figure 2.7 (A) shows a self-assembled bulk-heterojunction morphology formed by spin-coating from a donor/acceptor blend solution. It forms a disordered morphology, but this approach has been very successful and is able to realise almost 100% internal quantum efficiency in a PCDTBT/$PC_{70}BM$ device [5]. Figure 2.7 (B) shows an ordered bulk-heterojunction. In an ideal morphology, the domain sizes d_1 and d_2 are smaller than twice the exciton diffusion length, and the thickness T matches optical absorption length of the film.

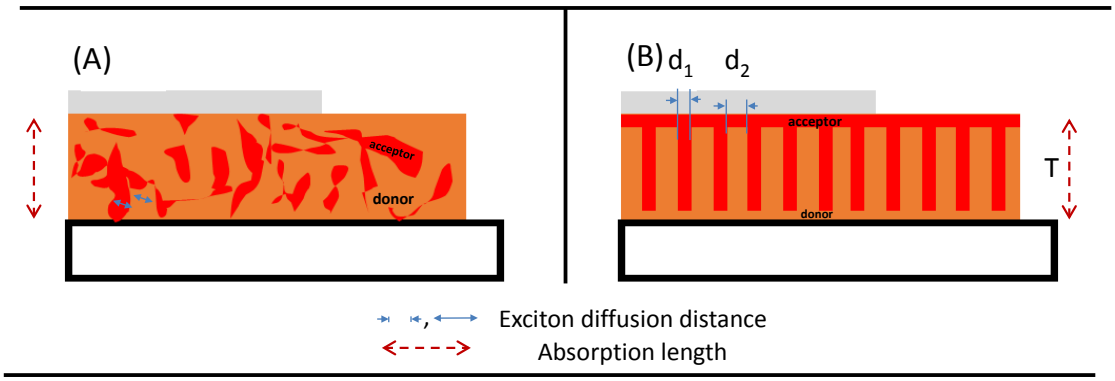

Figure 2.7 (A) A solar cell with self-assembled bulk heterojunction. (B) A solar cell with an ordered heterojunction.

The ordered heterojunction has drawn interest because the domains sizes are formed in a controllable way [24-26]. So far, most previous reports are with P3HT/PCBM solar cells, and no reports have used high-performance polymers such as PBDTTT. Moreover, for singlet fission solar cells, ordered heterojunctions are of particular interest. In singlet fission materials, a photon is absorbed first by exciting a singlet exciton state, before the singlet splits into two triplets. Then the triplet diffuses to a donor/acceptor interface, before separating into free carriers [18, 27]. Singlet fission solar cells have similar limits as polymer solar cells, namely, the triplet diffusion length does not match the absorption length even though triplet diffusion length is longer [27]. So far neither bi-layer structures nor self-assembled bulk-heterojunction structures solve this limit well in singlet-fission solar cell [28-31]. Therefore, solving this limit by ordered heterojunctions having controlled domain sizes are attractive.

2.2.4 Nanoimprinted solar cells

Nanoimprinting lithography is a method to fabricate nanoscale patterns, and is regarded as having high patterning resolution (<10 nm), high-throughput and good fidelity. Thus it is suitable to fabricate the active layer in ordered heterojunction solar cells and also able to nano-structure electrodes and charge-transport layers. Nanoimprinting lithography creates patterns by mechanical deformation of the imprint resist. The processes of a thermal imprinting are shown in Figure 2.8. A standard template which has predefined topological patterns is brought into contact

with the polymer film. The polymer is heated up above its glass transition temperature, when the stiffness of the polymer film decreases to appropriate value (Figure 2.8(A)). Then a certain pressure is applied to the template for a period of time to allow the template pattern pressed into the polymer. After being cooled down, the template is released and it leaves inverted patterns in the polymer film. To make a solar cell, another material can be then coated on the patterned film by spin-coating.

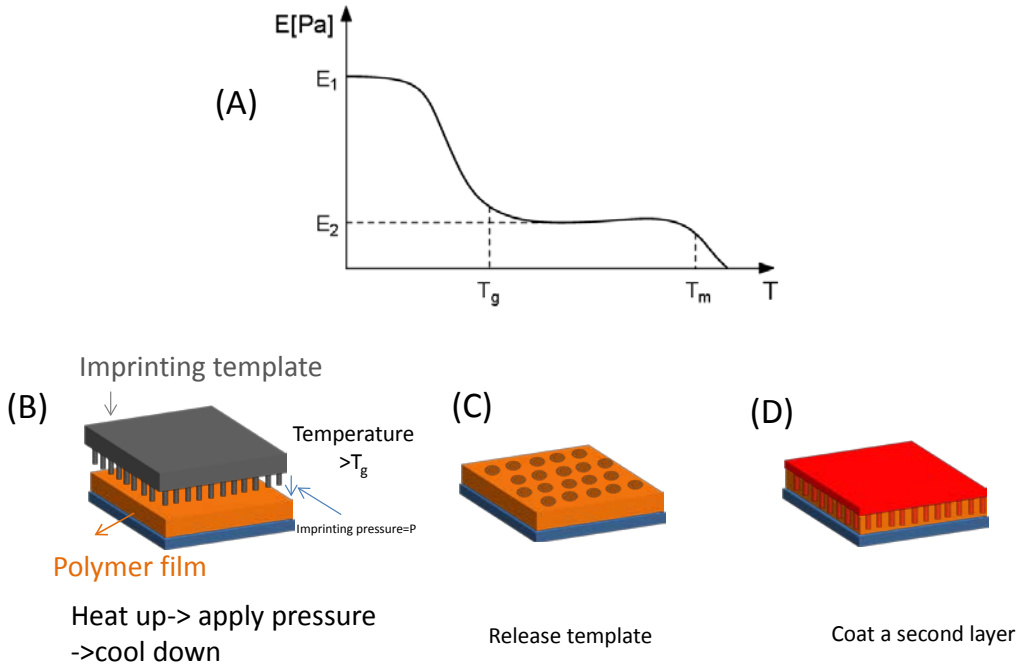

Figure 2.8 (A) Stiffness of a polymer as a function of temperature. T_g is the glass transition temperature, T_m is the melting temperature. Illustration of (B) thermal imprinting process (C) a film fabricated by thermal nanoimprinting (D) ordered heterojunction by coating a second layer on an imprinted film.

Many reports have covered different methods to imprinting P3HT, mostly using thermal imprinting [26, 32]. So far no reported have tried imprinting high performance polymers. What is more, for singlet-fission, no reports on nano-imprinted singlet fission solar cells have been done so far.

2.3 Working principles of light-emitting diodes (LEDs)

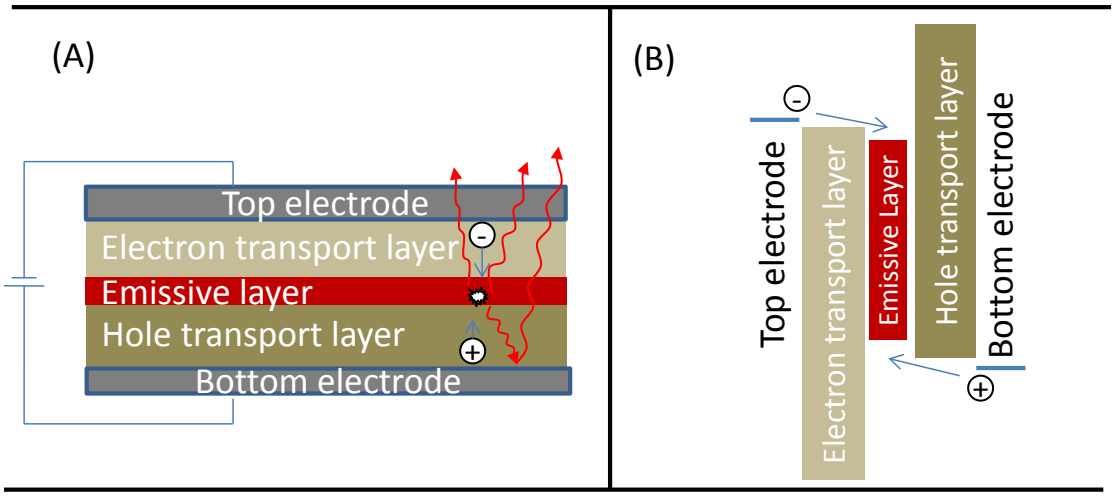

Figure 2.9 (A) Device structure of a light-emitting diode (B) Energy diagram of a light-emitting diode

A LED is a device that emits light when electrons and holes encounter and radiatively recombine in the active layer. A typical LED device structure is shown in Figure 2.9(A). The top electrode consists of a low workfunction metal; the hole-injection layer comprises a wide band-gap and high HOMO level semiconductor; the electron-injection layer comprises of wide band-gap and low LUMO level semiconductor; and the bottom electrode is made from a high workfunction metal. The injection layers also act as blocking layers that prevent charges and excitons escaping from emissive layer [33].

The LED active layer is where light is generated. Different active-layer configurations are used in different classes of LEDs. A single-layer polymer film is used in a polymer LED [34]. A large-band-gap semiconductor doped with a small-band-gap semiconductor used a host-guest small-molecule LED [35]. A thin film of quantum dots is used in a quantum dot LED (QLED) [36]. Finally the perovskite LED (PeLED), using various configurations of perovskite semiconductors in the active layer, will be investigated in this thesis [37, 38].

To be noticed, these sandwich structures are different from these in inorganic LEDs, which are P-N, P-I-N or MQW structures. In these exciton based LEDs, no spatial or quantum confinement is purposely incorporated, thanks to the natural

confinement in excitons; in addition the reason for no P-N junction is the difficulty to dope organic materials and form sharp P-N organic junctions.

Emission Spectrum: The emission spectrum describes the energy distribution of the LED emission over different wavelengths. It influences the energy efficiency of a LED. Natural sunlight contains a broad spectrum that covers ultra-violet (UV), visible and infrared (IR). Early artificial lighting–incandescent light and fluorescent light contain significant IR radiation, leading to a waste of energy. Newly invented GaN white LEDs, organic LEDs (OLEDs) and quantum dot LEDs (QLEDs) do not have UV and IR emission, making them very energy-efficient [39]. Emission spectrum also determines the visual perception of the light. In an artificial display, the colour space is generated by mixing three prime colours. It is importance to have single-colour LEDs with sharp spectra. Prime colours with sharp spectra are able to deliver better colour saturation and mix into richer group of colours. Moreover, a single-colour light source is important to enable generations of prime colours with no need for filters, thus enhancing energy usage efficiency.

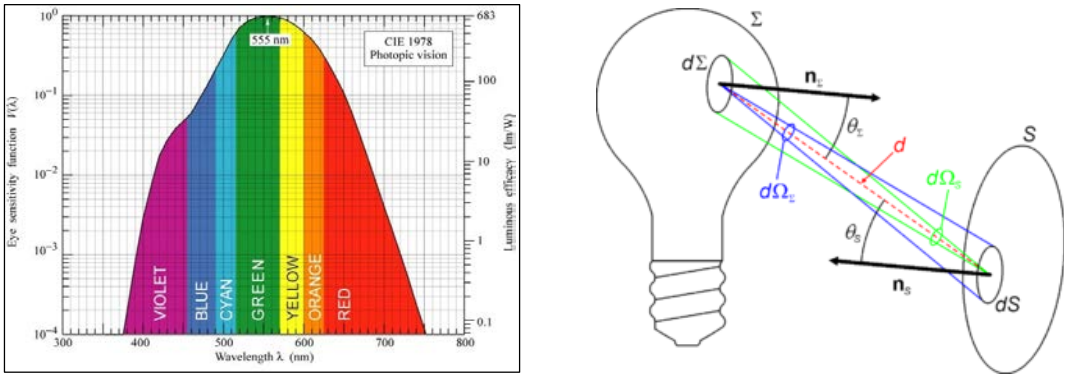

(A) (B)

Figure 2.10 (A) Luminous function (reproduced from [40]). (B) Parameters and configurations to define the luminance, reproduced from [41].

External quantum efficiency (EQE): The EQE of a LED refers to the ratio of the total number of emitted photons to the number of electrons passing through the external circuit.

Luminance function: luminous function describes the average spectral sensitivity of visual perception of brightness. It is based on subjective experiments in which the brightness of different-colour light is judged by participants. The CIE luminosity

function is shown in Figure 2.10 (A), and it is a standard function established by the Commission Internationale de l'Éclairage (CIE).

Luminance flux: luminous flux the visual perception of the brightness of light and it is calculated from the luminance function and the light spectrum.

$$\Phi_v = 683 \int_0^{\infty} \bar{y}(\lambda) \frac{dP_e(\lambda)}{d\lambda} d\lambda \,,$$

where I_v is the luminous intensity in candelas (cd), P_e is the radiant power in watts W, $\bar{y}(\lambda)$is the standard luminosity function.

Luminance: Luminance describes the visual brightness generated from a unitary light source area. Luminance is defined by luminous power per unit solid angle per unit projected sources. The configuration to calculate luminance is shown in Figure 2.10 (B), and the definition is

$$L_v = \frac{d^2\Phi_v}{d\Sigma d\Omega_\Sigma cos\theta_\Sigma}$$

Where L_v is the luminance (cd/m^2), $d^2\Phi_v$ is the luminous flux leaving the area in any direction contained inside the solid angle $d\Omega_\Sigma$. $d\Sigma$ is an infinite small area of the light emitting source, θ_Σ is the angle between the normal n_Σ to the surface $d\Sigma$ and the specified direction.

Colour and the CIE diagram: Colour is perceived by human in the follow steps: light is incident into eyes which causes the response of three kinds of cone receptors (S (short wavelength), M (medium wavelength), L (long wavelength)) on the retina; The receptors generate three neuron-signals from the three cone receptors respectively; finally the signals are transmitted to the vision zone in brain for processing. As long as the spectra of light causes the same neural responses in the receptors, human perceive the light as the same colour. Two spectra in the same colour are named metamers.

Industry uses a standardized colour diagram called CIE diagram, as shown in figure 2.11. The edge of the CIE diagram consists of the coordinates of the light at

different wavelength generated from the monochromator, and corresponds to the colours with the best purities and saturations. The colour inside the diagram is defined by the mixture of the colours from the monochromator at different ratios. In the lighting industry, colours for a display are usually generated by three primary coloured light sources. After having the coordinate of primary colour in the CIE diagram, by mixing the primary colours in different ratios the colour in the triangle constructed by the primary colours can be realised. This triangle constructed by the three primary colours is named gamut. Standard colour spaces, such as CIE 1931 XYZ, RGB, use different primary colours, thus display different ranges of colours.

Having known the spectrum of a light, its CIE coordinate can be calculated from its spectrum and the response function. The coordinate consists of X, Y and Z, where X+Y+Z=1. The HUE of a colour refers to the dominant emission wavelength, and is quantified by extend the CIE coordinate from the middle point E (0.333, 0.333) to the CIE diagram edge. As shown in the figure the HUE of an InGaN green LED is 520 nm. Another important property of a colour is its saturation or purity, which is quantified by its distance to the CIE diagram edge. In Figure 2.11, the black dots indicate the CIE coordinates of a group of blue, green and red LEDs. Compared to the green InGaN LED (0.156, 0.700), these coordinates are closer to the edge, meaning that they have better colour purities. The triangle formed by the black dots shows the colour space of these three prime colours.

Although we mainly talk about display, it is worth to mention that for lighting application the temperature of a light is important. The temperature of a colour is quantified by finding the nearest Planckian locus (back body radiation curve) point to this colour’s CIE coordinate.

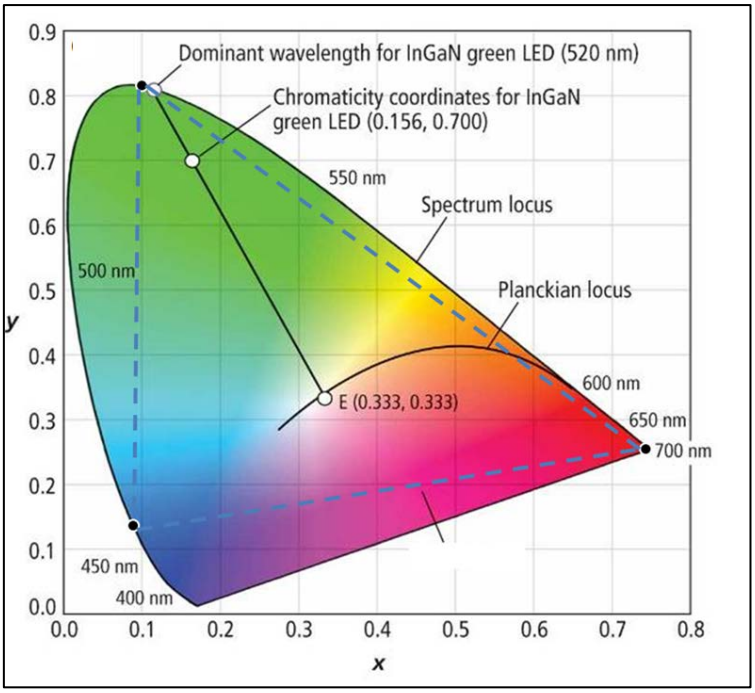

Figure 2.11 CIE diagram (reproduced from [39]).

The state-of-art display technology that offers the best colour purity is quantum dot LED (QLED), which can provide very sharp spectrum that is tuneable over the entire visible range. However, the precursors to make these quantum dots are expensive and the quantum dots require a core-shell structure which is synthesized under intricate control condition. In addition, the blue cadmium based quantum dot faces photo-oxidation problem. These challenges have hindered these quantum dots from commercial use.

2.4 Halide perovskites

2.4.1 Overview of perovskite materials

A natural mineral, in the formula $CaTiO_3$, was first discovered in 1839 and named perovskite. (Figure 2.12 (A) (B)). Nowadays perovskite broadly refer to materials sharing the similar perovskite crystal structure. These materials includes 3D perovskites (ABX_3), 2D perovskites (with infinite 2D slabs of the ABO_3 type structure separated by some motif, with formula $A_{n-1}B_nO_{3n+1}$) [37] and double perovskites (with a double-size unit cell compared to 3D perovskite) [42].

Inorganic perovskites (ABO_3) have been researched for decades. They show a rich variety of new interesting properties including superconductivity [43, 44], piezoelectricity [45], magneto-resistance [42, 46], ferromagnetic [47], ionic conductivity [48].

The pioneering work on solution-processed perovskite semiconductor was done by Mitzi et al. [49]. Halide perovskite (ABX_3, X=I, Br, Cl), especially methylammonium lead halide was found to exhibit high performance in photovoltaics in 2009 at ~4% then 2012 at ~10%[50, 51], after which a surge of research interest come up worldwide

The first light-emitting diode based on perovskite was reported by Era et al. [37], who observed strong green emission under liquid nitrogen temperature and with a layered perovskite. The first perovskite LED operated at room temperature was reported in 2014 by Tan et al. [38].

2.4.2 Perovskite crystal structure and perovskite stability

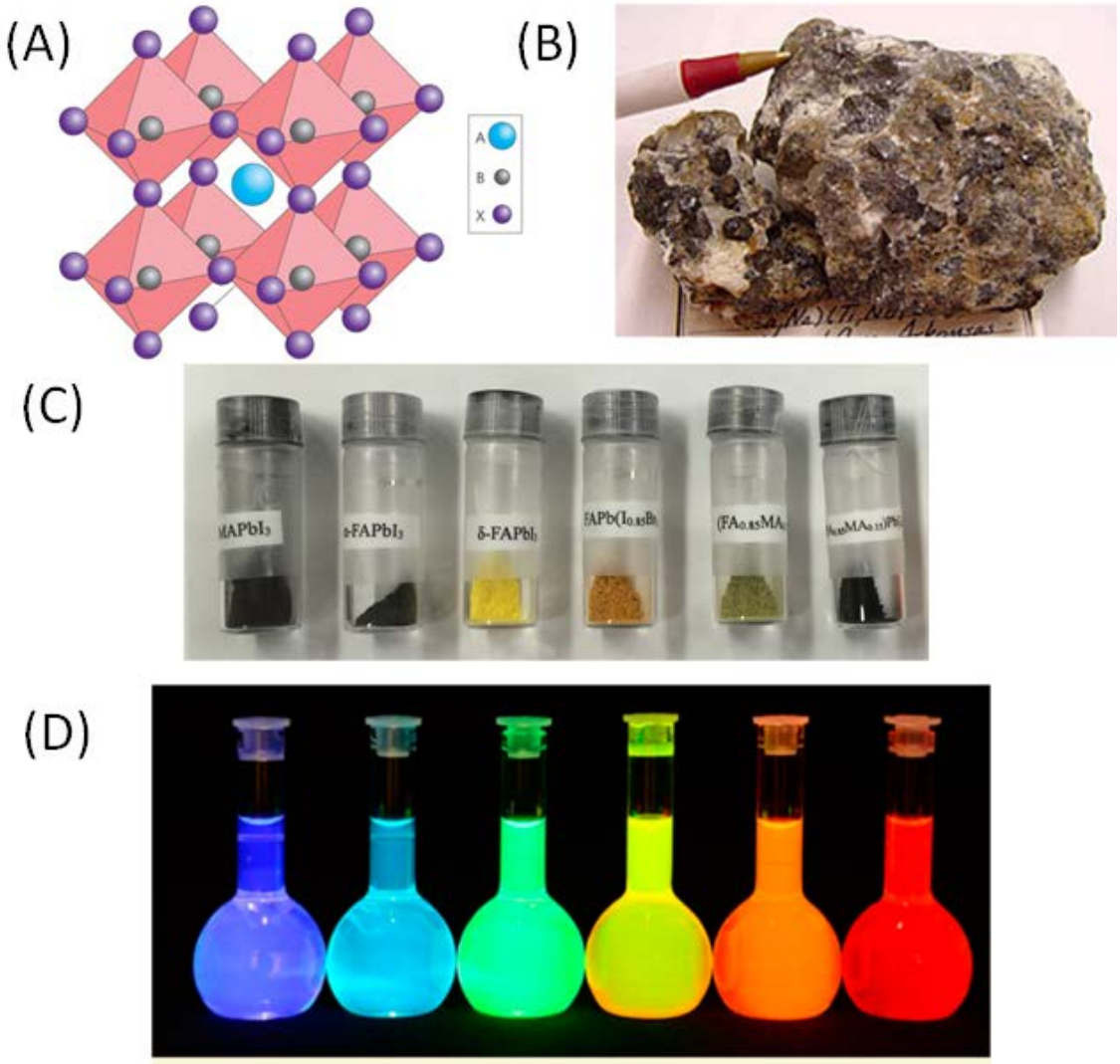

Figure 2.12 (A) Illustration of the crystal structure of ABX_3 perovskite [52]. (B) Photograph of a $CaTiO_3$ perovskite crystal. (C) Photographs of inorganic-organic hybrid halide perovskite powders [53]. (D) Photographs of $CsPbX_3$ (X=I, Br, Cl) quantum dot dispersions [54].

The most common 3D perovskite structure ABX_3 is a cubic structure, as shown in Figure 2.12 (A). It consists of an extended framework of corner-sharing BX_6 octahedra with the 'A' cation occupying the central site which is surrounded by 12 nearest-neighbour 'X' ions. Photographs of three types of perovskites, $CaTiO_3$, organic-lead halide perovskites and caesium lead halide nanocrystals, are shown in Figure 2.12 (B), (C) and (D), respectively.

The ability of the A, B and X ions to crystalize into a stable 3D perovskite structure is evaluated by the Goldschmidt tolerance factor *t* and octahedral factor μ:

$$t = \frac{r_A + r_X}{\sqrt{2}(r_B + r_X)},$$

$$\mu = \frac{r_B}{r_X},$$

where r_A , r_B and r_X are the ionic radii of A, B and X, respectively.

For halide perovskite, a stable structure meets the condition: $0.81 < t < 1.11$, $0.44 < \mu < 0.90$.An ideal cubic structure is expected to form when $0.9 < t < 1$; low symmetry structures such as tetragonal, rhombohedral, hexagonal or orthorhombic can be formed when $0.7 < t < 0.9$.

Although many ions can fit into the perovskite structure ($A=CH_3NH_3^+$, $NH_2\text{-}CH=NH_2^+$, Cs^+, Rb^+, $M=Pb^{2+}$, Sn^{2+}, Ge^{2+}, Co^{2+}, Fe^{2+}, Mn^{2+}, Cu^{2+}, Ni^{2+}, $X=Cl^-$, Br^-, I^-, F^-), only a few of the combinations are structurally stable. The structurally stable perovskites need to be chemically stable in atmospheric conditions to be useful. For example, Sn- and Ge-based perovskites readily degrade in air [55-57]. Of the halide perovskites, iodine- and chloride-based perovskites are relatively sensitive to air and water, while bromide-based perovskites are more stable.

2.4.3 Perovskite research for optoelectronics applications

Among all the perovskites, methylammonium lead halide perovskites ($MAPbX_3$, X=Cl, Br, I) have drawn tremendous interest due to the discovery of their photovoltaic performance that is comparable to silicon solar cells. The first incorporation of these materials into solar cells was reported by Miyasaka et al. in 2009, and they achieved 3.8% PCE in a dye-sensitized solar cell using perovskite as a dye [50]. In 2012, breakthrough was made by Snaith's group; they deposited $MAPbI_xCl_{3-x}$ in alumina scaffold and used a solid-state hole transporter spiro-OMeTAD; a PCE above 10% was realised. They demonstrated perovskite here was a high-quality electron-transport material. Later the same group reported that alumina or TiO_2 scaffolds are not necessary in efficient perovskite solar cells, and a mere planar device is adequate to realise PCE of above 15%, indicating perovskite can be a high-quality ambipolar semiconductor [58]. Up till now, a certified 20.1% PCE perovskite solar cell have been realized [59].

First report of electroluminescence in perovskite was done by Era et al. in 1994 [37] at liquid-nitrogen temperature with a layered perovskite compound $(C_6H_5C_2H_4NH_3)_2PbI_4$ in emissive layer. First room-temperature electroluminescence was reported by Tan et al. in 2014 with 3D lead halide perovskites [38]. Thin emissive layer was found crucial toward high perovskite-LED efficiency and EQEs of 0.75% and 0.1% were realised in a $CH_3NH_3PbI_xCl_{3-x}$ and a $CH_3NH_3PbBr_3$ LEDs, respectively. In parallel with LED work, optical pumped perovskite lasers were reported by Deschler et al. [60] and Xing et al. [61].

2.4.4 Optoelectronic properties of $MAPbX_3$ perovskite

$MAPbX_3$ perovskites are direct bandgap semiconductors with bandgaps tuneable from 1.6 eV ($MAPbI_3$) to 3.1 eV ($MAPbCl_3$)by changing halide compositions, as shown in Figure 2.13(A)(B). $MAPbI_3$ perovskites have larger absorption coefficient compared with silicon, while optimized $MAPbI_3$ solar cell have an absorption layer of ~500 nm much thinner than in planar silicon solar cell (several microns). The excitons are 3D Wannier type in $MAPbI_3$ and $MAPbBr_3$ perovskites with a binding energy of 10-100 meV, making the exciton likely to dissociate at room temperature [62]. The effective electron mass in $MAPbI_3$ perovskite is $0.1m_e$ [62]. The $MAPbI_xCl_{3-x}$ have minority-carrier lifetimes of up to 280 ns, charge carrier diffusion lengths of 100-1000 nm and charge mobilities over 20 $cm^2V^{-1}s^{-1}$ [63, 64], comparable to the best single-crystal semiconductors [65].

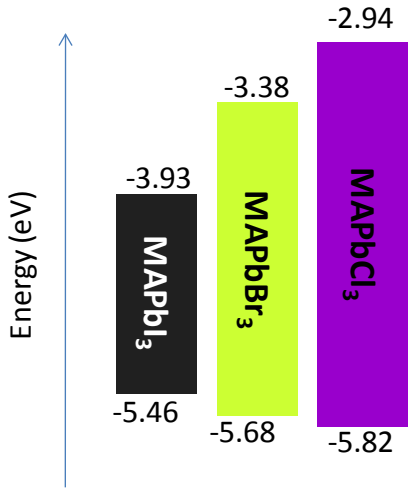

(A)

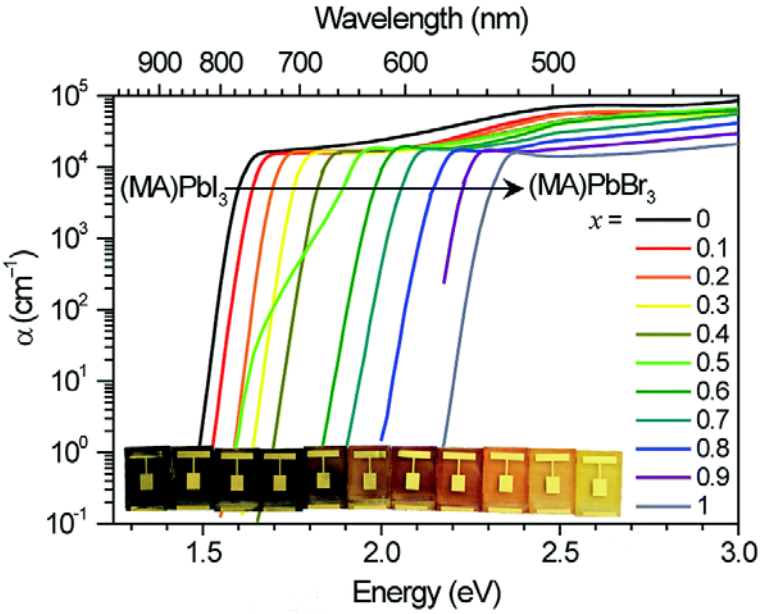

(B)

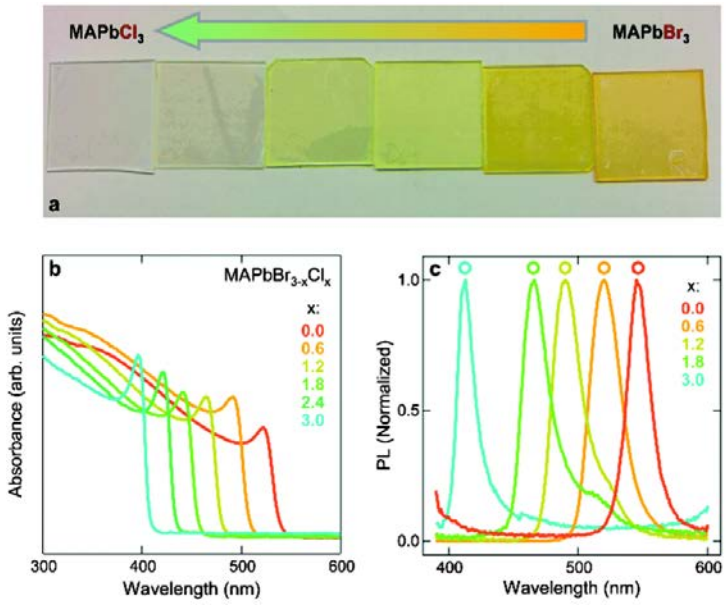

(C)

Figure 2.13 (A). Band alignments of $MAPbX_3$ perovskites [66, 67]. (B) Absorbance spectra and photographs of mixed-halide $MAPbBr_3I_{3-x}$ perovskite films [68](C) a. photographs; b. absorbance spectra; c. photoluminescence spectra of mixed $MAPbBr_3Cl_{3-x}$ perovskite [69]

The main defects in $CsPbI_3$ perovskites are point defects that mainly form shallow donors and acceptors and do not damage the transport in perovskite. [70-73] Apart from the lattice defects, morphological defects are also studied. One report said

phase inhomogeneity such as PbI_2 and CH_3NH_3I domains in the $CH_3NH_3PbI_3$ reduce charge lifetime [74]; however another report said these PbI_2 domains passivate the electronic defect on the $CH_3NH_3PbI_3$ crystal [75].

Ions in lead halide perovskite are mobile. The activation energy of MA^+, Pb^{2+} and I^- were reported to be 0.84, 2.31, 0.58 eV [71], indicating that MA^+ and I^- are very likely to move around in crystal lattices. Under electrical filed, the movement of MA^+ and I^- is able to form a macroscopic dipole in opposite direction to the external electrical field [76]. This ion mobility cause a lot of more phenomena in perovskite, such as photo-induced giant dielectric constants [77], switchable photovoltaic effect [78], photo-induce absorption shift [68] and the well-known photovoltaic hysteresis [79].

Photoluminescence in perovskite materials was reported as early as 20 years ago in ABO_3 type perovskite [37, 80-82]. Lead halide perovskites are direct-band-gap semiconductors. Their band-gap conveniently tuneable from infrared to near UV by changing their halide compositions (X=Br, I, Cl). The excitons in lead halide perovskite are 3D Wannier type with a binding energy of 10-100 meV and Bohr radius around 2 nm [83] or 5 nm [62]. For nanostructured perovskite, such as sub-10 nm $CH_3NH_3PbBr_3$ nanocrystals, the exciton binding energy was reported to be more than 300 meV [84] and is partially the reason for the crystals' high PLQE.

The emission spectrum of lead halide perovskite is surprisingly sharp for materials prepared by a simple solution spin-coating method. Full widths at half maximum (FWHMs) of their electroluminance emission spectra (tens of nm) are much smaller than polymer LEDs, and comparable to inorganic quantum dot LEDs [85].

Although photoluminescence efficiencies of most perovskite films are from 1% to 20%, the PLQE of a bulk perovskite film is close to 100% at low temperature and high excitation power density [86]. PL lifetimes are sensitive to the degree of surface passivation [87, 88]. High PLQE of 90% at room temperature and low excitation power was realized recently in perovskite quantum dots dispersed in organic solvent, the quantum dots have sizes less than 10 nm and surfaces passivated by organic ligands [89, 90]. The photoluminance properties relate closely to the crystallization condition which is realized by different preparation methods. The

emission is blue-shifted and more efficient in nano-size perovskites [54, 91-93], compared to macro-size perovskites [94-96].

2.4.5 Synthesis of $MAPbX_3$ perovskite

General synthesis routes for perovskite were developed decades ago [97]. For halide perovskites, the following routes are used:

- Preparation of $CH_3NH_3PbI_xCl_{3-x}$ by spin-coating from precursor solution (Figure 2.14 (A)):

  CH_3NH_3I and $PbCl_2$ at a weight ratio of 3:1 are dissolved in DMF by stirring overnight. Perovskite films are prepared by spin-coating, followed by annealing in a glovebox for 1 hour. This method is fast and convenient, but prone to form cracks in films. Recent reports used methods such as solvent treatment or hot spinning to improve the continuity of the spin-coated films [95, 98, 99].

- Preparation of $CH_3NH_3PbI_3$ by co-evaporation (Figure 2.14 (B)):

  CH_3NH_3I and PbI_2 are put into two crucibles and loaded in the thermal sources in a vacuum evaporator. The two sources are evaporated together to deposit a mixture of the two precursors in films. The films are then annealed at 100 ℃.

- Preparation of $CH_3NH_3PbI_3$ by sequential deposition [100] (Figure 2.14 (C)):

  PbI_2 dissolved in DMF is first spin-coated and dried on a substrate. Then CH_3NH_3I dissolved in isopropanol are dropped on top and stayed for a few minutes before being washed off by isopropanol.

- Preparation of $CsPbX_3$ (X=Cl, Br, I) colloidal nanocrystals by hot injection metho*d* [54, 101, 102] (Figure 2.14 (D)):

  In a typical process, Caesium-oleate solution in ODE is prepared by heating under nitrogen for 1 hour at 120 degree. PbX_2 dissolved in ODE with oleic acid and oleylamine as stabilizers are prepared by heating up at 100 ℃at vacuum for 1 hour. The PbX_2 solution is heated up to 170 ℃ under nitrogen, before Caesium-oleate solution at 80 ℃ is injected into it. The reaction is

finished in a few second. Excessive ligands are washed away by repeated precipitation and redissolution of the crystals. Purified nanocrystals are dispersed in suitable solvent. A detailed procedure to synthesise $CsPbX_3$ nanocrystals can be found in Chapter 3.

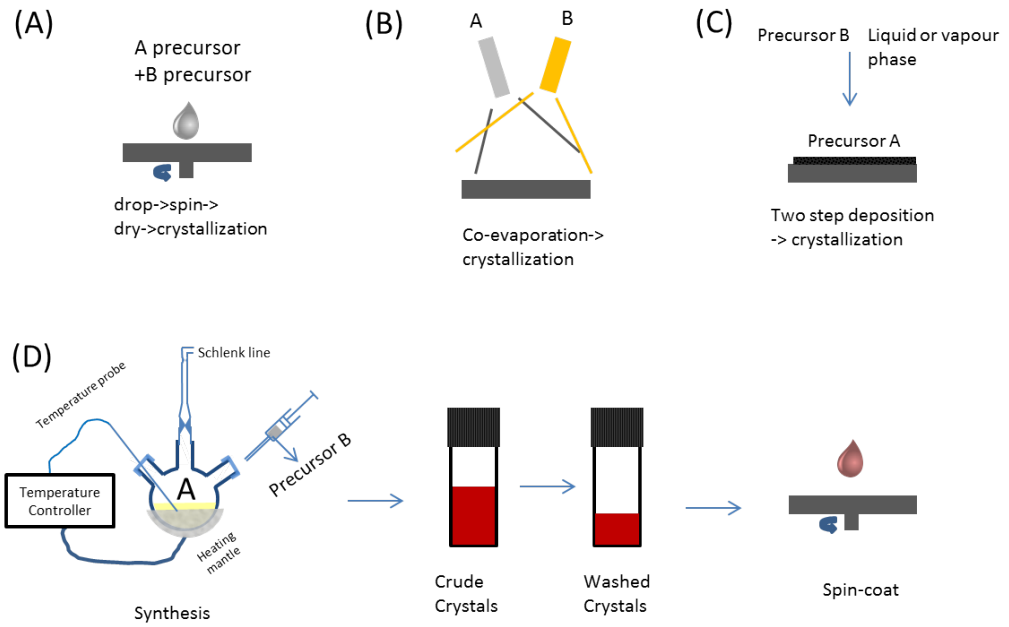

Figure 2.14 Different methods to prepare halide perovskite film: (A) spin-coating (B) co-evaporation (C) two-step deposition (D) colloidal nanocrystal synthesis.

2.5 Conclusion

Essential backgrounds on operations of solar cell and LEDs as well as the role of nanostructures and materials have been introduced. In this thesis we target a few needs as follows and then will address them:

Photovoltaics:

Many excitonic materials have exciton diffusion lengths that do not match the optical absorption length. In order to construct ordered heterojunctions to tackle this, there is a need to extend existing techniques to wider classes of materials. In chapter 4 we will show fabrication of nanostructured solar cell with a high-performance polymer and a singlet fission material.

Light-emitting diodes:

Perovskites offer the advantages of solution-processability, colour-tunability, wide material choices and high PLQE.

However, due to the difficulty to construct a fully-covered perovskite film, to improve the PLQE of film, and to optimize use of perovskite nanocrystals, construction of efficient LED device is challenging. From chapter 5 to chapter 7, we will state problems in detail and present our solutions.

References

1. Nakamura, S., Mukai, T., and Senoh, M., *Candela-class high-brightness InGaN/AlGaN double-heterostructure blue-light-emitting diodes.* Applied Physics Letters, **64**, 1687-1689(1994).
2. Nakamura, S. and Krames, M.R., *History of gallium–nitride-based light-emitting diodes for illumination.* Proceedings of the IEEE, **101**, 2211-2220(2013).
3. Halls, J., Walsh, C., Greenham, N., Marseglia, E., Friend, R., Moratti, S., and Holmes, A., *Efficient photodiodes from interpenetrating polymer networks.* 1995).
4. Yu, G., Gao, J., Hummelen, J.C., Wudl, F., and Heeger, A.J., *Polymer photovoltaic cells: enhanced efficiencies via a network of internal donor-acceptor heterojunctions.* Science, **270**, 1789-1790(1995).
5. Park, S.H., Roy, A., Beaupre, S., Cho, S., Coates, N., Moon, J.S., Moses, D., Leclerc, M., Lee, K., and Heeger, A.J., *Bulk heterojunction solar cells with internal quantum efficiency approaching 100&percnt.* Nature photonics, **3**, 297-302(2009).
6. Pope, M. and Swenberg, C.E., *Electronic processes in organic crystals and polymers*: Oxford University Press (1999)
7. Barford, W., *Electronic and optical properties of conjugated polymers*: Oxford University Press(2005)
8. Leutwyler, W.K., Bürgi, S.L., and Burgl, H., *Semiconductor clusters, nanocrystals, and quantum dots.* Science, **271**, 933-937(1996).
9. Coropceanu, V., Cornil, J., da Silva Filho, D.A., Olivier, Y., Silbey, R., and Brédas, J.-L., *Charge transport in organic semiconductors.* Chemical reviews, **107**, 926-952(2007).
10. Bruice, P.Y. and Education, P., *Essential organic chemistry*: Pearson Education(2006)
11. Petrucci, R.H., Harwood, W.S., Herring, G.F., and Madura, J.D., *General chemistry: principles and modern applications*: Pearson Education International(2007)
12. Menke, S.M. and Holmes, R.J., *Exciton diffusion in organic photovoltaic cells.* Energy & Environmental Science, **7**, 499-512(2014).

13. Kim, J.-S., Lu, L., Sreearunothai, P., Seeley, A., Yim, K.-H., Petrozza, A., Murphy, C.E., Beljonne, D., Cornil, J., and Friend, R.H., *Optoelectronic and Charge Transport Properties at Organic− Organic Semiconductor Interfaces: Comparison between Polyfluorene-Based Polymer Blend and Copolymer.* Journal of the American Chemical Society, **130**, 13120-13131(2008).
14. Marcus, R., *Nonadiabatic processes involving quantum-like and classical-like coordinates with applications to nonadiabatic electron transfers.* The Journal of chemical physics, **81**, 4494-4500(1984).
15. Fishchuk, I., Kadashchuk, A., Bässler, H., and Abkowitz, M., *Low-field charge-carrier hopping transport in energetically and positionally disordered organic materials.* Physical Review B, **70**, 245212(2004).
16. Turro, N.J., *Modern molecular photochemistry*: University science books(1991)
17. Köhler, A. and Bässler, H., *Triplet states in organic semiconductors.* Materials Science and Engineering: R: Reports, **66**, 71-109(2009).
18. Smith, M.B. and Michl, J., *Singlet fission.* Chemical reviews, **110**, 6891-6936(2010).
19. Wilson, M.W., Rao, A., Clark, J., Kumar, R.S.S., Brida, D., Cerullo, G., and Friend, R.H., *Ultrafast dynamics of exciton fission in polycrystalline pentacene.* Journal of the American Chemical Society, **133**, 11830-11833(2011).
20. Rao, A., Wilson, M.W., Hodgkiss, J.M., Albert-Seifried, S., Bassler, H., and Friend, R.H., *Exciton fission and charge generation via triplet excitons in pentacene/C60 bilayers.* Journal of the American Chemical Society, **132**, 12698-12703(2010).
21. Ramanan, C., Smeigh, A.L., Anthony, J.E., Marks, T.J., and Wasielewski, M.R., *Competition between singlet fission and charge separation in solution-processed blend films of 6, 13-bis (triisopropylsilylethynyl) pentacene with sterically-encumbered perylene-3, 4: 9, 10-bis (dicarboximide) s.* Journal of the American Chemical Society, **134**, 386-397(2011).
22. Yu, G., Gao, J., Hummelen, J.C., Wudl, F., and Heeger, A.J., *Polymer photovoltiac cells: Enhanced efficiencies via a network of internal donor-acceptor heterojunctions.* Science, **270**, 1789(1995).

23. Günes, S. and Sariciftci, N.S., *Hybrid solar cells.* Inorganica Chimica Acta, **361**, 581-588(2008).
24. McNeill, C.R., *Morphology of all-polymer solar cells.* Energy & Environmental Science, **5**, 5653-5667(2012).
25. Watkins, P.K., Walker, A.B., and Verschoor, G.L., *Dynamical Monte Carlo modelling of organic solar cells: The dependence of internal quantum efficiency on morphology.* Nano letters, **5**, 1814-1818(2005).
26. Yang, Y., Mielczarek, K., Aryal, M., Zakhidov, A., and Hu, W., *Nanoimprinted polymer solar cell.* ACS nano, **6**, 2877-2892(2012).
27. Lee, J., Jadhav, P., Reusswig, P.D., Yost, S.R., Thompson, N.J., Congreve, D.N., Hontz, E., Van Voorhis, T., and Baldo, M.A., *Singlet exciton fission photovoltaics.* Accounts of chemical research, **46**, 1300-1311(2013).
28. Jadhav, P.J., Mohanty, A., Sussman, J., Lee, J., and Baldo, M.A., *Singlet exciton fission in nanostructured organic solar cells.* Nano letters, **11**, 1495-1498(2011).
29. Ehrler, B., Walker, B.J., Böhm, M.L., Wilson, M.W., Vaynzof, Y., Friend, R.H., and Greenham, N.C., *In situ measurement of exciton energy in hybrid singlet-fission solar cells.* Nature communications, **3**, 1019(2012).
30. Tabachnyk, M., Ehrler, B., Bayliss, S., Friend, R.H., and Greenham, N.C., *Triplet diffusion in singlet exciton fission sensitized pentacene solar cells.* Applied Physics Letters, **103**, 153302(2013).
31. Congreve, D.N., Lee, J., Thompson, N.J., Hontz, E., Yost, S.R., Reusswig, P.D., Bahlke, M.E., Reineke, S., Van Voorhis, T., and Baldo, M.A., *External quantum efficiency above 100% in a singlet-exciton-fission–based organic photovoltaic cell.* Science, **340**, 334-337(2013).
32. Chou, S.Y., Krauss, P.R., and Renstrom, P.J., *Nanoimprint lithography.* Journal of Vacuum Science & Technology B, **14**, 4129-4133(1996).
33. Friend, R., Gymer, R., Holmes, A., Burroughes, J., Marks, R., Taliani, C., Bradley, D., Dos Santos, D., Bredas, J., and Lögdlund, M., *Electroluminescence in conjugated polymers.* Nature, **397**, 121-128(1999).
34. Burroughes, J., Bradley, D., Brown, A., Marks, R., Mackay, K., Friend, R., Burns, P., and Holmes, A., *Light-emitting diodes based on conjugated polymers.* nature, **347**, 539-541(1990).

35. Reineke, S., Lindner, F., Schwartz, G., Seidler, N., Walzer, K., Lüssem, B., and Leo, K., *White organic light-emitting diodes with fluorescent tube efficiency*. Nature, **459**, 234-238(2009).
36. Colvin, V., Schlamp, M., and Alivisatos, A., *Light-emitting diodes made from cadmium selenide nanocrystals and a semiconducting polymer*. Nature, **370**, 354-357(1994).
37. Era, M., Morimoto, S., Tsutsui, T., and Saito, S., *Organic-inorganic heterostructure electroluminescent device using a layered perovskite semiconductor* $(C_6H_5C_2H_4NH_3)_2PbI_4$. Applied Physics Letters, **65**, 676-678(1994).
38. Tan, Z.-K., Moghaddam, R.S., Lai, M.L., Docampo, P., Higler, R., Deschler, F., Price, M., Sadhanala, A., Pazos, L.M., Credgington, D., Hanusch, F., Bein, T., Snaith, H.J., and Friend, R.H., *Bright light-emitting diodes based on organometal halide perovskite.* Nature nanotechnology, 2014).
39. Kelly, G., *Understand color science to maximize success with LEDs–Part 4.* LED Magazine February, 2013).
40. Schubert, E.F., Gessmann, T., and Kim, J.K., *Light emitting diodes*: Wiley Online Library(2005)
41. Chaves, J., *Introduction to nonimaging optics*: CRC Press(2015)
42. Kobayashi, K.-I., Kimura, T., Sawada, H., Terakura, K., and Tokura, Y., *Room-temperature magnetoresistance in an oxide material with an ordered double-perovskite structure.* Nature, **395**, 677-680(1998).
43. Bednorz, J.G. and Müller, K.A., *Possible highT c superconductivity in the Ba− La− Cu− O system.* Zeitschrift für Physik B Condensed Matter, **64**, 189-193(1986).
44. Maeno, Y., Hashimoto, H., Yoshida, K., Nishizaki, S., Fujita, T., Bednorz, J., and Lichtenberg, F., *Superconductivity in a layered perovskite without copper.* Nature, **372**, 532-534(1994).
45. Saito, Y., Takao, H., Tani, T., Nonoyama, T., Takatori, K., Homma, T., Nagaya, T., and Nakamura, M., *Lead-free piezoceramics.* Nature, **432**, 84-87(2004).

46. Moritomo, Y., Asamitsu, A., Kuwahara, H., and Tokura, Y., *Giant magnetoresistance of manganese oxides with a layered perovskite structure.* Nature, **380**, 141-144(1996).

47. Cohen, R.E., *Origin of ferroelectricity in perovskite oxides.* Nature, **358**, 136-138(1992).

48. Inaguma, Y., Liquan, C., Itoh, M., Nakamura, T., Uchida, T., Ikuta, H., and Wakihara, M., *High ionic conductivity in lithium lanthanum titanate.* Solid state communications, **86**, 689-693(1993).

49. Mitzi, D.B., *Synthesis, structure, and properties of organic-inorganic perovskites and related materials.* Progress in Inorganic Chemistry, Volume 48, 1-121(2007).

50. Kojima, A., Teshima, K., Shirai, Y., and Miyasaka, T., *Organometal halide perovskites as visible-light sensitizers for photovoltaic cells.* Journal of the American Chemical Society, **131**, 6050-6051(2009).

51. Lee, M.M., Teuscher, J., Miyasaka, T., Murakami, T.N., and Snaith, H.J., *Efficient hybrid solar cells based on meso-superstructured organometal halide perovskites.* Science, **338**, 643-647(2012).

52. Green, M.A., Ho-Baillie, A., and Snaith, H.J., *The emergence of perovskite solar cells.* Nature Photonics, **8**, 506-514(2014).

53. Jeon, N.J., Noh, J.H., Yang, W.S., Kim, Y.C., Ryu, S., Seo, J., and Seok, S.I., *Compositional engineering of perovskite materials for high-performance solar cells.* Nature, **517**, 476-480(2015).

54. Protesescu, L., Yakunin, S., Bodnarchuk, M.I., Krieg, F., Caputo, R., Hendon, C.H., Yang, R.X., Walsh, A., and Kovalenko, M.V., *Nanocrystals of Cesium Lead Halide Perovskites ($CsPbX_3$, X= Cl, Br, and I): Novel Optoelectronic Materials Showing Bright Emission with Wide Color Gamut.* Nano letters, 2015).

55. Niu, G., Guo, X., and Wang, L., *Review of recent progress in chemical stability of perovskite solar cells.* Journal of Materials Chemistry A, **3**, 8970-8980(2015).

56. Leijtens, T., Eperon, G.E., Noel, N.K., Habisreutinger, S.N., Petrozza, A., and Snaith, H.J., *Stability of Metal Halide Perovskite Solar Cells.* Advanced Energy Materials, 5, 1500963 (2015).

57. Rong, Y., Liu, L., Mei, A., Li, X., and Han, H., *Beyond Efficiency: the Challenge of Stability in Mesoscopic Perovskite Solar Cells.* Advanced Energy Materials, 5, 1506066(2015).

58. Liu, M., Johnston, M.B., and Snaith, H.J., *Efficient planar heterojunction perovskite solar cells by vapour deposition.* Nature, **501**, 395-398(2013).

59. Green, M.A., Emery, K., Hishikawa, Y., Warta, W., and Dunlop, E.D., *Solar cell efficiency tables (Version 45).* Progress in photovoltaics: research and applications, **23**, 1-9(2015).

60. Deschler, F., Price, M., Pathak, S., Klintberg, L.E., Jarausch, D.-D., Higler, R., Hüttner, S., Leijtens, T., Stranks, S.D., and Snaith, H.J., *High photoluminescence efficiency and optically pumped lasing in solution-processed mixed halide perovskite semiconductors.* The Journal of Physical Chemistry Letters, **5**, 1421-1426(2014).

61. Xing, G., Mathews, N., Lim, S.S., Yantara, N., Liu, X., Sabba, D., Grätzel, M., Mhaisalkar, S., and Sum, T.C., *Low-temperature solution-processed wavelength-tunable perovskites for lasing.* Nat Mater, **13**, 476-480(2014).

62. Miyata, A., Mitioglu, A., Plochocka, P., Portugall, O., Wang, J.T.-W., Stranks, S.D., Snaith, H.J., and Nicholas, R.J., *Direct Measurement of the Exciton Binding Energy and Effective Masses for Charge carriers in an Organic-Inorganic Tri-halide Perovskite.* Nature Physics, 11, 582-587(2015)

63. Xing, G., Mathews, N., Sun, S., Lim, S.S., Lam, Y.M., Grätzel, M., Mhaisalkar, S., and Sum, T.C., *Long-range balanced electron-and hole-transport lengths in organic-inorganic CH3NH3PbI3.* Science, **342**, 344-347(2013).

64. Stranks, S.D., Eperon, G.E., Grancini, G., Menelaou, C., Alcocer, M.J., Leijtens, T., Herz, L.M., Petrozza, A., and Snaith, H.J., *Electron-hole diffusion lengths exceeding 1 micrometer in an organometal trihalide perovskite absorber.* Science, **342**, 341-344(2013).

65. Brandt, R.E., Stevanović, V., Ginley, D.S., and Buonassisi, T., *Identifying defect-tolerant semiconductors with high minority-carrier lifetimes: beyond hybrid lead halide perovskites.* MRS Communications, 1-11(2015).

66. Ryu, S., Noh, J.H., Jeon, N.J., Kim, Y.C., Yang, W.S., Seo, J., and Seok, S.I., *Voltage output of efficient perovskite solar cells with high open-circuit voltage and fill factor.* Energy Environ. Sci., **7**, 2614-2618(2014).

67. Maculan, G., Sheikh, A.D., Abdelhady, A.L., Saidaminov, M.I., Haque, M.A., Murali, B., Alarousu, E., Mohammed, O.F., Wu, T., and Bakr, O.M., *CH3NH3PbCl3 Single Crystals: Inverse Temperature Crystallization and Visible-Blind UV-Photodetector.* The Journal of Physical Chemistry Letters, **6**, 3781-3786(2015).

68. Hoke, E.T., Slotcavage, D.J., Dohner, E.R., Bowring, A.R., Karunadasa, H.I., and McGehee, M.D., *Reversible photo-induced trap formation in mixed-halide hybrid perovskites for photovoltaics.* Chemical Science, **6**, 613-617(2015).

69. Comin, R., Walters, G., Thibau, E.S., Voznyy, O., Lu, Z.-H., and Sargent, E.H., *Structural, optical, and electronic studies of wide-bandgap lead halide perovskites.* Journal of Materials Chemistry C, **3**, 8839-8843(2015).

70. Azpiroz, J.M., Mosconi, E., Bisquert, J., and De Angelis, F., *Defects Migration in Methylammonium Lead Iodide and their Role in Perovskite Solar Cells Operation.* Energy & Environmental Science, 8, 2118-2127(2015).

71. Eames, C., Frost, J.M., Barnes, P.R., O'regan, B.C., Walsh, A., and Islam, M.S., *Ionic transport in hybrid lead iodide perovskite solar cells.* Nature communications, **6**, 2015).

72. Leijtens, T., Stranks, S.D., Eperon, G.E., Lindblad, R., Johansson, E.M., McPherson, I.J., Rensmo, H., Ball, J.M., Lee, M.M., and Snaith, H.J., *Electronic properties of meso-superstructured and planar organometal halide perovskite films: charge trapping, photodoping, and carrier mobility.* ACS nano, **8**, 7147-7155(2014).

73. Yin, W.-J., Shi, T., and Yan, Y., *Unusual defect physics in CH3NH3PbI3 perovskite solar cell absorber.* Applied Physics Letters, **104**, 063903(2014).

74. Kim, J., Lee, S.-H., Lee, J.H., and Hong, K.-H., *The role of intrinsic defects in methylammonium lead iodide perovskite.* The Journal of Physical Chemistry Letters, **5**, 1312-1317(2014).

75. Chen, Q., Zhou, H., Song, T.-B., Luo, S., Hong, Z., Duan, H.-S., Dou, L., Liu, Y., and Yang, Y., *Controllable self-induced passivation of hybrid lead iodide*

perovskites toward high performance solar cells. Nano Letters, **14**, 4158-4163(2014).

76. Yang, T.Y., Gregori, G., Pellet, N., Grätzel, M., and Maier, J., *The Significance of Ion Conduction in a Hybrid Organic–Inorganic Lead-Iodide-Based Perovskite Photosensitizer.* Angewandte Chemie, 127, 8016-8021(2015).
77. Juarez-Perez, E.J., Sanchez, R.S., Badia, L., Garcia-Belmonte, G., Kang, Y.S., Mora-Sero, I., and Bisquert, J., *Photoinduced giant dielectric constant in lead halide perovskite solar cells.* The Journal of Physical Chemistry Letters, **5**, 2390-2394(2014).
78. Xiao, Z., Yuan, Y., Shao, Y., Wang, Q., Dong, Q., Bi, C., Sharma, P., Gruverman, A., and Huang, J., *Giant switchable photovoltaic effect in organometal trihalide perovskite devices.* Nature materials, **14**, 193-198(2015).
79. Snaith, H.J., Abate, A., Ball, J.M., Eperon, G.E., Leijtens, T., Noel, N.K., Stranks, S.D., Wang, J.T.-W., Wojciechowski, K., and Zhang, W., *Anomalous hysteresis in perovskite solar cells.* The Journal of Physical Chemistry Letters, **5**, 1511-1515(2014).
80. Pizani, P., Leite, E., Pontes, F., Paris, E., Rangel, J., Lee, E., Longo, E., Delega, P., and Varela, J.A., *Photoluminescence of disordered ABO_3 perovskites.* Applied Physics Letters, 824-826(2000).
81. Yamamoto, H., Okamoto, S., and Kobayashi, H., *Luminescence of rare-earth ions in perovskite-type oxides: from basic research to applications.* Journal of luminescence, **100**, 325-332(2002).
82. Stoumpos, C.C., Malliakas, C.D., and Kanatzidis, M.G., *Semiconducting tin and lead iodide perovskites with organic cations: phase transitions, high mobilities, and near-infrared photoluminescent properties.* Inorganic chemistry, **52**, 9019-9038(2013).
83. Tanaka, K., Takahashi, T., Ban, T., Kondo, T., Uchida, K., and Miura, N., *Comparative study on the excitons in lead-halide-based perovskite-type crystals $CH_3NH_3PbBr_3$ $CH_3NH_3PbI_3$.* Solid state communications, **127**, 619-623(2003).
84. Zheng, K., Zhu, Q., Abdellah, M., Messing, M.E., Zhang, W., Generalov, A., Niu, Y., Ribaud, L., Canton, S.E., and Pullerits, T., *Exciton Binding Energy*

and the Nature of Emissive States in Organometal Halide Perovskites. The journal of physical chemistry letters, **6**, 2969-2975(2015).

85. Yang, Y., Zheng, Y., Cao, W., Titov, A., Hyvonen, J., Manders, J.R., Xue, J., Holloway, P.H., and Qian, L., *High-efficiency light-emitting devices based on quantum dots with tailored nanostructures.* Nature Photonics, **9**, 259-266(2015).
86. Stranks, S.D., Burlakov, V.M., Leijtens, T., Ball, J.M., Goriely, A., and Snaith, H.J., *Recombination kinetics in organic-inorganic perovskites: Excitons, free charge, and subgap states.* Physical Review Applied, **2**, 034007(2014).
87. Noel, N.K., Abate, A., Stranks, S.D., Parrott, E.S., Burlakov, V.M., Goriely, A., and Snaith, H.J., *Enhanced photoluminescence and solar cell performance via Lewis base passivation of organic–inorganic lead halide perovskites.* ACS nano, **8**, 9815-9821(2014).
88. Shao, Y., Xiao, Z., Bi, C., Yuan, Y., and Huang, J., *Origin and elimination of photocurrent hysteresis by fullerene passivation in $CH_3NH_3PbI_3$ planar heterojunction solar cells.* Nature communications, **5**, 5784(2014).
89. Kojima, A., Ikegami, M., Teshima, K., and Miyasaka, T., *Highly luminescent lead bromide perovskite nanoparticles synthesized with porous alumina media.* Chemistry Letters, **41**, 397-399(2012).
90. D'Innocenzo, V., Srimath Kandada, A.R., De Bastiani, M., Gandini, M., and Petrozza, A., *Tuning the light emission properties by band gap engineering in hybrid lead halide perovskite.* Journal of the American Chemical Society, **136**, 17730-17733(2014).
91. Dou, L., Wong, A.B., Yu, Y., Lai, M., Kornienko, N., Eaton, S.W., Fu, A., Bischak, C.G., Ma, J., and Ding, T., *Atomically thin two-dimensional organic-inorganic hybrid perovskites.* Science, **349**, 1518-1521(2015).
92. Zhang, D., Eaton, S.W., Yu, Y., Dou, L., and Yang, P., *Solution-Phase Synthesis of Cesium Lead Halide Perovskite Nanowires.* Journal of the American Chemical Society, **137**, 9230-9233(2015).
93. Sichert, J.A., Tong, Y., Mutz, N., Vollmer, M., Fischer, S., Milowska, K.Z., García Cortadella, R., Nickel, B., Cardenas-Daw, C., and Stolarczyk, J.K., *Quantum Size Effect in Organometal Halide Perovskite Nanoplatelets.* Nano letters, **15**, 6521-6527(2015).

94. Dong, Q., Fang, Y., Shao, Y., Mulligan, P., Qiu, J., Cao, L., and Huang, J., *Electron-hole diffusion lengths> 175 μm in solution-grown $CH_3NH_3PbI_3$ single crystals.* Science, **347**, 967-970(2015).

95. Nie, W., Tsai, H., Asadpour, R., Blancon, J.-C., Neukirch, A.J., Gupta, G., Crochet, J.J., Chhowalla, M., Tretiak, S., and Alam, M.A., *High-efficiency solution-processed perovskite solar cells with millimeter-scale grains.* Science, **347**, 522-525(2015).

96. Shi, D., Adinolfi, V., Comin, R., Yuan, M., Alarousu, E., Buin, A., Chen, Y., Hoogland, S., Rothenberger, A., and Katsiev, K., *Low trap-state density and long carrier diffusion in organolead trihalide perovskite single crystals.* Science, **347**, 519-522(2015).

97. Schwartz, R.W., *Chemical solution deposition of perovskite thin films.* Chemistry of Materials, **9**, 2325-2340(1997).

98. Jeon, N.J., Noh, J.H., Kim, Y.C., Yang, W.S., Ryu, S., and Seok, S.I., *Solvent engineering for high-performance inorganic–organic hybrid perovskite solar cells.* Nature materials, 2014).

99. Heo, J.H., Song, D.H., and Im, S.H., *Planar $CH_3NH_3PbBr_3$ Hybrid Solar Cells with 10.4% Power Conversion Efficiency, Fabricated by Controlled Crystallization in the Spin-Coating Process.* Advanced Materials, **26**, 8179-8183(2014).

100. Chen, Q., Zhou, H., Hong, Z., Luo, S., Duan, H.-S., Wang, H.-H., Liu, Y., Li, G., and Yang, Y., *Planar heterojunction perovskite solar cells via vapor-assisted solution process.* Journal of the American Chemical Society, **136**, 622-625(2013).

101. Schmidt, L.C., Pertegás, A., González-Carrero, S., Malinkiewicz, O., Agouram, S., Mínguez Espallargas, G., Bolink, H.J., Galian, R.E., and Pérez-Prieto, J., *Nontemplate synthesis of $CH_3NH_3PbBr_3$ perovskite nanoparticles.* Journal of the American Chemical Society, **136**, 850-853(2014).

102. Zhang, F., Zhong, H., Chen, C., Wu, X.-g., Hu, X., Huang, H., Han, J., Zou, B., and Dong, Y., *Brightly Luminescent and Color-Tunable Colloidal $CH_3NH_3PbX_3$ (X= Br, I, Cl) Quantum Dots: Potential Alternatives for Display Technology.* ACS nano, **9**, 4533-4542(2015).

Chapter 3

Experimental Methods

In this chapter we explain the common experiments used throughout this thesis. Specialized methods, such as nanostructure fabrication methods, crosslinking treatment, will be found in the main chapters.

3.1 Device Construction

Our solar cells and light-emitting diodes are constructed in similar processes.

The components of our devices are shown in Figure 3.1(A). Glass substrates coated with ~150 nm thick ITO stripes are sonicated in acetone and then isopropanol for 5 minutes each. The substrates were then cleaned in an oxygen-plasma cleaner for 10 minutes at a power of 250 W. Then the bottom layer, the active layer and the top layer were deposited sequentially, usually by spin-coating, and followed by annealing according to need. The metallic electrode was thermally evaporated at a vacuum better than 5×10^{-6} mbar through a metal mask. To make good electrical contacts to the device, a process called 'legging' was carried out by attaching metallic frames to the top and bottom electrodes separately. At the end, the devices were either tested without encapsulation but in an enclosed box (for chapter 4), or tested in air right after out of an enclosed nitrogen vial (for chapter 5), or tested after encapsulated with a UV epoxy and a glass slide (for chapter 7). Figure 3.1 (B) shows a complete device. Solar cells are tested with the light incident through the ITO/glass side; LEDs are tested with the light coming out from the ITO/glass side. The overlap area of the ITO and the top metallic electrode is 4.5 mm^2, as shown in figure 3.1 (C), and defines the device active area.

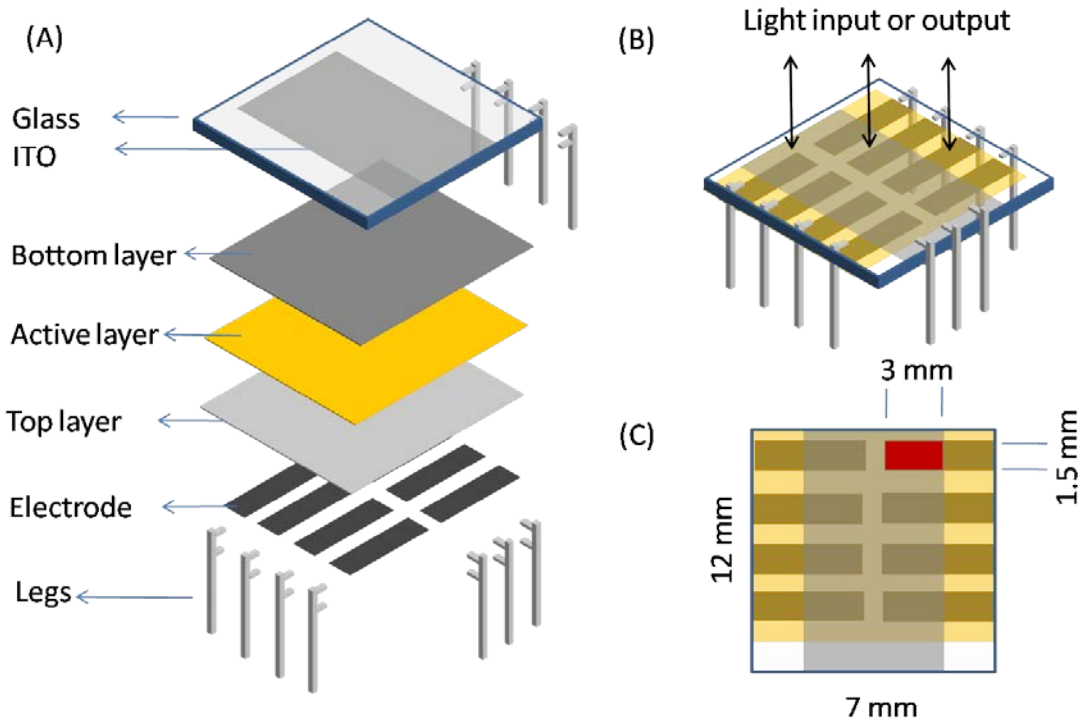

Figure 3.1 (A) Components of our devices. (B) A complete device. (C) Dimensions of a complete device (the red area indicates the active area).

3.2 Device Characterization

3.2.1 Characterization of Solar Cells

Figure 3.2(A) is an drawing of the setup to measure external quantum efficiency (EQE). The light source is a 250 W tungsten filament lamp, and provides a broadband emission. A Oriel Cornerstone 260 monochromator is used to select narrow-band light with a resolution of 5 nm. Half of the narrow-band light is separated by a beam splitter, and goes to a reference silicon photodiode; and the rest of the light goes straight to the test position.

First a calibrated silicon diode with a known photocurrent responsivity (in A/W) was put in the test position. The output current of the calibrated silicon diode is monitored by a Keithley 2635 SourceMeter. At the same time, the electrical current generated from the reference photodiode is monitored by an thorlabs photodiode amplifier and a Keithley 2000 multimeter. In this way, a calibration step is carried out

to calibrate the illumination power in the test position against the output of the reference diode over the entire wavelength range.

The cell to test is connected in the test position and monitored by a Keithley 2635 SourceMeter. EQE spectrum is measure by scaning the monochromator across the wavelength range of interest, while the power of incoming light is monitored by the reference cell and the photocurrent from the cell is monitored by Keithley 2635 SourceMeter.

This method offers better accuracy against the fluctuations of the light source power during measurement.

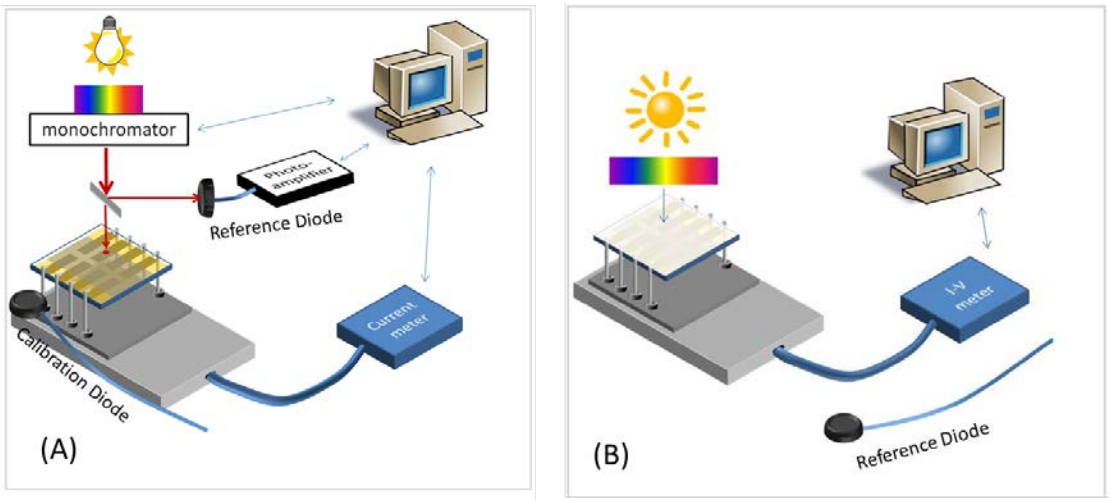

Figure 3.2 Illustration of the setup to measure the EQE (A), PCE (B) of a solar cell.

As Figure 3.2(B) shows, an air mass 1.5G solar simulator (ABET technologies Sun 2000 Solar Simulator) is equipped with a 1500 W xenon arc lamp and a filter. The power of the lamp is set using a standard silicon diode, corrected by a mismatch factor (calculated from the EQE spectrum of the cell) to compensate the spectra difference of solar light and our simulated light. Light-IV and dark-IV curves were measured using a Keithley 2635 source meter controlled by a Lab-view program.

3.2.2 Characterization of Light-Emitting Diodes

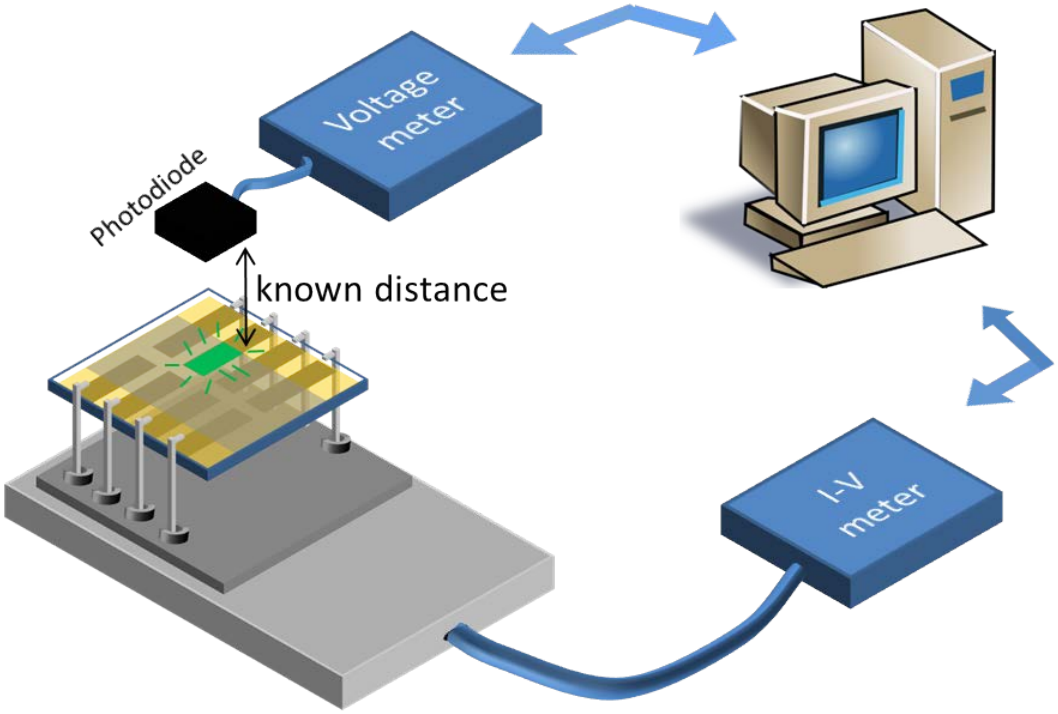

Figure 3.3 Illustrations on the setup to measure the LED performance

Figure 3.3 illustrates how we determine external quantum efficiency and luminance of a LED. The photo-detector was fixed at a known distance above the emitting pixel to measure the emission intensities. The LED is powered by a Keithley meter, while the I-V current is scanned across the range of interest. The EL spectrum is measured by a Labsphere Spectrometer.

The quantity of photons received by the photo-diode can be calculated by the EL spectrum and the photo-diode response. Assuming the emission profile of the LED is Lambertian emission profile and the solid angle occupied by the diode is approximated by A/d^2 (Under the assumption that $d^2>>A$, where A is the photo-detection diode area, d is the photodiode-LED distance), the quantity of photons emitted by the LED can be calculated in the entire π solid angle. The total photons emitted per second can be then divided by the electrons passing the external circuit per second to obtain the EQE value. The luminance can be calculated by the standard luminous function, the EL spectrum and the entire number of photons emitted from the LED.

3.3 Spectroscopic Characterization

3.3.1 Photoluminescence quantum efficiency (PLQE)

Photoluminescence quantum efficiency refers to the ratio of photons that are emitted by a photo-excited material, to the number of photons absorbed in the excitation process. In order to resolve issues such as scattering and reflection of light in the samples, we carried out our measurement following Reference [1]. In the algorism of Reference [1], 3 sets of PL spectra are collected, as Figure 3.4 shows, an optical fibre were inserted to the top of the integrating sphere to quantify the PL spectrum in the sphere. In the 'blank' configuration (Figure 3.4 (A)), no sample is in the integrating sphere; in the 'sample on' configuration (Figure 3.4 (B)), the sample is held in the path of the laser beam, thus most of the PL signal is from direct laser beam excitation; in the 'sample off' configuration (Figure 3.4 (C)), sample is held in the sphere but off the direct path of laser beam. Thus the PL signal is excited by scattered laser beam

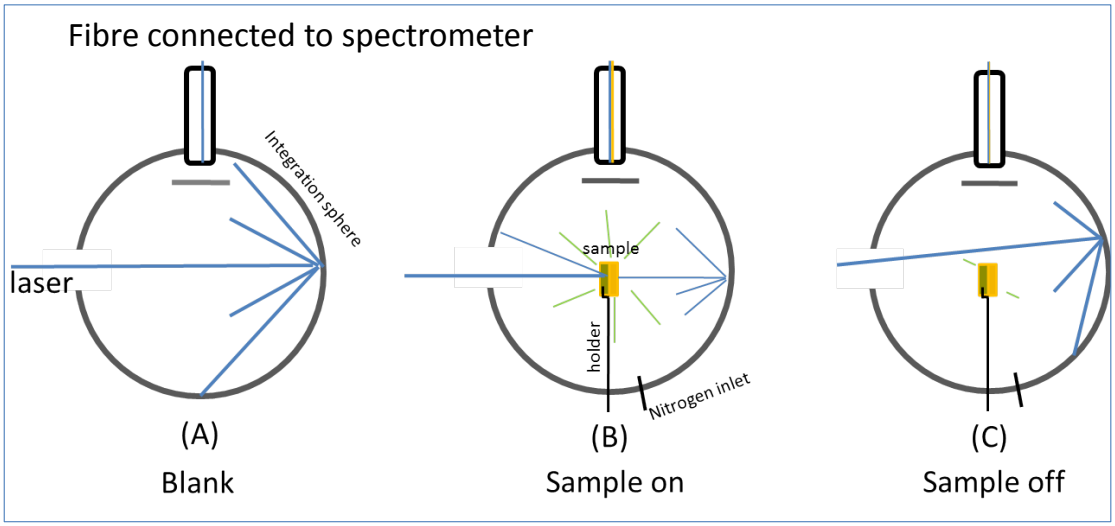

Figure 3.4 Illustration of experimental configurations to measure PLQE of a film: (A) blank, (B) sample on, (C) sample off.

3.3.2 Time-correlated single-photon counting (TCSPC)

TCSPC is a technique to determine the lifetime of the photo-excited state in a material following photo-excitation. The measurement is based on the detection of single photons and their arrival times in respect to a reference signal which is a short-pulse laser.

In our system, a pulsed 10 MHz diode laser (Pico Quant LDH400) emitting at 407 nm with 80 ps FHWM is used as excitation source. The photon emissions were detected by a microchannel-plate photomultiplier (Hamamatsu Photonics) coupled to a monochromator and TCSPC electronics (Lifespec-pc and VTC900 PC card, Edinburgh Instruments).

3.3.3 X-ray Photoelectron Spectroscopy (XPS)

XPS is a surface-sensitive quantative spectroscopic technique that detects the energy dispersion of electrons that escaped from sample surface after the sample is excited by X-ray. The detection depth is usually a few nanometres, determined by the photoelectron escaping depth. The XPS spectrum is a plot of the counts of photoelectrons as a function of binding energy. The characteristic spectral peaks correspond to the electron configuration of the electrons within atoms. The integral number of the electrons in each of the peaks in directly related to the amount of element within the XPS sampling volume. These integral numbers are corrected by a relative sensitivity factor to generate elementary composition values.

We use a commercial XPS setup ‘ESCALAB 250Xi’. The setup was equipped with an XR6 monochromated Al K_α X-ray source ($h\nu$=1486.6 eV). The XPS samples were prepared on silicon substrates by spin-coating from solution. Measurement is done in ultra-high-vacuum (UHV, pressure $<10^{-9}$mbar). In some of the measurement, in-situ argon ion sputtering is used to obtain a depth profile.

3.3.4 Fourier Transform Infrared Spectroscopy (FTIR)

FTIR is a rapid molecular spectroscopic technique and chemical analysis method. We used it to understand qualitatively the chemical reaction caused by

material processing. In the infrared transmission spectrum of a film, the transmission valleys correspond to the vibration frequencies of chemical bonds in the material.

We used a commercial Agilent Technologies Cary 600 Series FTIR Spectrometer. The samples were prepared by spin-coating from solution on to 20 mm diameter 1 mm thick KBr substrates (Sigma Aldrich). The measurement was done within the mid-infrared range (5000 cm^{-1} to 500 cm^{-1}), with 10-100 sampling average. The background is corrected before each measurement.

3.4 Structural Characterization

3.4.1 Scanning electron microscopy (SEM)

SEM is a technique to scan a focused electron beam across the surface of a sample, to acquire information on the sample's surface topography and chemical composition. It analyses the signal backscattered from the sample, thus it is useful for samples with any thickness provided they are sufficiently conductive [2].

In this thesis, a LEO 1550 SEM system was used with an in-lens detector. We analyse the signal from the secondary electrons. This signal is a low energy and surface-sensitive signal, and is influenced by both topographic contrast and atomic number contrast.

The sample is mounted in the SEM chamber and measured in vacuum better than 1×10^{-5} mbar. The incident electron beam is accelerated by a voltage of 10 kV. The best resolution of our image is 1-5 nm.

3.4.2 Transmission electron microscopy (TEM)

TEM images were kindly captured by Florencia Wisnivesky Rocca Rivarola from Electron Microscopy group, Material Science department, Cambridge.

TEM analyses the beam of electrons that transmitted through an ultra-thin sample. High-resolution transmission electron microscopy (HRTEM) is an imaging mode of the TEM that allows for direct imaging of the atomic structure of the sample.

A FEI Tecnai Osiris TEM/STEM 80-200 microscope operating at 200 kV was used. The TEM samples were analysed through high angle annular dark field STEM (HAADF-STEM). [2] The samples are prepared by drop-casting 2-5 mg/ml nano-crystal dispersion in hexane, onto carbon coated thin TEM grids.

3.4.3 Electron energy loss spectroscopy (EELS)

EELS images were kindly captured and analysed by Florencia Wisnivesky Rocca Rivarola and Dr. Francisco de la Peña from Electron Microscopy group, Material Science department, Cambridge.

EELS is a technique to analyse the electron signal that inelastically scattered through inner-shell ionization of targeted materials. Compared to the energy-dispersive x-ray spectroscopy (EDX), EELS works better at relatively low atomic numbers, such as carbon and aluminium.

In this thesis, a FEI Tecnai Osiris TEM/STEM 80-200 microscope operating at 200 kV, and with a Gatan Enfinium ER 977 spectrometer was used. Core-loss spectra were acquired over different regions of the specimen, using a 2 nm pixel size. Dark current and gain variations in the detector were corrected in all spectra. The dwell time was 0.2 s for core-loss spectra and 10 μs for low-loss spectra. Convergence and collection angles were 8.5 mrad and 34 mrad respectively.

Weighted principal component analysis (PCA) and independent component analysis (ICA) were used to obtain the elemental maps [3]. Curve fitting of the ICA results using Hartree-Slater cross sections was carried out to quantify the maps. The open source software package HyperSpy was used to calculate the relative elemental quantuity on the EELS map [4].

3.4.4 Atomic force microscopy (AFM)

AFM is a type of high-resolution scanning probe microscopy (SPM). By monitoring the interaction of a nano-sized tip with the surface of a sample, AFM is able to capture surface height information at a resolution of nanometre.

On the right is the illustration of a typical AFM configuration (from Wikipedia)We use an AFM model of Dimension^{TM} 3100. We acquired our AFM data with tapping mode, at scanning speed of 0.5-1 Hz.

3.4.5 X-ray Diffraction (XRD)

We use a powder diffraction XRD technique in this thesis [5].

XRD is a technique to identify the structure of a crystal, by elastically diffracting X-rays through the crystal lattice and recording the diffraction patterns.

XRD can be useful to estimate size of nanocrystals below 100 nm by analysing the broadening of diffraction peaks following the Scherrer Equation [6]:

$$B(2\theta) = \frac{K\lambda}{Lcos\theta}$$

B is the integral peak width (in radians 2θ), which is the width of a rectangle with the same height and area as the diffraction peak. L is the volume-weighted crystal size, K is the Scherrer constant (assumed here to be 1), λ is the X-ray wavelength. This equation gives best result when B is much bigger than instrumental broadening.

The samples are prepared by spin-coating on glass substrate and characterized under ambient condition. We use a Bruker D8 Advance diffractometer with copper radiation source (~1.541 Å) and a position-sensitive (Lynx Eye) detector.

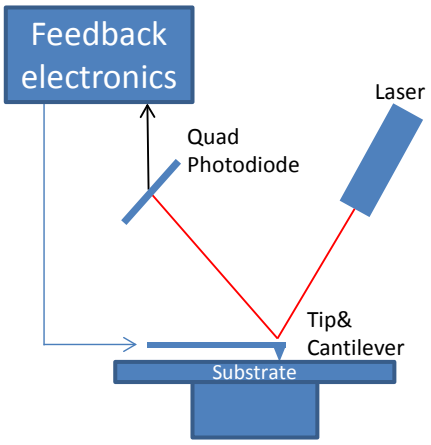

3.5 Material Synthesises

3.5.1 CH_3NH_3Br

Methylammonium bromide (CH_3NH_3Br) was prepared by adding 33 wt% methylamine solution in ethanol (24 mL) and 48 wt% hydrobromic acid in water (8.5 mL) to 100 mL of absolute ethanol. The reaction mixture was stirred at room temperature in a nitrogen atmosphere. The solvent was removed by rotary evaporation until white crystals started to appear. The crystals were collected by Büchner funnel filtration and were dried overnight under vacuum at 80 °C. The perovskite precursor solution was prepared by mixing CH_3NH_3Br and $PbBr_2$ at different molar ratios in anhydrous N, N-dimethylformamide (DMF, from ROMIL).

This material was synthesized by May Ling Lai, and used in Chapter 5 and chapter 6.

3.5.2 $CsPbX_3$ nanocrystals

Perovskite nanocrystals were synthesized using previously reported procedures [7]. Cs_2CO_3 (0.814g, 99.9%) was loaded into 100 mL 3-neck flask along with octadecene (ODE, 30 mL, 90%) and oleic acid (2.5 mL, OA, 90%), and the mixture was dried for 2h at 120 °C under N_2. The solution temperature was then lowered to 100 °C. ODE (75 mL), oleylamine (7.5 mL, OLA, 90%) and dried OA (7.5 mL) and PbX_2 (2.82 mmol) such as PbI_2 (1.26 g, 99.99%), PbBr2 (1.035 g, 99.99%), $PbCl_2$ (0.675g, 99.99%) or their mixtures were loaded into a 250 mL 3-neck flask and dried under vacuum for 2h at 120 °C. After complete solubilisation of the PbX_2 salt, the temperature was raised to 170 °C and the Cs-oleate solution (6.0 mL, 0.125 M in ODE, prepared as described above) was quickly injected. After 10s, the reaction mixture was cooled in an ice-water bath. For $CsPbCl_3$ synthesis, 1 mL of trioctylphosphine (TOP, 97%) was added to solubilize $PbCl_2$. The nanocrystals were precipitated from solution by the addition of equal volume anhydrous butanol (BuOH, 99%) (ODE:BuOH=1:1 by volume). After centrifugation, the supernatant was discarded and the nanocrystals were redispersed in anhydrous hexane (99%) and precipitated again with the addition of BuOH (Hexane:BuOH=1:1 by volume). These were redispersed in hexane. The nanocrystal dispersion was filtered through a 0.2 μm PTFE filter and diluted to 10mg/mL in hexane before use.

This material was synthesized by Nate, Tom, Guangru, and used in Chapter 7.

3.5.3 ZnO nanoparticles

Colloidal ZnO nanocrystals were synthesized by a solution-precipitation process according to previously reported procedures [8]. Typically, zinc acetate dihydrate (329 mg) was dissolved in dimethyl sulphoxide (DMSO) (0.5 M) by stirring at room temperature. A solution of tetramethylammonium hydroxide (TMAH, 453 mg) in ethanol (5 mL) was then added dropwise within 5 min. After 2 h, the product mixture was decanted and washed twice with ethyl acetate and ethanol. Ethanol (6 mL) was added to disperse the precipitate and produce a colloidal ZnO nanocrystal dispersion with a concentration of ~7 mg/ mL. The dispersion was filtered with a 0.45 μm PTFE filter before use.

This material was synthesized by Sai Bai and used in Chapter 7.

References

1. de Mello, J.C., Wittmann, H.F., and Friend, R.H., *An improved experimental determination of external photoluminescence quantum efficiency.* Advanced Materials, **9**, 230-232(1997).
2. Williams, D.B. and Carter, C.B., *Transmission electron microscopy Second Edition, Part 1-Part 4*: Springer(2009)
3. de la Peña, F., Berger, M.H., Hochepied, J.F., Dynys, F., Stephan, O., and Walls, M., *Mapping titanium and tin oxide phases using EELS: An application of independent component analysis.* Ultramicroscopy, **111**, 169-176(2011).
4. Peña, F.d.l., Burdet, P., Ostasevicius, T., Sarahan, M., Nord, M., Fauske, V.T., Taillon, J., Eljarrat, A., Mazzucco, S., Donval, G., Zagonel, L.F., Walls, M., and Iyengar, I., *hyperspy: HyperSpy 0.8.2.* 2015.
5. Klug, H.P. and Alexander, L.E., *X-ray diffraction procedures.* 1954).
6. Langford, J.I. and Wilson, A., *Scherrer after sixty years: a survey and some new results in the determination of crystallite size.* Journal of Applied Crystallography, **11**, 102-113(1978).
7. Protesescu, L., Yakunin, S., Bodnarchuk, M.I., Krieg, F., Caputo, R., Hendon, C.H., Yang, R.X., Walsh, A., and Kovalenko, M.V., *Nanocrystals of Cesium Lead Halide Perovskites ($CsPbX_3$, X= Cl, Br, and I): Novel Optoelectronic Materials Showing Bright Emission with Wide Color Gamut.* Nano letters, 2015).
8. Bai, S., Wu, Z., Wu, X., Jin, Y., Zhao, N., Chen, Z., Mei, Q., Wang, X., Ye, Z., Song, T., Liu, R., Lee, S.-t., and Sun, B., *High-performance planar heterojunction perovskite solar cells: Preserving long charge carrier diffusion lengths and interfacial engineering.* Nano Research, **7**, 1749-1758(2014).

Chapter 4

Solar Cells Fabricated on Nano-structured Substrates

Ideal nanoscale phase separation in the active layer of an exciton-based solar cell should happen both laterally and vertically, on the correct length scale. Lateral phase-separation is to allow most excitons to reach the donor/acceptor interfaces; vertical phase separation is to allow the free electrons and holes generated from exciton separation to be collected. In this chapter, to realise an ordered nano-structure with controlled sizes, we develope nano-fabrication methods that offer better scalability and applicability compared to previous methods. We showcase one prototype solar cell based on a high performance polymer, PBDTTT-CT. Then we realise patterning of singlet fission materials TIPS-pentacene and pentacene, which is important for making singlet fission solar cells. Finally we show a prototype singlet fission solar cell based on a nano-structured ZnO scaffold.

4.1 Overview

In 2005, Watkins et al. [1] suggested that in the PFB/F8BT solar cell system, the optimized polymer domain size in the active layer of a polymer solar cell is ~20 nm. Researchers have fabricated such an ordered structure, by techniques such as nano-imprinting. In 2008, Cheyns et al. [2] fabricated nanoimprinted 50-nm wide trenches in P3HT films, and realised a solar cell with 0.1% power conversion efficiency (PCE) by backfilling an polymer acceptor PTCDI-C_{13}. The first efficient nano-imprinted solar cell was reported by He et al. [3, 4] in 2010. Using templates fabricated through e-beam lithography, EQEs of 1.9% and 3.5% were realized in P3HT/F8TBT and P3HT/PCBM solar cells respectively. In 2011, Dian et al. [5] replaced the e-beam-fabricated template with an anodic aluminium oxide (AAO) template and realised a P3HT/PCBM solar cell with 2.4% EQE.

Despite the relatively high efficiency obtained, the methods above have several drawbacks: The e-beam templating method used by He et al. [3, 4] is expensive, slow and not scalable. Cheyns et al. [2] and Dian et al. [5] thermally imprinted P3HT which can cause thermal degradation; also, thermal imprinting is not adaptable with PEDOT:PSS, TIPS-pentacene and metal oxide.

To tackle these drawbacks, in Section 4.2 we will demonstrate diblock-copolymer lithography as a tool to fabricate templates over large areas, with feature sizes smaller than 50 nm. In Section 4.3 we will show that, using a solvent-vapour-assisted imprinting method, a high-glass-transition-temperature polymer and a water-soluble polymer are successfully imprinted with no need for heating. A method to pattern TiO_2 electrode is also presented. In Section 4.4, an imprinted PBDTTT-CT/$PC_{70}BM$ solar cell is fabricated.

Apart from conjugated polymers, singlet fission materials such as pentacene, TIPS-pentacene are of particular interest. Singlet fission solar cells have the potential to produce double photocurrent in the short-wavelength range compared to traditional cells, and thus are able to reach higher PCE limit [6]. In these materials, a photon is absorbed first to excite a singlet exciton state. The singlet then splits into two triplets. Then the triplet diffuses to donor/acceptor interface, before separating into free carriers. The triplet exciton diffusion length in singlet fission materials is 10-50 nm in polycrystalline materials such as pentacene [7, 8] and up to microns in single crystals such as rubrene [9, 10]. Although these values are larger than singlet diffusion length in conjugated polymers, singlet fission materials mostly are small molecules that suffer from low absorption coefficients, for example in the optimized pentacene solar cell, the 40 nm pentacene film only absorbs 30% of the incident light at the peak of its absorption spectrum [11-13]. So far only one report has realized EQE above 100%, which is in a pentacene/C60 solar cell. Although bulk heterojunction approach have been attempted but the best EQE did not surpass the best planar devices [14].

In Section 4.5 we demonstrate that pentacene and TIPS-pentacene are successfully patterned on sub-50 nm scale. In Section 4.6, we demonstrate a nano-structured TIPS-pentacene cell based on ZnO nanopillars.

4.2 Copolymer lithography

A diblock copolymer consists of two immiscible polymer blocks A and B which are covalently bonded together. Its self-assembling behaviours in films have been well studied [15, 16]. In brief, if the polymer is given sufficient mobility e.g. by thermal annealing, it will self-assemble to minimize the free energy. Depending on the weight ratio of two blocks, a spherical phase, a cylindrical phase, a gyroid phase or a lamellar phase can be formed. Here we use PS-b-PMMA polymers with PMMA volume ratio of about 30%, these copolymers self-assemble into hexagonal arrays of cylinders [17, 18].

The chemical structures of the polymers we used are shown in Figure 4.1 (A) and (B). The fabrication processes of the silicon template are shown in Figure 4.1 (1)-(9). We generated copolymer-lithography patterns on silicon substrates following the method in literature [19]. The silicon substrates were cleaned in piranha solution (98% sulphuric acid/30% hydrogen peroxide=3:1) at 80^{o}C for 1 hr to form a hydroxide-rich surface. 10 mg/ml random-copolymer of hydroxide-terminated PS-r-PMMA dissolved in toluene (purchased from Polymer Source, with chemical structure shown in Figure 4.1 (B), with molecular mass of 13kDa, polystyrene weight ratio of 59% and PDI of 1.3) was spin-coated at 2000 rpm on the silicon substrates, followed by annealing at around 185°C in vacuum for 60 hr to allow the hydroxide-terminated PS-r-PMMA to graft to the natural oxide surface. Un-grafted PS-r-PMMA was washed away by toluene. This step is to tune the interfacial energies of the silicon/PS and silicon/PMMA to be the same thus self-assembled PMMA cylinders are able to stand vertically to the silicon surface [18]. Then a 9 mg/ml diblock-copolymer PS-b-PMMA (purchased from Polymer Source, with chemical structure shown in Figure 4.1 (A), with molar mass of 101 kDa, PMMA weight ratio of 30.7% and PDI of 1.08) was spin-coated at 6000 rpm on top of the PS-r-PMMA-modified silicon substrates, followed by annealing in a glovebox at 185 °C for 1 hr, resulting in 25 nm thick films. The films were UV-developed under a 254 nm UV lamp for 1 hr in a glove box (dose~30J/cm^2). During this UV treatment, bonds between the PS and the PMMA blocks were broken and the PMMA blocks were degraded. The films were brought to air and they are washed with acetic acid to remove the PMMA blocks. A gentle oxygen plasma etching was applied to etch away

residual PS-r-PMMA modification layer. 50 cycles of alumina were deposited uniformly on the whole structure by atomic layer deposition at 100 ^{o}C, to provide a hard dry-etching mask that has good etch ratio against etching of silicon. Ar plasma etching was employed to etch away the alumina on top of the polystyrene matrix. We found that the etching rate in the holes was slower than on the top. Thus after using O_2 plasma to remove the PS matrix, 2-3 nm high alumina dot arrays were left on the surface of the silicon substrate. These alumina dot patterns were then transferred by dry etching with SF_6/O_2 plasma into the silicon substrate. The resultant silicon substrates with pillar structures were modified by vapour-phase treatment with perfluorodecyltrichlorosilane (FDTS) in an evacuated desiccator overnight to improve mold releasing properties.

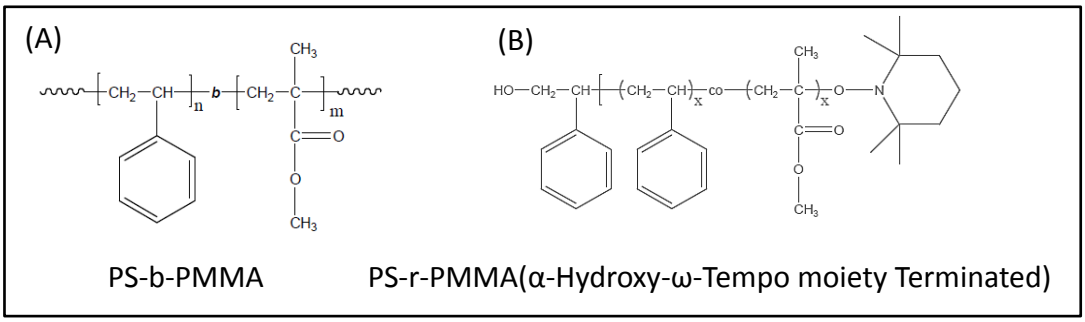

Figure 4.1 (A) Chemical structure of PS-b-PMMA. (B) Chemical structure of PS-r-PMMA.

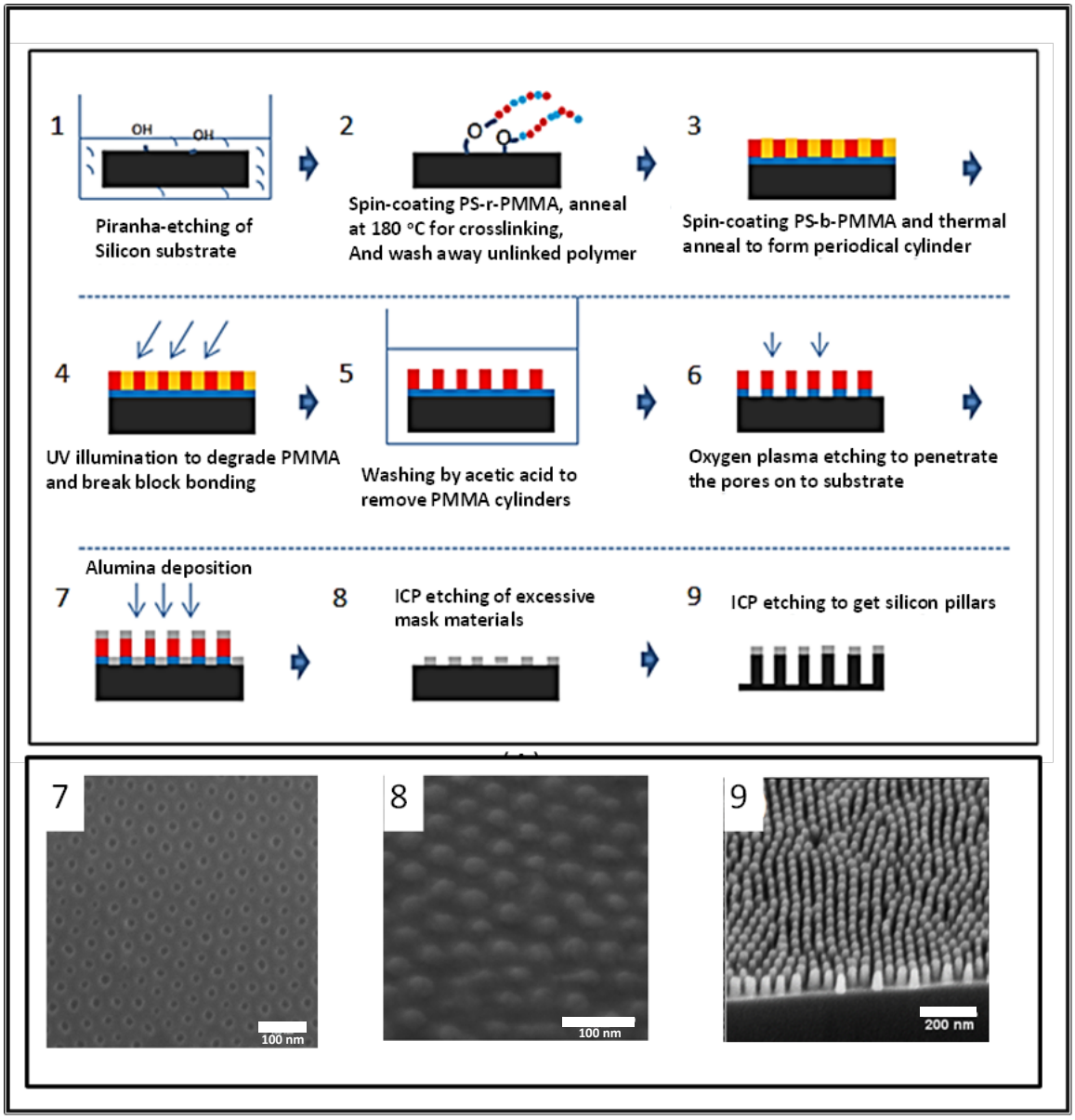

Figure 4.2 (1)-(9) Flow chart showing the processes to fabricate the silicon template from di-block copolymer; top-view SEM images of (7) the polystyrene matrix covered with 50 cycle alumina; (8) alumina dots fabricated from the polystyrene matrix; (9) silicon pillars. Scale bars: 100 nm in (7) and (8), 200nm in (9). Note: all the dry etching recipes can be found in Section 4.6

Figure 4.2 (7) shows the polystyrene matrix fabricated by copolymer lithography. The holes were uniformly distributed, and had a diameter of 25 nm and a period of 50 nm. Figure 4.2 (8) shows the alumina-dot arrays transferred from the polystyrene matrix. Figure 4.2 (9) shows the silicon pillars fabricated from the alumina-dot arrays by dry etching.

4.3 PBDTTT-CT, PEDOT:PSS and TiO_2 nanostructures

Large donor/acceptor interfacial area in a solar cell is important to enable more excitons to reach the interfaces. We show imprinting nanostructure of a donor material–PBDTTT-CT in Section 4.3.1. Large area of electrode is important to improve charge extraction in a solar cell or charge injection in a LED. We show patterning of electrode materials, such as PEDOT:PSS and TiO_2 in Section 4.3.2 and Section 4.3.3, respectively.

4.3.1 PBDTTT-CT nanostructure

PBDTTT-CT is a low-bandgap polymer (1.8 eV), with a chemical structure shown in Figure 4.3. Bulk heterojunction solar cells made of PBDTTT-CT have demonstrated PCE performance as high as ~9% [20]. However, it is difficult to thermally imprint PBDTTT-CT because of its high glass-transition temperature at 400-410 ^{o}C [21].

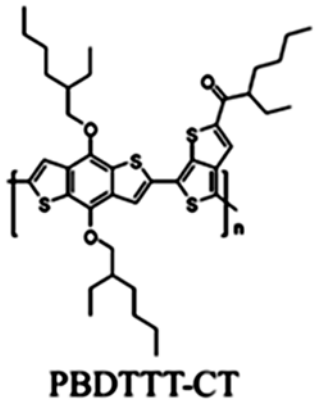

Figure 4.3 Chemical structure of PBDTTT-CT.

We used a solvent-vapour-assisted imprinting method to achieve room-temperature imprinting of PBDTTT-CT, with a setup reported in the literature [22]. Figure 4.4 (A) illustrates our setup: nitrogen (line A) was bubbled through a solvent bottle to form saturated solvent vapour. The vapour going out of the solvent bottle was mixed with another line (line B) of dry nitrogen. Flows of the two lines were controlled by two flow controllers respectively, in order to change saturation ratios in the mixed vapour. The mixed vapour then entered an imprinting chamber

sealed with a metallic lid. An imprinting stamp was installed in the center of the lid. The photo of the setup is shown in Figure 4.4 (B)

Our imprinting pressure controller is shown in Figure 4.4(C). To monitor the imprinting pressure, a load cell is installed to the stamp. A load cell is a transducer that is able to produce an electrical signal proportional to the force being measured. We used an S type load cell–TEDEA MODEL 615. Force is applied to the load cell and the stamp by a mechanical screw and calibrated with a standard weight. Imprinting pressure is calculated from the force applied and the area of the silicon stamp, thus it indicates the pressure on entire area of the silicon stamp. Areas of the silicon templates are 1×1 cm^2. Maximum imprinting pressure is ~150 bar.

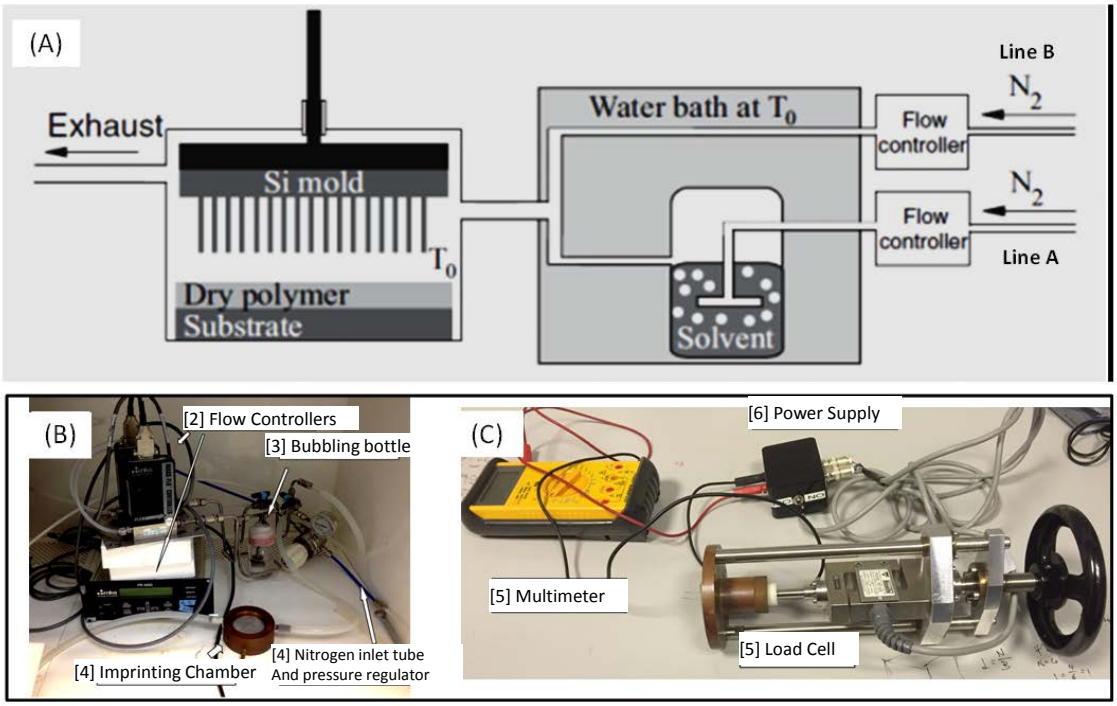

Figure 4.4 (A) Diagram of the solvent imprinting setup, reproduced from [22]. (B) Photograph of our solvent-vapour-assisted imprinter. (C) Photograph of the pressure-control setup.

Using our setup, the imprinting processes are as follows: the substrate coated with PBDTTT-CT film was first loaded face-to-face with the silicon template in the chamber. The chamber lid was then screwed tightly on top before an imprinting pressure of 5 bar was applied by the load cell. A chloroform vapour was generated by setting flow rates of 45 sccm for LINE A and 5 sccm for LINE B, and was kept flowing through the chamber for 30 minutes to fully swell the PBDTTT-CT film. An

imprinting pressure of 50 bar was then applied for 15 minutes to enable the structure on the silicon template imprinted to the polymer film. The chloroform vapour was then stopped, leaving only dry nitrogen (LINE B only) to purge the chamber for 1 hour. Finally the imprinting pressure was brought to zero. The chamber was opened and the PBDTTT-CT film was separated from the silicon template.

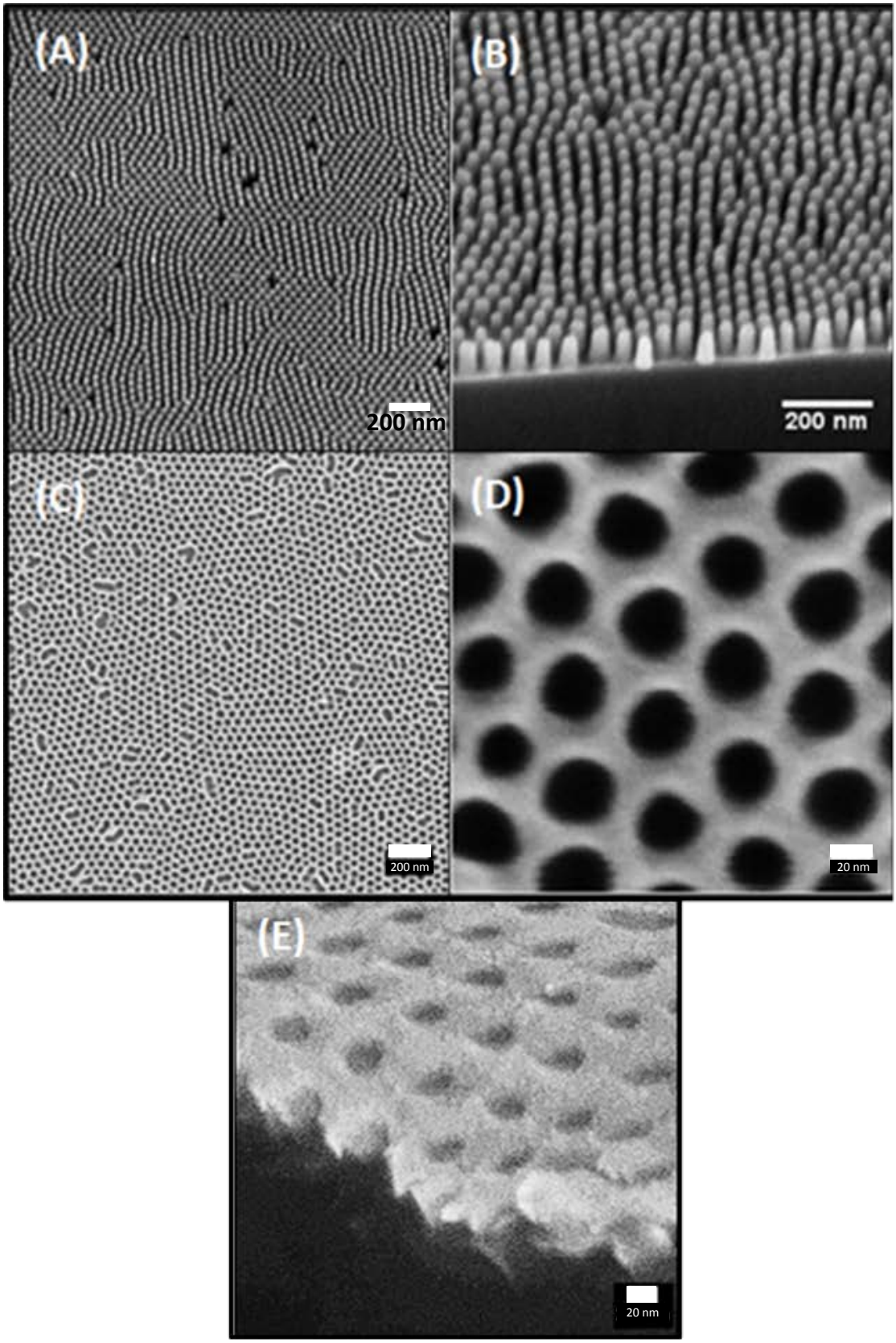

Figure 4.5 SEM images of the silicon template fabricated from copolymer lithography: (A) top-view image (B) 45° image. SEM image of the PBDTTT-CT nanostructures: (C) top-view (D) enlarged top-view (E) 45° image.

SEM images of the silicon template used are shown in Figure 4.5 (A) (B). The templates are in size of 1.2*1.2 cm^2, and highly reproducible. The fabrication processes are scalable, so we can make multiple templates at the same time. To facilitate the demolding of the templates after imprinting, we purposely improve the side-angle of the pillars by adjusting the silicon-etching parameters. The imprinted PBDTTT-CT structure is shown in Figure 4.5 (C) (D) (E).

4.3.2 PEDOT:PSS nanostructure

A 50-nm feature-sized silicon template was fabricated as described in Section 4.2, but with a longer-chain PS-b-PMMA polymer. The top-view and the 45°-view SEM images of the template are shown in Figure 4.6 (A-B). The PEDOT:PSS films were prepared by spin-coating PEDOT:PSS aqueous solution (Clevios P VP Al 4083) on ITO/glass substrates at 1500 rpm for 2 min, resulting in film thicknesses of ~70 nm. The films were annealed at 150 ^oC for 30 min under a nitrogen atmosphere.

PEDOT:PSS does not have a well-defined glass transition [23], and is not soluble in organic solvents, so we used water as the swelling solvent. We used the same processes as in Section 4.3.1, except water was used in place of chloroform. The imprinting result is shown in Figure 4.6 (C) (D). A nano-structured PEDOT:PSS film was successfully imprinted with feature size as small as ~50 nm, and height of ~70 nm.

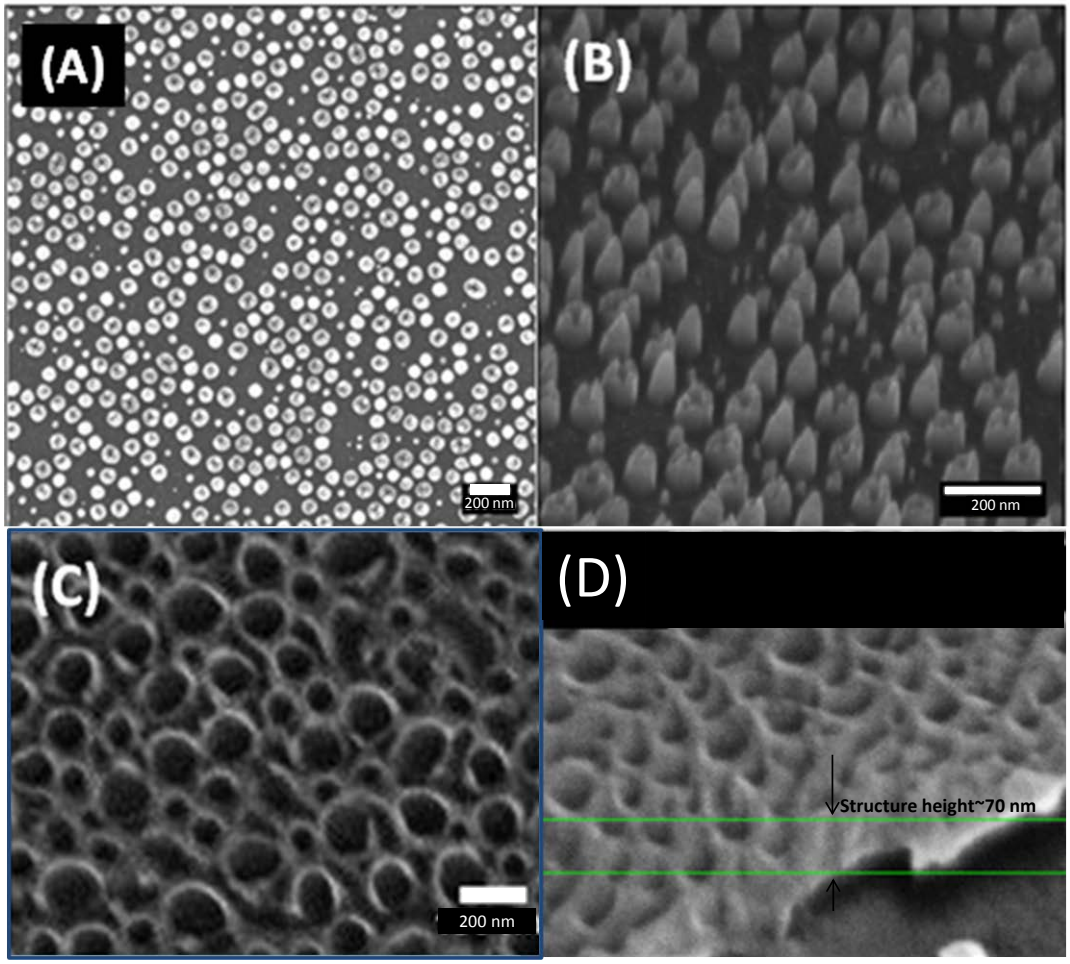

Figure 4.6 SEM image of silicon template fabricated by diblock copolymer lithography: (A) top-view, (B) 45°-view; SEM image of the silicon template SEM image of imprinted PEDOT:PSS patterns: (C) top-view, (D)45°-view.

4.3.3 TiO_2 nanostructure

TiO_2 is a hard metal oxide; it is not soluble in any solvent, it does not have a glass transition and has a melting point of ~1800 ^oC. Therefore, it is not possible to direct pattern TiO_2 by imprinting. Hence, we first fabricate the polystyrene patterns on the TiO_2 film by nanoimprinting, followed by an extra step of dry etching to enable the pattern transferred to the TiO_2 film.

Detailed fabrication steps:

The silicon template was prepared in the same way as in Section 4.2. The template was replicated into a perfluoropolyether (PFPE) soft mold following the methods in literature [24]. This replication is important to enable uniform patterning

of a ultra-thin polystyrene film, and the PFPE mold was made as follows: PFPE-dimethacrylate (PFPE-DMA, Solvay Solexis Fluorolink MD700) was mixed with a photoinitiator–2, 2-diethoxyacetophenone (Sigma Aldrich), at a mixing ratio of 1% w/w (photoinitiator to PFPE-DMA). The mixture liquid was mechanically agitated for 10 min to form a clear liquid. Several drops of the mixture liquid were spread on surface of the silicon template. In a chamber having been purged with nitrogen for 10 min, the template covered with the liquid was exposed to a 365 nm UV lamp for 30 min, to enable a crosslinking reaction that is detailed in the literature [25]. The resultant mold was peeled off the silicon template by sharp tweezers.

40 nm TiO_2 films were prepared by a sol-gel method [26]. The precursor solution was prepared by adding 2M hydrochloric acid (0.35 mmol, 17.5 μL) in 1.25 mL ethanol dropwise to a solution of titanium (IV) isopropoxide (Sigma Aldrich, 0.60 mmol, 175 μL) in 1.25 mL ethanol while vigorously stirring. The resulting solution was used freshly and was spin-coated onto ITO substrates at 2000 rpm. The resultant films were annealed in air at 500 ^{o}C for 30 min.

10-nm-thick polystyrene films were prepared on the TiO_2 substrates by spin-coating polystyrene solution in toluene (6 mg/ml, molecular weight 10K), at 4000 rpm for 1 minute. Polystyrene nanopillars or nano-holes were then fabricated by imprinting the polystyrene film at a temperature of 140 °C and at an imprinting pressure of 20 bar for 3 min, using the PFPE mold and with a commercial Obducat imprinter. Transfer of the polystyrene pattern into the TiO_2 film was performed by dry etching with a CHF_3/CH_4 plasma using an Oxford ICP 80 instrument.

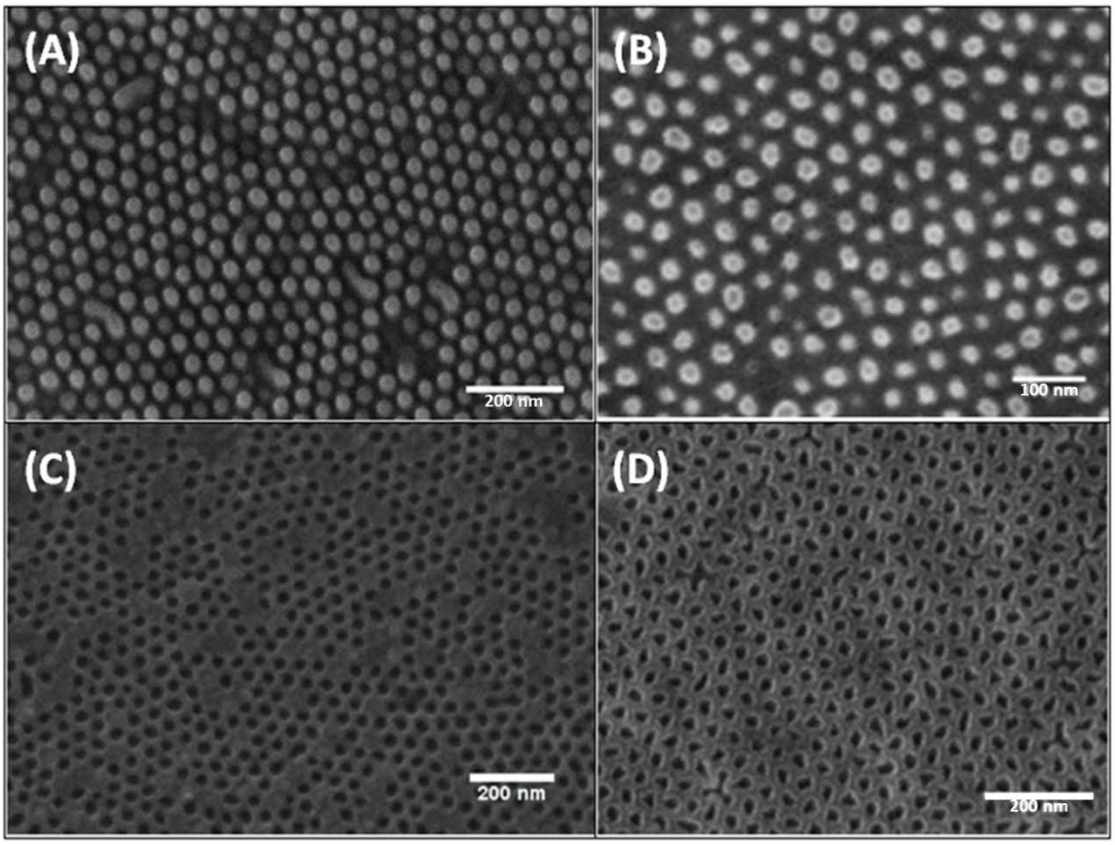

Figure 4.7 Top-view SEM images of (A) polystyrene dots on the TiO_2 substrate. (B) TiO_2 pillars fabricated from the polystyrene dots. (C) polytyrene holes on the TiO_2 substrate. (D) TiO_2 nanoholes fabricated from the polystyrene holes.

The imprinted polystyrene pillars and holes are shown in Figure 4.7(A)(C). We optimized the recipe for CHF_3/CH_4 plasma etching, to enable best nanostructure sharpness. The fabricated TiO_2 nanopillars and nanoholes are shown in Figure 4.7(B)(D). The heights of the structures were 10-20 nm, as measured by AFM.

4.4 A nanostructured PBDTTT-CT/$PC_{70}BM$ solar cell

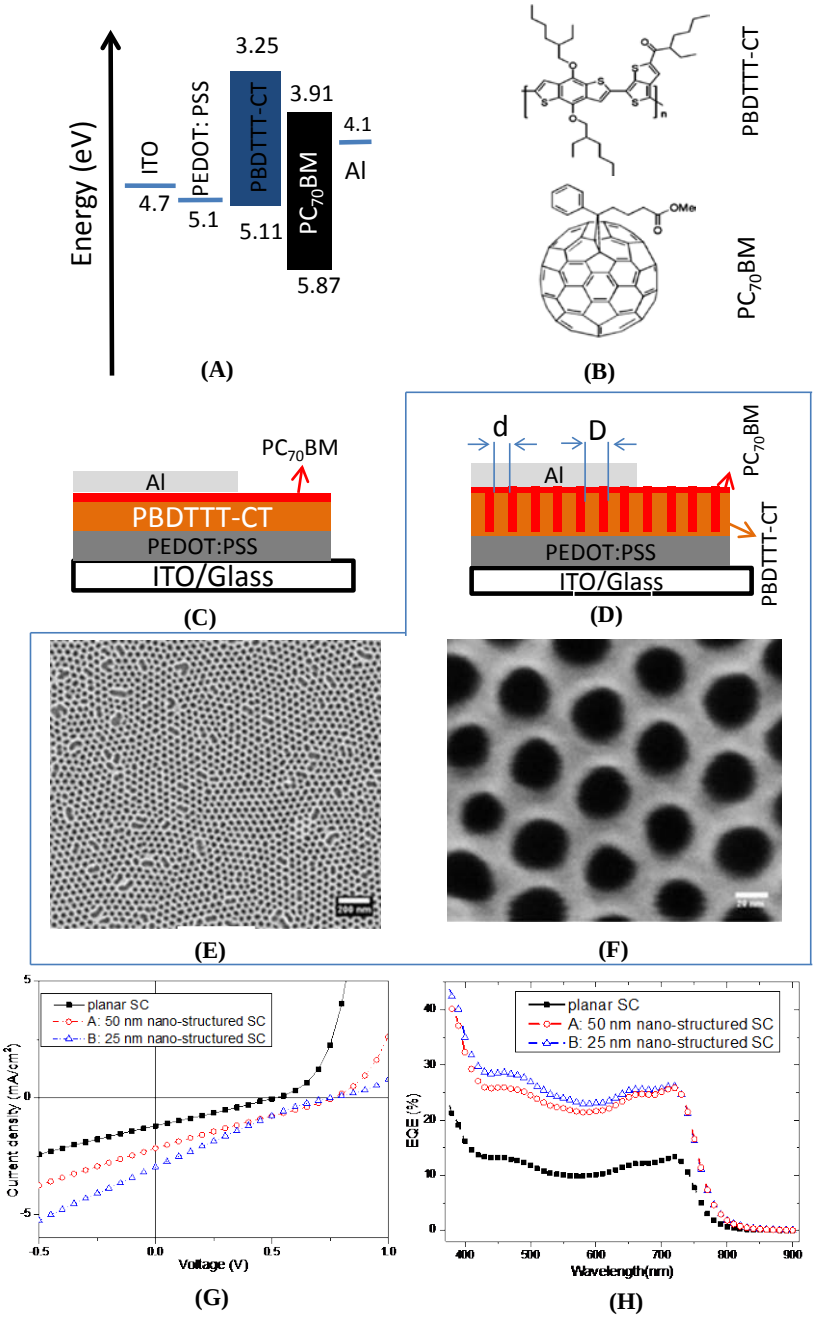

Figure 4.8 (A) Energy diagram of a PBDTTT-CT/$PC_{70}BM$ solar cell. (B) Chemical structure of PBDTTT-CT and $PC_{70}BM$. (C) Device structure of a bilayer PBDTTT-CT/$PC_{70}BM$ solar cell. (D) Device structure of a nanostructured PBDTTT-CT/$PC_{70}BM$ solar cell. (E) Top-view SEM image of PBDTTT-CT nano-structure fabricated in Section 4.3. Scale bar represents 200 nm. (F) Closer view of the PBDTTT-CT nanostructure, scale bar is 20 nm (G) Light IV curve of planar and nano-structured PBDTTT-CT/$PC_{70}BM$ solar cell. (H) EQE spectrum of the planar and the nano-structured solar cells.

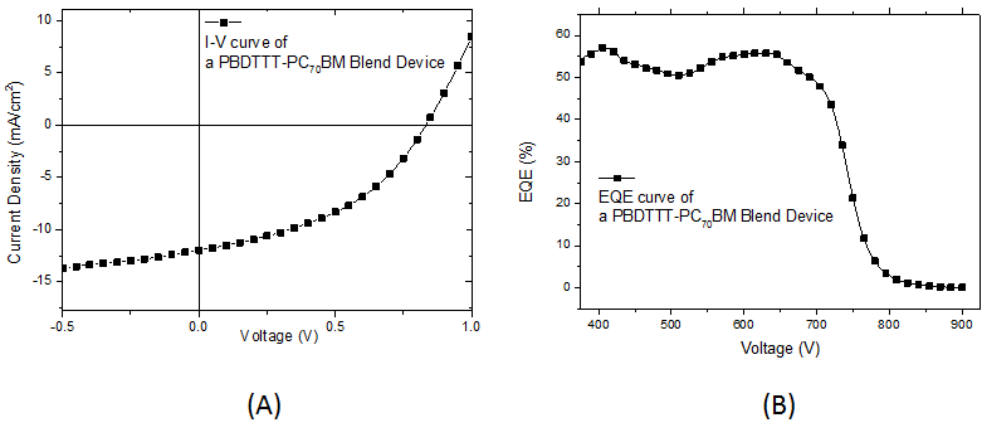

Figure 4.9 (A) Light IV curve of a bulk-heterojunction PBDTTT-CT/$PC_{70}BM$ solar cell. (B) EQE spectrum of a bulk-heterojunction PBDTTT-CT/$PC_{70}BM$ solar cell.

Our device structure (Fig. 4.8 (A)) employed a 25 nm-thick PEDOT:PSS film as the hole-transport layer, PBDTTT-CT film as the donor layer, $PC_{70}BM$ film as the acceptor layer and a 100 nm-thick aluminium film as the top electrode. The chemical structures of PBDTTT-CT and $PC_{70}BM$ are shown in Figure 4.8(B).

The illustration of the morphology of the planar device and the nano-structured device are shown in Figure 4.8 (C) and (D) respectively. *d* refers to the size of the feature, *D* refers to the period of the feature.

For the planar device, the active layer was fabricated by spin-coating a 40 nm PBDTTT-CT film from 10 mg/ml PBDTTT-CT solution in chlorobenzene at 2000 rpm for 1 min. The absorbance of this film at the first absorption peak is ~0.2. A $PC_{70}BM$ layer was spin-coated on top of the PBDTTT-CT film from a 2 mg/ml $PC_{70}BM$ solution in an orthogonal solvent, 1, 4–dioxin, at 700 rpm for 1 min, resulting in an average film thickness of 10 nm.

For the nano-structured device, the polymer layer was a nano-imprinted PBDTTT-CT film. One nanostructure, ‘A’, is shown in the SEM image in Figure 4.7 (E) and (F). The nanohole structures uniformly covered the entire substrate, with a hole diameter of ~25 nm and hole period of ~50 nm. The depth of these nano-holes was ~30 nm, as confirmed by both AFM and the 45° SEM image. Considering the starting film thickness is 40 nm, it is likely the nanoholes did not penetrate through the PBDTTT-CT film. The other nanostructure, ‘B’, had ~50 nm diameter holes with period of ~100 nm. On both the ‘A’ and ‘B’ nanostructures, $PC_{70}BM$ films were

spin-coated under the same condition as in the planar device. For the bulk heterojunction device C, the active layer was spin-coated at 2000 rpm from 30 mg/ml PBDTTT-CT/$PC_{70}BM$ chlorobenzene solution with 3% 1,8-diiodooctane as additive. All the device was evaporated with 100 nm aluminum as top electrode.

We tested the performance of the solar cells under nitrogen, and as shown in Figure 4.8(G) and (H). Both the short-circuit photocurrent and open-circuit voltage were improved in nano-structured solar cells, compared to the planar solar cell. Figure 4.8 (H) shows that the EQEs were substantially improved over the entire spectrum, with an EQE of ~27% at 720 nm and ~45% at 380 nm in the 25 nm structured solar cell, compared to 14% and 22% in planar solar cells, respectively.

We note that, performances of the plane structure and the bulk heterojunction structure are reproducible in every pixel. For the nanostructured device we picked up the best performing devices to represent uniformly imprinted devices. Some pixels of imprinted devices exhibit very low performance mainly because of the leakage route through the location where PBDTTT-CT film is peeled off while imprinting.

	d (nm)	D (nm)	V_{oc} (V)	J_{sc} (mA/cm^2)	FF (%)	PCE (%)	$\Delta PCE/PCE_{plane}$
Plane Structure	-	-	0.52	1.20	26.00	0.16	-
Device A	50	100	0.76 (46%)	2.16 (96%)	25.19	0.41	156%
Device B	25	50	0.76(46%)	2.96 (147%)	22.26	0.50	213%
Device C	-	-	0.83	11.9	42.4	4.2	

Table 4.1 Photovoltaic performance of the planar and the nano-structured PBDTTT-CT/$PC_{70}BM$ solar cell. The values in the brackets indicate the percent of performance improvement over the planar structure.

The performance parameters are summarized in Table 4.1. Devices A and B have similar improvement of 46% in open-circuit voltage. The short-circuit current and the power conversion efficiency were improved by 96% and 156% respectively in device A, and 147% and 213% respectively in device B.

We calculated the increase of interfacial area of the 30 nm high structures. The enhancement of short-circuit current is consistent with the increase of interfacial area by 54% in device A and 113% in device B, compared to the planar cell. This indicates more excitons were able to reach the interface.

We noticed that performance of nano-imprinted devices is still much lower than

the bulk heterojunction device (Device C), indicating we are still far from an ideal bulk-heterojunction. Several factors are currently limiting our PBDTTT-CT/$PC_{70}BM$ solar cell performance: 1. the height of the nanostructures is not large enough to match the optical absorbance length; 2. $PC_{70}BM$ does not have good solubility in the dioxin solvent, thus rendering it difficult to spin-coat a thick and continuous film. 3. Dioxin does not wet well on the PBDTTT-CT film making it difficult to infiltrate PCBM into the nano-holes.

4.5 Patterning of singlet fission materials

Pentacene is a highly efficient singlet fission material that shows a triplet yield close to 200% with a dynamic time scale of ~80 fs [27, 28]. Previous research has realized a pentacene solar cell with EQE above 100%. However, in their optimized pentacene solar cell, the 40 nm pentacene film only absorbs 30% of the incident light at the peak of its absorption spectrum [11-13]. While thicker pentacene film does not match the diffusion length of the triplets, a nano-structured pentacene film is favorable for the further efficiency enhancement.

TIPS-pentacene shows a triplet yield of 200% in concentrated solutions [29] and a triplet yield of 144% in thin films [30]. However, early device research shows only ~15% EQE [31] Lately, PbSe quantum dots were reported by Yang et al. to be a good acceptor for TIPS-pentacene. In a bilayer solar cell, EQEs up to 60% in the TIPS-pentacene absorption range were achieved, with an internal quantum efficiency of 170%. In order to realise this high performance, the TIPS-pentacene film has to be as thin as 20 nm, limiting the absorbance of light in this singlet fission material. Thus by introducing nanostructure to this architecture, it may be possible to enable optimized solar cell to have higher absorption in TIPS-pentacene, and have higher external quantum efficiency.

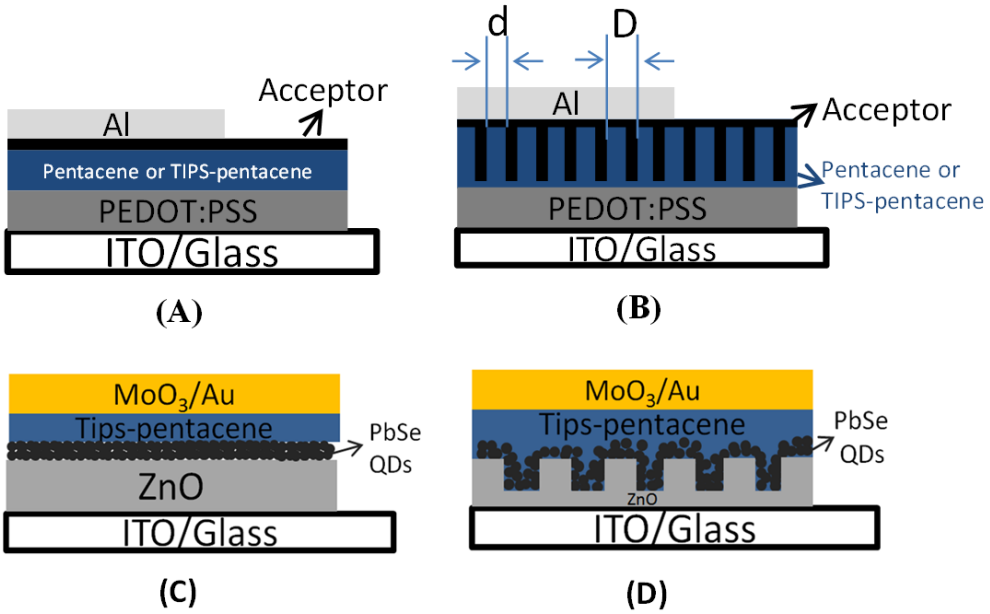

Figure 4.10 Device architectures of (A) a planar normal structure singlet fission solar cell (B) a nano-structured normal structure singlet fission solar cell (C) a planar inverted singlet-fission solar cell (D) a nano-structured inverted singlet-fission solar cell.

Figure 4.10 shows the two possible methods to introduce nanostructure to a pentacene solar cell or a TIPS-pentacene solar cell. For a normal structure solar cell (Figure 4.10 (A) (B)), we need to pattern pentacene or TIPS-pentacene. For an inverted structure solar cell (Figure 4.10 (C) (D)), we need to pattern ZnO or PbSe QDs.

4.5.1 Pentacene nanostructure

Pentacene is not soluble and does not have a glass transition. However, pentacene is an organic material that is softer than inorganic materials such as silicon, so we can change the topography of pentacene films by applying strong forces using hard templates and at elevated temperature.

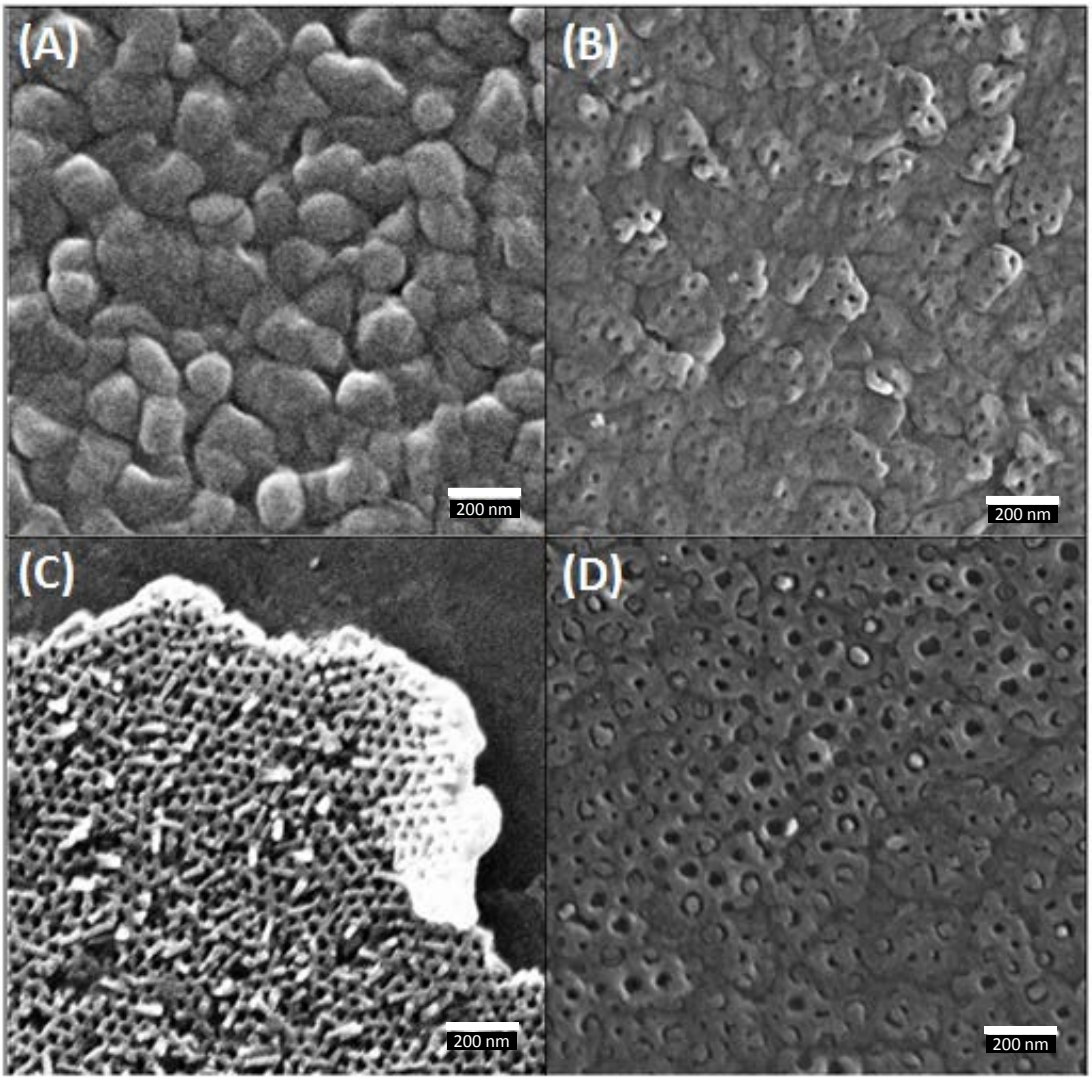

Figure 4.11 Top-view SEM images of (A) the as-deposited pentacene film; (B) the pentacene structure imprinted with a soft PFPE template; (C) the pentacene structure imprinted with a 25-nm feature-sized silicon template; (D) the pentacene structure imprinted with a 50-nm feature-sized silicon template.

50-nm-thick pentacene films were first prepared by themal evaporation. The film were composed of 100-200 nm grains as shown in Figure 4.11 (A). We first imprinted the pentacene films with a PFPE soft mold at pressure of 40 bar and temperature of 160 ^{o}C for 10 min in air. As shown in Figure 4.11 (B), the imprinted pentacene structure fully covered the film with no distortion or peeling off. However the structure was very shallow. Then hard silicon templates with different feature sizes were used and the pentacene films were imprinted at pressure of 100 bar and temperature of 160 ^{o}C for 10 min in air. The resultant films are shown in Figure

4.11(C)(D), They have deeper and sharper features but large areas of the film were peeled off.

Due to the peeling off, we were not able to make these pentacene nanostructures into solar cells. Also, pentacene undergoes photo-oxidation in air [32, 33], making our patterning method not suitable for device fabrication.

4.5.2 TIPS-pentacene nanostructures

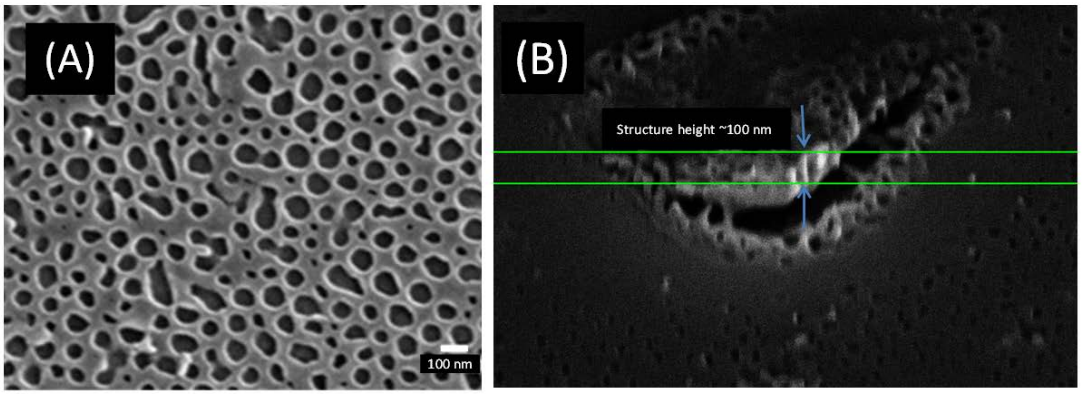

Figure 4.12 SEM images of the imprinted TIPS-pentacene: (A) top-view (B) 45°-view

TIPS-pentacene is a small molecule that does not have a glass transition and cannot be directly thermally imprinted, thus we show here patterning of it can be done by solvent-vapour-assisted imprinting. ~100 nm TIPS-pentacene films were spin-coated on ITO/glass substrates. Chloroform was used as the swelling solvent and imprinting was carried out under the same condition as in Section 4.3.1. As shown in Figure 4.12 (A) (B), sharp structures were successfully fabricated, with a feature size of 50-100 nm and height >100 nm.

We had difficulty to fabricate these TIPS-pentacene structure into solar cells, because they are soluble in most common solvents, and so far other than PbSe or PbS colloidal quantum dots, no suitable acceptor for TIPS-pentancene has been found [34].

4.6 A singlet fission solar cell based on ZnO pillars

In an effort to fabricate inverted-structure singlet fission solar cells, we start from fabricating reliable ZnO structure. We show that nanostructured PbSe and TIPs-pentacene layers are sucessfully deposited on top, which enables the improvement of performance in the nano-structured singlet fissio solar cell.

4.6.1 Colloidal lithography and fabrication of ZnO pillars

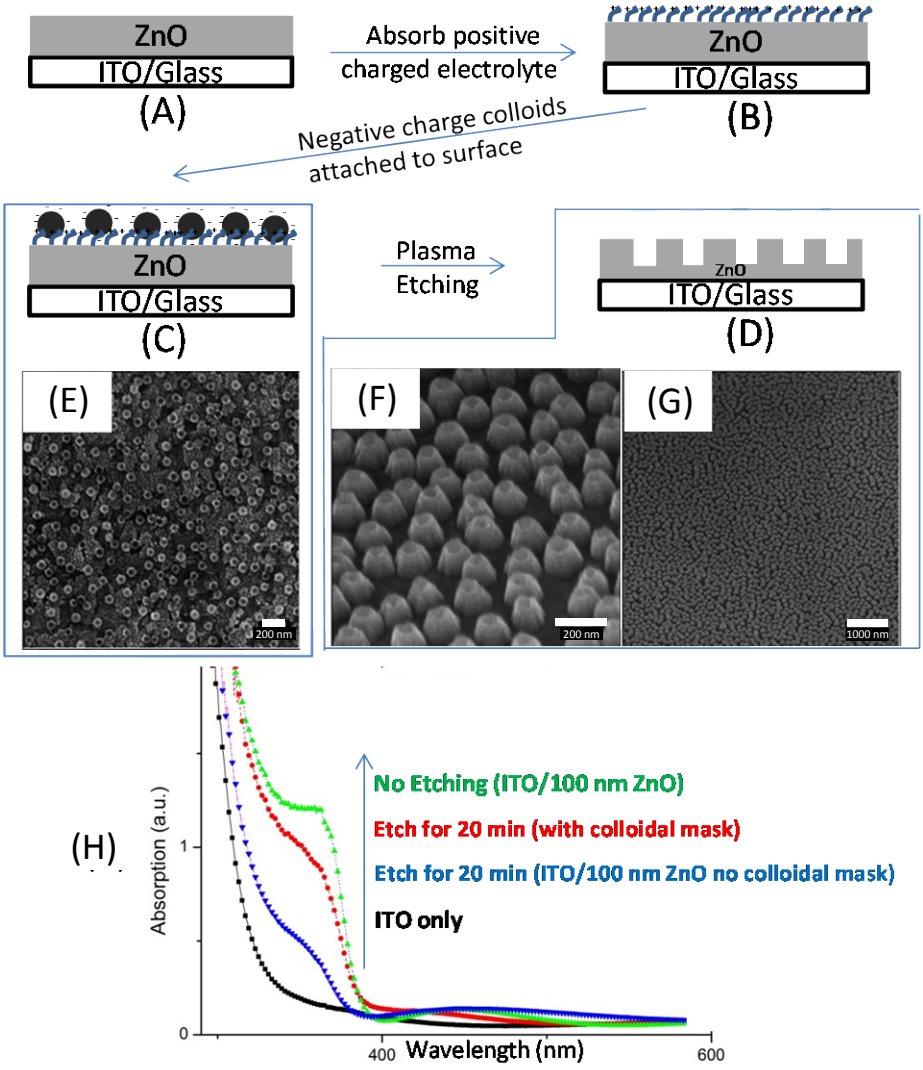

Figure 4.13 (A)-(D) Fabrication processes of ZnO nanostructure based on colloidal lithography. (E) Top-view SEM image of the ZnO nano-pillars fabricated from PS colloidal mask. (F) 45° SEM image of the ZnO nano-pillars. (G) 45° SEM image of the ZnO nanopillars in larger area. (H) UV-vis spectra of ZnO films under the etching conditions as marked.

150 nm thick ZnO film was prepared by atomic layer deposition on ITO/glass substrates, followed by annealing at 350 ^{o}C for 30 min in air. The ZnO film was firstly masked with polystyrene arrays which are prepared as reported in [35]. This method forms randomly-distributed polystyrene-sphere arrays on oxide surface through electrostatic forces. The preparation process is as follows: A positively charged polyelectrolyte (polydiallyldimethylammonium (PDDA), 0.2 wt% in deionized water) solution was dropped on to the ZnO film, followed by rinsing with DI water to remove excess PDDA. The modified ZnO surface is illustrated in Figure 4.13 (B). After the substrate was dried in a N_2 stream, a water suspension containing negatively charged polystyrene particles (sulfate latex, 0.2% in DI water) was dropped onto the substrate, kept for 30 seconds and then dried in a N_2 stream. Resulted film structure is illustrated in Figure 4.13 (C). The substrates were then characterized by SEM, the top view SEM image is shown in Figure 4.13 (E).

With the polystyrene-sphere array as the etching mask, plasma etching (Ar/CH_4) was used to transfer the array structure into the ZnO film, followed by O_2 plasma cleaning to remove excessive polystyrene and polyelectrolyte. Resulted ZnO structure is illustrated in Figure 4.13 (D). The SEM images are shown in Figure 4.13 (F) (G).

The optimized ZnO etching recipe is 10 sccm CH_4/10 sccm Ar at a chamber pressure of 5 mTorr, a RIE power of 150 W and a chamber bias of 145 V. This recipe gave an etching rate of 5 nm/min for ZnO, and a deposition rate of 2 nm/minute on the polystyrene spheres. By processing for 20 min, we obtained 100 nm high and 80 nm wide uniformly distributed teepee-like pillars with a period of ~200 nm.

UV-vis measurement was performed to evaluate the change of the ZnO absorption. As Figure 4.13 (E) shows, a clear absorption peak at ~360 nm appears in all the etched samples, indicating the absorption property of ZnO was well preserved after dry etching. The absorption spectrum of 20-min-etched samples done on ZnO film without the polystyrene spheres, indicates the sample still had a thin residue layer of ZnO.

4.6.2. A nano-structured ZnO/PbSe/TIPS-pentacene solar cell

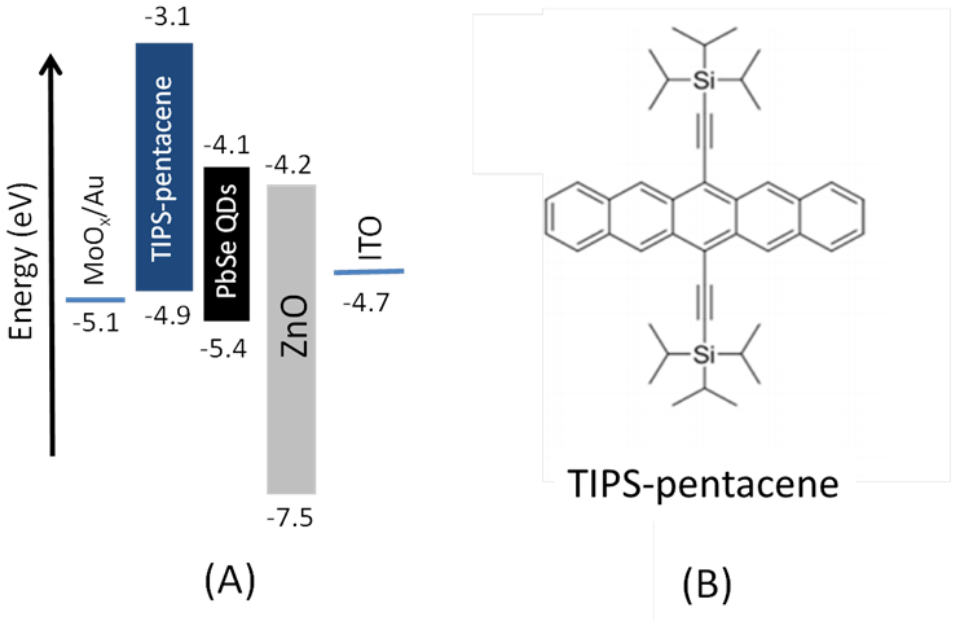

Figure 4.14 (A) Energy diagram of a TIPS-pentacene/PbSe QDs/ZnO nanopillar solar cell. (B) Chemical structure of TIPS-pentacene.

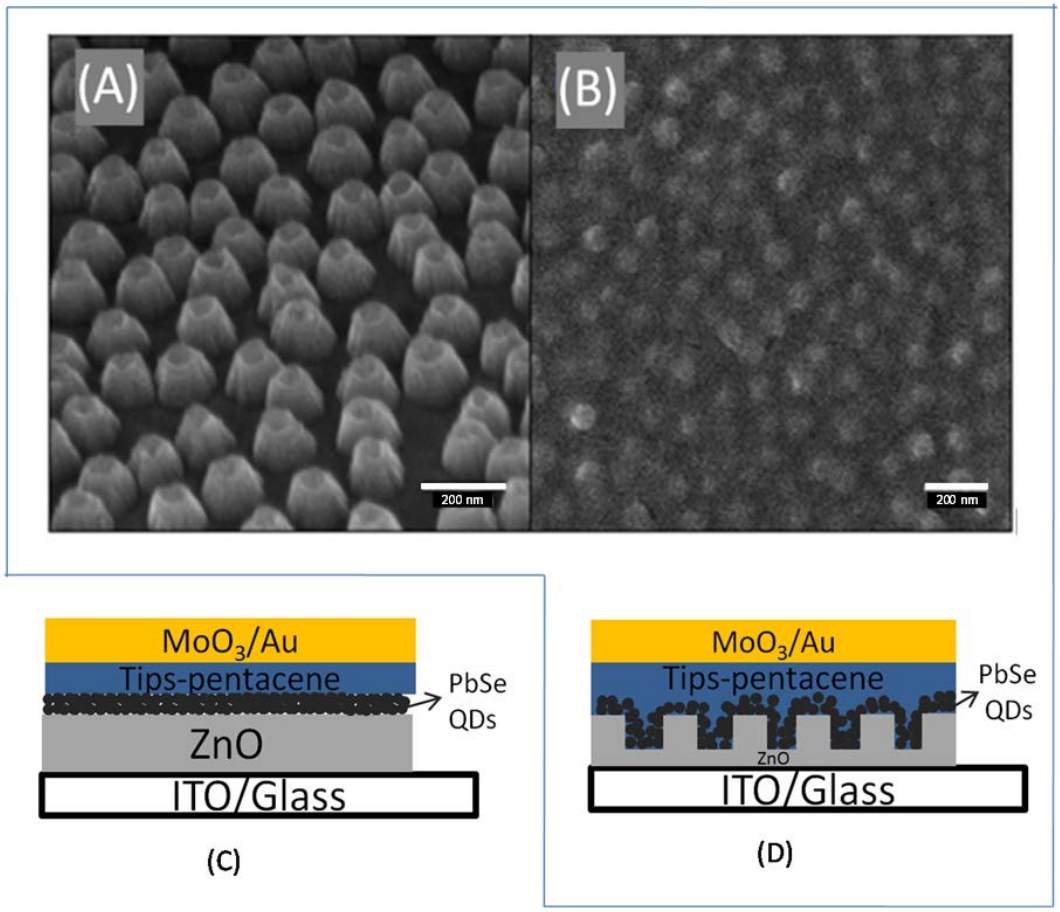

Figure 4.15 (A) 45° SEM image of a ZnO nano-pillar structure. (B) Top-view SEM image of the PbSe layer. (C) Device structure of a planar ZnO/PbSe/TIPS-pentacene solar cell. (D) Device structure of a nano-structured ZnO/PbSe/tips-pentacene solar cell.

Our device structure (Figure 4.14(A)) consists of an ITO film as the anode layer, a ZnO film as the acceptor layer, a PbSe quantum dot film as the intermediate layer and a TIPS-pentacene film as the top donor layer.

The fabrication and test of these devices were carried out by Le Yang.

ZnO pillar arrays were prepared as described in Section 4.5.2 (Figure 4.15 (A)). The ‘teepee’ like ZnO columns have an average diameter of ~80 nm, an average distance of ~200 nm and height of ~100 nm, and they were uniformly distributed. Based on this ZnO layer we constructed devices in the following steps: A solution of the crosslinker 1, 4-benzenedithiol (BDT) in acetonitrile (0.10-0.23% v/v) was first dropped on the ZnO layer and held for 5-10s to absorb a thin layer of crosslinker, before excessive BDT was washed off by acetonitrile. PbSe quantum dot film (band

gap 0.95 eV, synthesized by Le Yang [34], 25 mg/ml in octane) was spin-coated for 1500 rpm for 15 s, followed by soaking with BDT for 10s, and sequentially rinsed by acetonitrile and octane to remove free ligands and unlinked nanocrystals. This process was repeated twice to enable deposition of ~40 nm PbSe films. As shown in the SEM image of Figure 4.15 (B), the nanostructures in ZnO columns were successfully transferred to the PbSe layer. Thus increased interfacial areas exist on both the ZnO/PbSe and the PbSe/tips-pentacene interfaces. 2 mg/ml TIPS-pentacene in chloroform was spin-coated at 1500 rpm for 20s, resulting in a TIPS-pentacene film of ~20 nm. Then MoO_x/gold anode was thermally evaporated under vacuum at a pressure of 5×10^{-6} mbar. The devices were legged and encapsulated, before testing in air. The complete device structures of the planar and nano-structured devices are shown in Figure 4.15 (C) and (D) respectively.

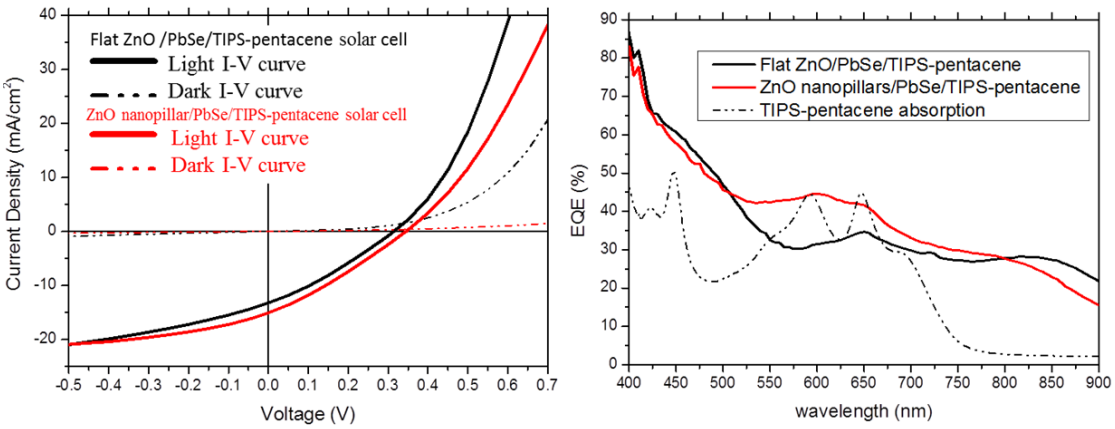

Figure 4.16 (A) Light IV and dark IV curves of the planar and the nano-structured ZnO/PbSe/Tips-pentacene solar cells. (B) EQE spectra of the planar and the nano-structured ZnO/PbSe/TIPS-pentacene solar cells.

	V_{OC} (V)	J_{SC} (mA/cm^2)	FF (%)	PCE (%)	$\Delta PCE/PCE_{plane}$
Planar structured	0.31	13.24	29.37	1.22	-
Nano-structured	0.35	15.09	28.60	1.49	22 %

Table 4.2 Photovoltaic performance of planar and nano-structured ITO/ZnO/PbSe/TIPS-pentacene/MoO_3/Au solar cells

We tested the performance of our devices. In Figure 4.16(A) the device performance of the nano-structured device shows improvement in both V_{oc} and J_{sc}, resulting in an overall 22% improvement of the power conversion efficiency. We notice that the dark current of nano-structured device is half of that in a planar device, which might be due to the electronic damage by the dry etching of the surface of ZnO.

Note: the data are selected from the best-performing device from the 8 pixels in each structure. We also calculated the average PCEs which are 1.16% and 1.32% for plane-structured and nano-structured devices, respectively.

The EQE spectra are shown in Figure 4.16(B). The EQE of the nano-structured solar cell shows an improvement between 520 nm and 700 nm over the planar solar cell, the range of which overlaps with the two exciton absorption peaks of TIPS-pentacene. This possibly indicates the improvement of triplet exciton collection in TIPS-pentacene.

In summary, we have shown here a solar cell based on substrates of ZnO columns. Two layers of PbSe and TIPS-pentacene were sequentially deposited and have both their interfacial areas increased. Compared to the planar device, the nanostructure device had its triplet exciton collection improved.

4.7 Dry etching recipes

No.	Targeted materials	Gas 1 (sccm)	Gas 2 (sccm)	Chamber Pressure (mTorr)	RIE power (W)	ICP power (W)	Etching rate (nm/min)
1	alumina	Ar(20)		1	90	250	2
2	PS-r-PMMA copolymer	O_2(20)		12	30	0	30
3	Silicon	C_4F_8(50)	SF_6(25)	5	11	150	5
4	Silicon	SF_6(15)	O_2(15)	2	30	0	60
5	TiO_2	CHF_3(15)	CH_4(5)	5	30	500	4
6	ZnO	Ar(10)	CH_4(10)	5	150	0	5

Table 4.2 Summary of the dry etching recipes used in this chapter

References

1. Watkins, P.K., Walker, A.B., and Verschoor, G.L., *Dynamical Monte Carlo modelling of organic solar cells: The dependence of internal quantum efficiency on morphology.* Nano Letters, **5**, 1814-1818(2005).
2. Cheyns, D., Vasseur, K., Rolin, C., Genoe, J., Poortmans, J., and Heremans, P., *Nanoimprinted semiconducting polymer films with 50 nm features and their application to organic heterojunction solar cells.* Nanotechnology, **19**, 424016(2008).
3. He, X., Gao, F., Tu, G., Hasko, D., Huttner, S., Steiner, U., Greenham, N.C., Friend, R.H., and Huck, W.T., *Formation of nanopatterned polymer blends in photovoltaic devices.* Nano Letters, **10**, 1302-1307(2010).
4. He, X., Gao, F., Tu, G., Hasko, D.G., Hüttner, S., Greenham, N.C., Steiner, U., Friend, R.H., and Huck, W.T., *Formation of Well-Ordered Heterojunctions in Polymer: PCBM Photovoltaic Devices.* Advanced Functional Materials, **21**, 139-146(2011).
5. Chen, D., Zhao, W., and Russell, T.P., *P3HT nanopillars for organic photovoltaic devices nanoimprinted by AAO templates.* ACS nano, **6**, 1479-1485(2012).
6. Lee, J., Jadhav, P., Reusswig, P.D., Yost, S.R., Thompson, N.J., Congreve, D.N., Hontz, E., Van Voorhis, T., and Baldo, M.A., *Singlet exciton fission photovoltaics.* Accounts of chemical research, **46**, 1300-1311(2013).
7. Mikhnenko, O.V., Ruiter, R., Blom, P.W., and Loi, M.A., *Direct measurement of the triplet exciton diffusion length in organic semiconductors.* Physical review letters, **108**, 137401(2012).
8. Lunt, R.R., Giebink, N.C., Belak, A.A., Benziger, J.B., and Forrest, S.R., *Exciton diffusion lengths of organic semiconductor thin films measured by spectrally resolved photoluminescence quenching.* Journal of Applied Physics, **105**, 053711(2009).
9. Irkhin, P. and Biaggio, I., *Direct imaging of anisotropic exciton diffusion and triplet diffusion length in rubrene single crystals.* Physical review letters, **107**, 017402(2011).

10. Najafov, H., Lee, B., Zhou, Q., Feldman, L., and Podzorov, V., *Observation of long-range exciton diffusion in highly ordered organic semiconductors.* Nature materials, **9**, 938-943(2010).
11. Tabachnyk, M., Ehrler, B., Bayliss, S., Friend, R.H., and Greenham, N.C., *Triplet diffusion in singlet exciton fission sensitized pentacene solar cells.* Applied Physics Letters, **103**, 153302(2013).
12. Congreve, D.N., Lee, J., Thompson, N.J., Hontz, E., Yost, S.R., Reusswig, P.D., Bahlke, M.E., Reineke, S., Van Voorhis, T., and Baldo, M.A., *External quantum efficiency above 100% in a singlet-exciton-fission–based organic photovoltaic cell.* Science, **340**, 334-337(2013).
13. Ehrler, B., Walker, B.J., Böhm, M.L., Wilson, M.W., Vaynzof, Y., Friend, R.H., and Greenham, N.C., *In situ measurement of exciton energy in hybrid singlet-fission solar cells.* Nature communications, **3**, 1019(2012).
14. Jadhav, P.J., Mohanty, A., Sussman, J., Lee, J., and Baldo, M.A., *Singlet exciton fission in nanostructured organic solar cells.* Nano letters, **11**, 1495-1498(2011).
15. Li, M. and Ober, C.K., *Block copolymer patterns and templates.* Materials Today, **9**, 30-39(2006).
16. Noshay, A. and McGrath, J.E., *Block copolymers: overview and critical survey*, academic press, INC(2013)
17. Thurn-Albrecht, T., Schotter, J., Kästle, G., Emley, N., Shibauchi, T., Krusin-Elbaum, L., Guarini, K., Black, C., Tuominen, M., and Russell, T., *Ultrahigh-density nanowire arrays grown in self-assembled diblock copolymer templates.* Science, **290**, 2126-2129(2000).
18. Mansky, P., Liu, Y., Huang, E., Russell, T., and Hawker, C., *Controlling polymer-surface interactions with random copolymer brushes.* Science, **275**, 1458-1460(1997).
19. Gay, G., Baron, T., Agraffeil, C., Salhi, B., Chevolleau, T., Cunge, G., Grampeix, H., Tortai, J., Martin, F., and Jalaguier, E., *CMOS compatible strategy based on selective atomic layer deposition of a hard mask for transferring block copolymer lithography patterns.* Nanotechnology, **21**, 435301(2010).

20. Guo, X., Zhang, M., Ma, W., Ye, L., Zhang, S., Liu, S., Ade, H., Huang, F., and Hou, J., *Enhanced Photovoltaic Performance by Modulating Surface Composition in Bulk Heterojunction Polymer Solar Cells Based on PBDTTT-C-T/PC71BM.* Advanced Materials, **26**, 4043-4049(2014).
21. Hou, J., Chen, H.-Y., Zhang, S., Chen, R.I., Yang, Y., Wu, Y., and Li, G., *Synthesis of a low band gap polymer and its application in highly efficient polymer solar cells.* Journal of the American Chemical Society, **131**, 15586-15587(2009).
22. Voicu, N.E., Ludwigs, S., Crossland, E.J., Andrew, P., and Steiner, U., *Solvent-Vapor-Assisted Imprint Lithography.* Advanced Materials, **19**, 757-761(2007).
23. Zhou, J., Anjum, D.H., Chen, L., Xu, X., Ventura, I.A., Jiang, L., and Lubineau, G., *The temperature-dependent microstructure of PEDOT/PSS films: insights from morphological, mechanical and electrical analyses.* Journal of Materials Chemistry C, **2**, 9903-9910(2014).
24. Williams, S.S., Retterer, S., Lopez, R., Ruiz, R., Samulski, E.T., and DeSimone, J.M., *High-resolution PFPE-based molding techniques for nanofabrication of high-pattern density, sub-20 nm features: a fundamental materials approach.* Nano letters, **10**, 1421-1428(2010).
25. Rolland, J.P., Hagberg, E.C., Denison, G.M., Carter, K.R., and De Simone, J.M., *High-Resolution Soft Lithography: Enabling Materials for Nanotechnologies.* Angewandte Chemie, **116**, 5920-5923(2004).
26. Carnie, M.J., Charbonneau, C., Davies, M.L., Troughton, J., Watson, T.M., Wojciechowski, K., Snaith, H., and Worsley, D.A., *A one-step low temperature processing route for organolead halide perovskite solar cells.* Chemical Communications, **49**, 7893-7895(2013).
27. Wilson, M.W., Rao, A., Clark, J., Kumar, R.S.S., Brida, D., Cerullo, G., and Friend, R.H., *Ultrafast dynamics of exciton fission in polycrystalline pentacene.* Journal of the American Chemical Society, **133**, 11830-11833(2011).
28. Rao, A., Wilson, M.W., Hodgkiss, J.M., Albert-Seifried, S., Bassler, H., and Friend, R.H., *Exciton fission and charge generation via triplet excitons in*

pentacene/C60 bilayers. Journal of the American Chemical Society, **132**, 12698-12703(2010).

29. Walker, B.J., Musser, A.J., Beljonne, D., and Friend, R.H., *Singlet exciton fission in solution.* Nature chemistry, **5**, 1019-1024(2013).
30. Ramanan, C., Smeigh, A.L., Anthony, J.E., Marks, T.J., and Wasielewski, M.R., *Competition between singlet fission and charge separation in solution-processed blend films of 6, 13-bis (triisopropylsilylethynyl) pentacene with sterically-encumbered perylene-3, 4: 9, 10-bis (dicarboximide) s.* Journal of the American Chemical Society, **134**, 386-397(2011).
31. Palilis, L.C., Lane, P.A., Kushto, G.P., Purushothaman, B., Anthony, J.E., and Kafafi, Z.H., *Organic photovoltaic cells with high open circuit voltages based on pentacene derivatives.* Organic Electronics, **9**, 747-752(2008).
32. Maliakal, A., Raghavachari, K., Katz, H., Chandross, E., and Siegrist, T., *Photochemical stability of pentacene and a substituted pentacene in solution and in thin films.* Chemistry of Materials, **16**, 4980-4986(2004).
33. Fudickar, W. and Linker, T., *Why triple bonds protect acenes from oxidation and decomposition.* Journal of the American Chemical Society, **134**, 15071-15082(2012).
34. Yang, L., Tabachnyk, M., Bayliss, S.L., Böhm, M.L., Broch, K., Greenham, N.C., Friend, R.H., and Ehrler, B., *Solution-Processable Singlet Fission Photovoltaic Devices.* Nano letters, **15**, 354-358(2014).
35. Fredriksson, H., Alaverdyan, Y., Dmitriev, A., Langhammer, C., Sutherland, D.S., Zäch, M., and Kasemo, B., *Hole–mask colloidal lithography.* Advanced Materials, **19**, 4297-4302(2007).

Chapter 5

This chapter was modified from a paper published [1]. The work was carried out in collaboration with Zhi-Kuang Tan, Dawei Di, May Ling Lai, Lang Jiang, and Jonathan Hua-Wei Lim, and supervised by Richard H. Friend and Neil C. Greenham. Guangru Li carried out most of the experiments. Guangru Li, Zhi-Kuang Tan and Dawei Di conceived the initial idea. May Ling Lai synthesized the perovskite materials. Lang Jiang suggested and supplied appropriate polymers. Jonathan Hua-Wei Lim did XRD characterization. Guangru Li, Zhi-Kuang Tan wrote the manuscript.

Efficient Light-Emitting Diodes based on Nano-Crystalline Perovskite in a Dielectric Polymer Matrix

Electroluminescence in light-emitting devices relies on the encounter and radiative recombination of electrons and holes in the emissive layer. In organometal halide perovskite light-emitting diodes, poor film formation creates electrical shunting paths, where injected charge carriers bypass the perovskite emitter, leading to a loss in electroluminescence yield. Here, we report a solution-processing method to block electrical shunts and thereby enhance electroluminescence quantum efficiency in perovskite devices. In this method, a blend of perovskite and a polyimide precursor dielectric (PIP) is solution-deposited to form perovskite nanocrystals in a thin-film matrix of PIP. The PIP forms a pinhole-free charge-blocking layer, while still allowing the embedded perovskite crystals to form electrical contact with the electron- and hole-injection layers. This modified structure reduces non-radiative current losses and improves quantum efficiency by 2 orders of magnitude, giving an external quantum efficiency of 1.2%. This simple technique provides an alternative route to circumvent film formation problems in perovskite optoelectronics and offers the possibility of flexible and high-performance light-emitting displays.

5.1 Overview

Solution processing of luminescent semiconductors presents a particularly attractive option for the low-cost fabrication of light-emitting devices. [2-5] Recent works on high-efficiency organometal halide perovskite photovoltaics have shown these materials to possess both the remarkable qualities of traditional semiconductors and the facile processability of organic semiconductors. [6-10] A new report on perovskite nanoparticles has further shown these materials to possess high photoluminescence quantum yield [11]. The perovskite materials also benefit from low cost and earth-abundance, and can be deposited at low temperatures under ambient conditions. More recently, bright and colour-controlled electroluminescence was reported in perovskite light-emitting diodes (PeLED), thereby opening up a potential range of display and lighting applications for these materials [12, 13]. However, the quantum efficiencies in these PeLED devices remain modest due to difficulties in the formation of uniform thin films.

Light emission occurs when injected electrons and holes meet in the perovskite layer and recombine radiatively. However, it is easy for injected charges to bypass the perovskite layer through pinholes in the thin films, leading to non-radiative current losses and a lower efficiency. Difficulties in the formation of uniform and pinhole-free perovskites are well known, due to the material's crystalline nature. This problem is further exacerbated by the sublimation of excess methylammonium halide precursor during thermal annealing, thereby leaving voids in the perovskite layer. An established technique to overcome this problem involves sequential or vapour deposition of the perovskite precursors [8, 14], although these methods only improve film formation and cannot completely eliminate pinholes.

In this chapter we fabricated efficient light-emitting diodes through the embedding of perovskite nanocrystals in a matrix of dielectric polymer. The perovskite nanocrystals form *in-situ* when a blend of perovskite precursor and polymer is deposited and annealed. The uniformly distributed perovskite nanocrystals provide good light emission, while the dielectric polymer fills in the surrounding voids to block non-radiative current losses.

5.2 Preparation of polymer/perovskite composite films

In order to select a polymer to blend with perovskite for the fabrication of LEDs, the polymer needs to meet several solubility criteria. The polymer needs to be soluble in N,N-dimethylformamide (DMF) and insoluble in chlorobenzene. Polyimide precursor (PIP) is the one fitting well to these criteria. The PIP (product number PI2525) was purchased from HD microsystems and was diluted into a concentration of 20 mg ml^{-1} in N-methyl-2-pyrrolidone before use.

Blend solutions were prepared by mixing 5 wt% $CH_3NH_3PbBr_3$ solutions and the diluted PIP solutions to give different weight ratios. The blend solutions were stirred at room temperature for 2 hours before use. The mixed solutions ranged from colourless to light-orange coloured depending on the blending ratio. The blend solutions were spin-coated at 3000 rpm for 30 s.

5.3 Composite film characterisation

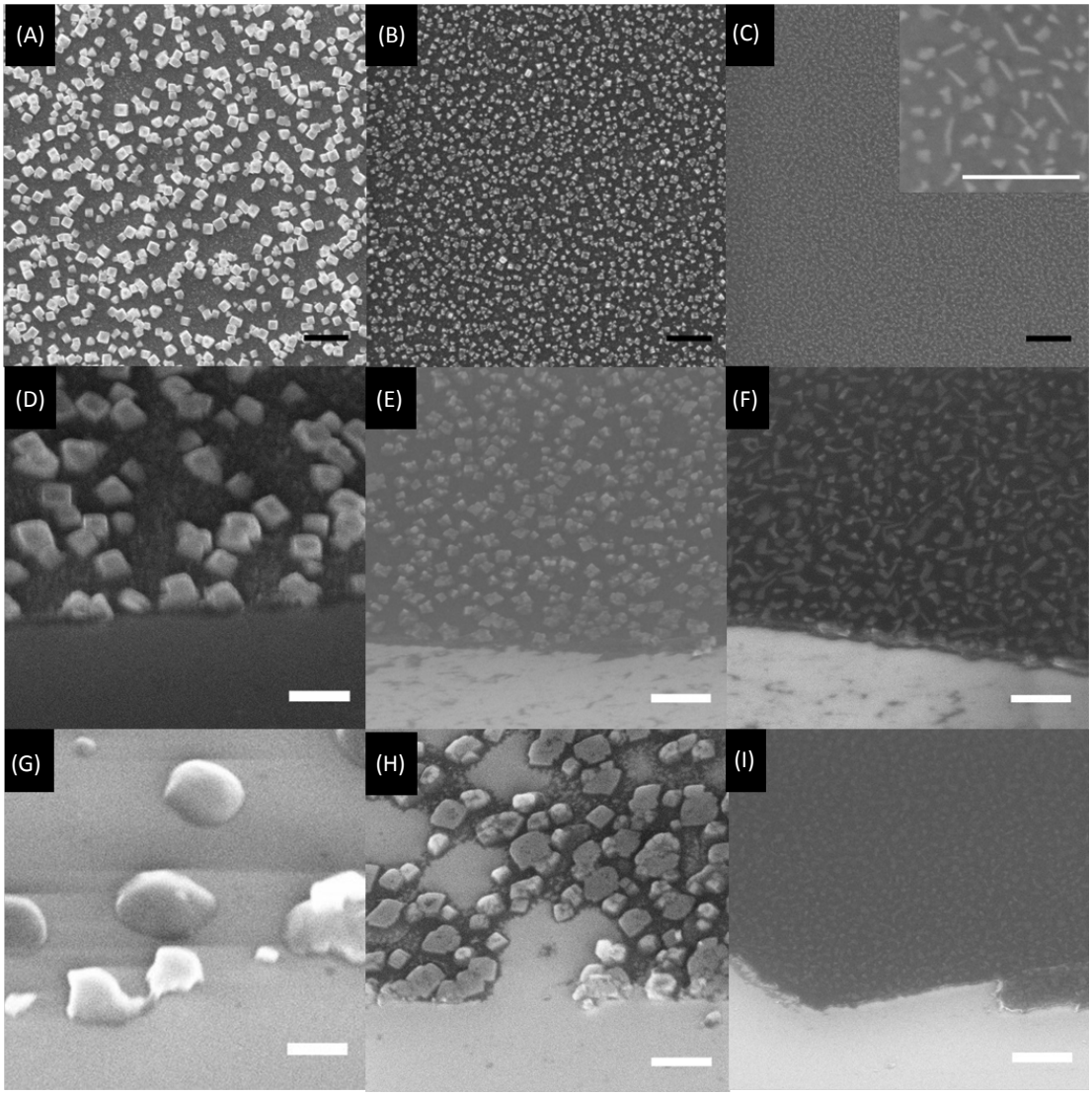

Figure 5.1 Top-view SEM images of (A) perovskite only, (B) 1/10 PIP/perovskite, (C) 1/2 PIP/perovskite on PEDOT-PSS coated silicon. Inset in (C) shows an enlarged image of 1/2 PIP/perovskite film. (D), (E) & (F) show 45° angled view of (A), (B) & (C), respectively. (G), (H) & (I) show 45° angled view of films spin-coated with the same solution in (A), (B) & (C), but on bare silicon substrate. All black scale bars represent 1 μm. All white scale bars represent 500 nm.

We studied the perovskite and PIP composite films using scanning electron microscopy (SEM). Figures 5.1(A), (B) & (C) show top-view SEM images of the perovskite-only, PIP: perovskite 1:10 w/w ratio and 1:2 w/w ratio films, respectively. Figures 5.1 (D), (E) & (F) show the corresponding SEM images of the scratched edge of each film, taken at an angle of 45°. The brighter areas represent perovskite since

they have a higher electron density than the surrounding polymer. The films in Figures 5.1(A) to (F) are deposited on a poly(3,4-ethylenedioxythiophene)-poly(styrenesulfonate) (PEDOT:PSS) substrate in order to ensure that the images are representative of the perovskite layers in the PeLED structures.

As shown in Figures 5.1(A) & (D), the perovskite-only "layer" consists of cuboid nanocrystals of approximately 250 nm in dimension, and they occupy only 33 % of the layer area. As previously explained, electrical current flowing through these empty areas contributes to a massive loss of device efficiency. In the 1:10 ratio film as shown in Figures 5.1(B) & (E), the addition of PIP causes the nanocrystal sizes to decrease to 100 nm, and the perovskite nanocrystals occupy approximately 27% of the film area. The nanocrystals shrink further to just 60 nm in the 1:2 ratio film, and occupy 28% of the area, as shown in Figures 5.1(C) & (F). It is unlikely that these nanoparticles were formed ready in the precursor solution, under the observation that these solutions are fully transparent. The nanoparticles must form in-situ in the processes of spin-coating and annealing. We are aware that this similar concept to form nanoparticle in-situ from a precursor was utilized in earlier work by Dowland et al. on polymer/nanoparticle hybrid solar cells [15].

From the 45° SEM images, which show the scratched edge of the films, we can clearly observe that the perovskite crystals are embedded in a uniform layer of polymer. The light grey area shows the bare silicon substrate where the film has been removed, the dark grey area shows the polymer layer, and the lighter cuboidal and polyhedronal objects within the polymer represent embedded perovskite crystals. This darker polymer layer could either be PEDOT: PSS or PIP. In order to differentiate between the two polymers, we took the 45° SEM images of perovskite films that are deposited on bare silicon substrates, as shown in Figure 5.1 (G), (H) &(I). Any polymer layers that form will therefore, unambiguously, be PIP. We note that the morphology of the perovskite crystals appear different when deposited on bare silicon as compared to those deposited on PEDOT: PSS. This is due to a change in the substrate surface properties, which influences the wetting and film formation process. In the 1:10 ratio film in Figure 5.1(H), the PIP polymer layer is shown to be incomplete in certain areas. In comparison, the 1:2 ratio film in Figure 5.1(I), shows a complete PIP polymer coverage with no signs of pinholes.

Through these SEM results, we can deduce that the perovskite nanocrystals form within a matrix of dielectric PIP in the blend films, and the insulating PIP polymer serves to block the electrical shunting paths. The thickness of the PIP polymer was determined to be 7nm and 30 nm in the 1:10 and 1:2 ratio films, respectively, as shown in the atomic force microscopy (AFM) measurements in Figure 5.2 (A)(B)(C). And the average thicknesses of the entire PIP-perovskite composite films are 11, 25, 33 nm for the perovskite-only, 1:10, and 1:2 weight ratio films, respectively.

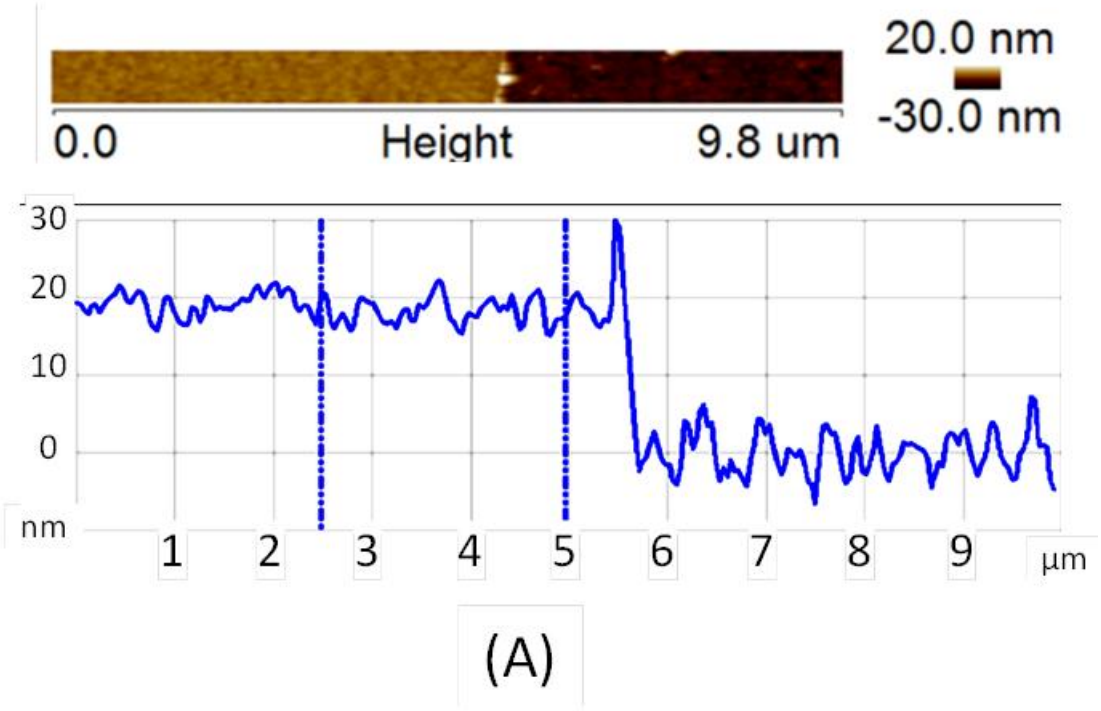

(A)

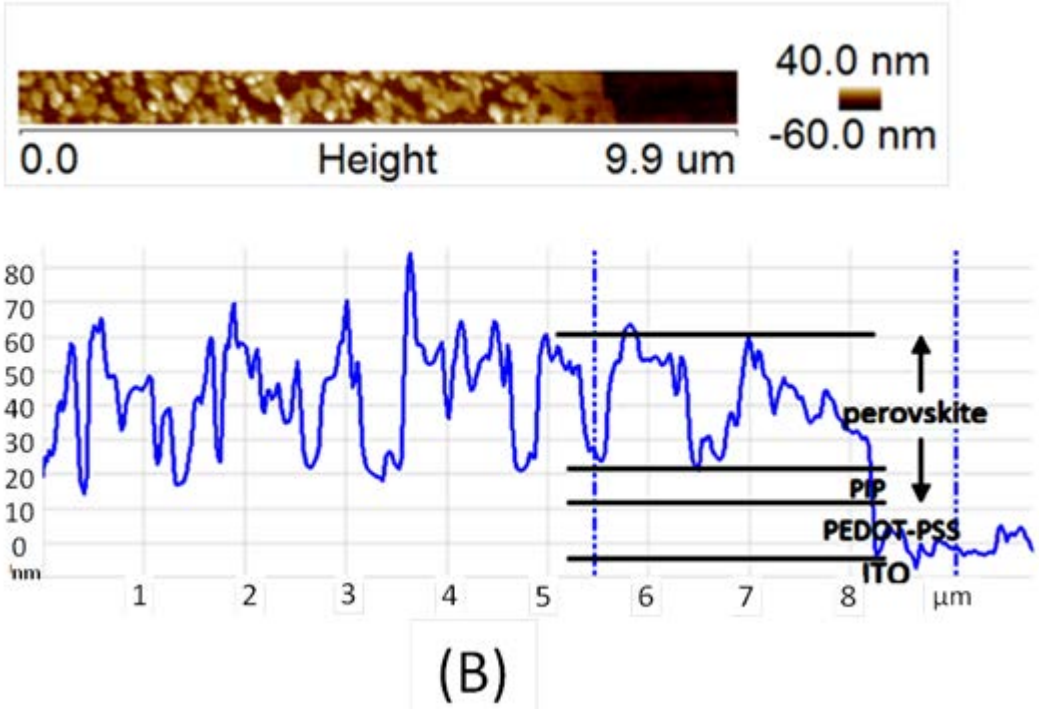
40.0 nm
-60.0 nm
0.0
Height
9.9 um
80
70
60
50
40
30
20
10
0
nm
perovskite
PIP
PEDOT-PSS
ITO
1
2
3
4
5
6
7
8
µm

(B)

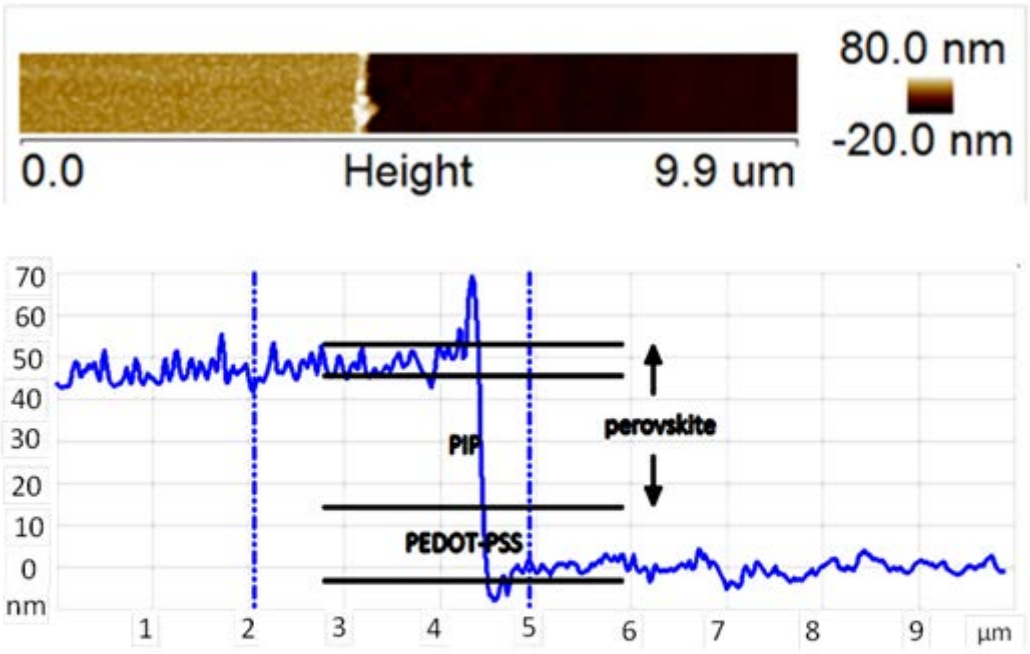
80.0 nm
-20.0 nm
0.0
Height
9.9 um
70
60
50
40
30
20
10
0
nm
perovskite
PIP
PEDOT-PSS
1
2
3
4
5
6
7
8
9
µm

(C)

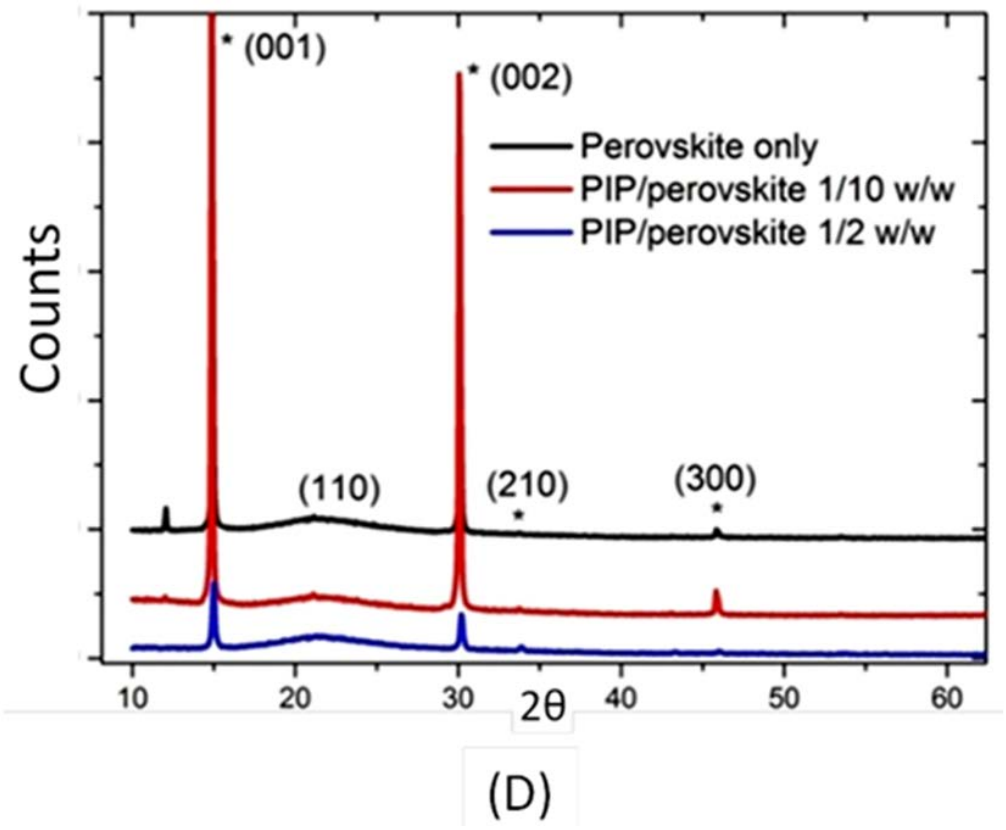

Figure 5.2 AFM images: (A) Scratched edge of PEDOT-PSS film on ITO substrate and its cross-section profile. (B) Scratched PIP: perovskite/PEDOT:PSS film of mixing ratio 1/10 w/w and its cross-section profile. (C) Scratched PIP: perovskite/PEDOT-PSS film of mixing ratio 1/2 w/w and its cross-section profile. The estimated average thickness of PEDOT: PSS film is 18±2 nm, the estimated thickness of PIP is 7±2 nm in PIP/perovskite 1/10 w/w film and 30±3 nm in PIP/perovskite 1/2 w/w film. (D) X-ray diffraction data of films spin-coated on quartz substrate under different PIP/perovskite blending ratios. The sizes of perovskite-only and PIP/perovskite 1/10 w/w films cannot be determined because of instrumental broadening. The estimated crystal size for PIP/perovskite 1/2 w/w is 70 nm.

5.4 LED device fabrication

Our devices use the poly(9,9-dioctylfluorene) (F8) as an electron-transporting layer, which blocks injected holes from leaving the device, and also serves as a spacer layer to prevent luminescence quenching at the metal electrode. In addition, the semiconducting F8 forms a good conformal coating and prevents the top electrode from shorting through the thin (< 50 nm) perovskite layer. The low-workfunction calcium electrode provides ohmic electron injection, while the high-workfunction PEDOT:PSS acts as the hole-injection layer.

The structure of our devices is ITO/PEDOT: PSS/Perovskite:PIP/F8/Ca/Ag, as shown in Figure 5.3 (A). We use a large-bandgap perovskite, $CH_3NH_3PbBr_3$, as a green emitter layer. The perovskite precursors are made by blending CH_3NH_3Br and $PbBr_2$ at 5 wt% (DMF) at a molar ratio of 3:2. A commercial aromatic polyimide precursor (PIP) dissolved in N-methyl-2-pyrrolidone (NMP) is blended with perovskite precursor solutions in different weight ratios. The chemical structure of PIP is shown in Figure 5.3 (B). This polymer was chosen because it can associate well with the hybrid perovskite and can be readily processed in DMF, possibly due to its polar functional group and hydrophilicity [16]. The polymer is also transparent and electrically insulating, and therefore suitable for use as a charge-blocking material in a light-emitting device. The use of a polymer in the composite layer also potentially offers the benefit of enhanced material stability, as previously demonstrated in 2D-perovskite-polymer mixtures [17], [18]. The perovskite nanocrystal: PIP polymer composite forms upon spin-coating the blend solutions on PEDOT: PSS and annealing the resulting films at 60 °C for 1 minute. We note that the PIP polymer remains in its un-imidized precursor form under our processing conditions, since a temperature of 200 °C is typically required for the precursor to react into polyimide [19]. The formation of perovskite crystals, in the presence of a polymer matrix, is confirmed by x-ray diffraction studies (Figure 5.2(D)).

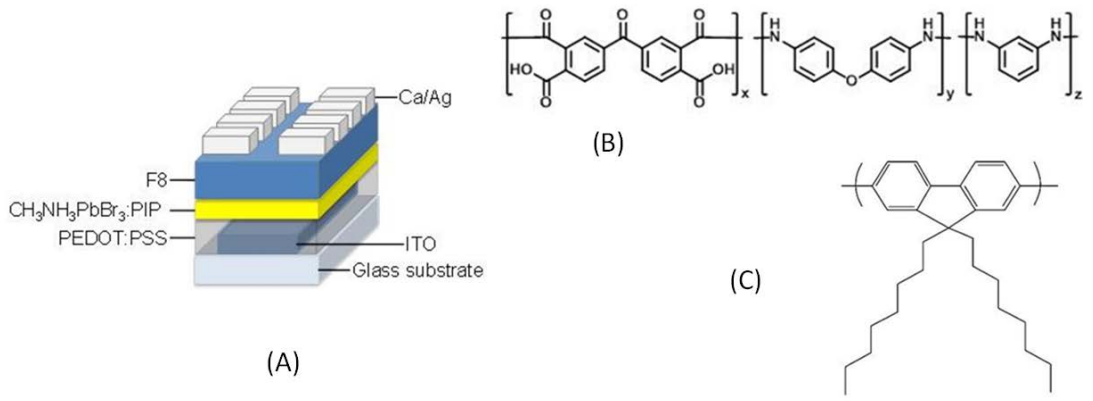

Figure 5.3 (A) Device structure of $CH_3NH_3PbBr_3$ perovskite light-emitting diode (PeLED) (B) Chemical structure of PI2525 polyimide precursor (PIP) (C) Chemical structure of poly(9,9-dioctylfluorene) (F8)

Detailed fabrication steps:

F8 polymer was provided by Cambridge Display Technology (CDT) and was used as received. Polyimide precursor (product number PI2525) was purchased from HD microsystems and was diluted into a concentration of 20 mg ml^{-1} in N-methyl-2-pyrrolidone before use. All other chemicals were purchased from Sigma-Aldrich and were used as received.

Blend solutions were prepared by mixing 5 wt% $CH_3NH_3PbBr_3$ solutions and diluted PIP solutions to give different weight ratios. The blend solutions were stirred at room temperature for 2 hours before use. The mixed solutions ranged from colourless to light-orange coloured depending on the blending ratio. ITO-coated glass substrates were cleaned with acetone and isopropanol for 15 minutes separately, followed by 10 minutes oxygen plasma treatment. PEDOT:PSS (Clevios P VP Al 4083) was spin coated on ITO substrates at 6000 rpm for 30 seconds and annealed at 140 °C for 30 minutes in a nitrogen glovebox. The blend solutions were spin-coated onto PEDOT:PSS at 3000 rpm for 30 seconds and annealed at 60 °C for 1 minute. A solution of F8 in chlorobenzene (10 mg mL^{-1}) was spin coated on top of the PIP: perovskite layer at 3000 rpm for 30 seconds to give a 50 nm film. We note that PIP is insoluble in chlorobenzene and is unaffected by the deposition of the F8 layer. Ca (20 nm) and Ag (100 nm) were successively deposited by vacuum thermal evaporation at

vacuum better than 3×10^{-6} mbar. Devices were tested in air immediately after taking out of glovebox without additional encapsulation.

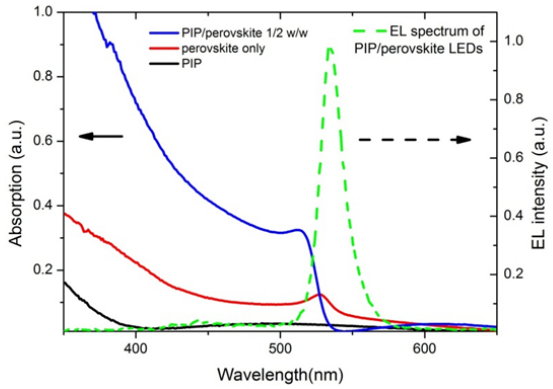

(A)

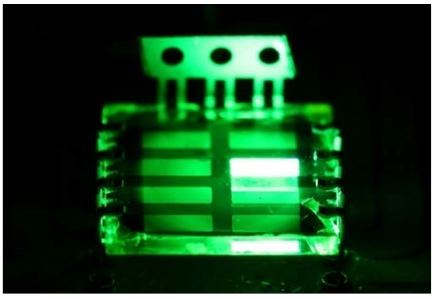

(B)

Figure 5.4 (A) Absorption spectra of PIP, $CH_3NH_3PbBr_3$ and blend film, and electroluminescence spectrum (dashed line) of $CH_3NH_3PbBr_3$/PIP PeLED. (B) Image of $CH_3NH_3PbBr_3$/PIP PeLED.

5.5 LED Performance and Discussion

We tested the performance of the above composite films in a light-emitting diode structure. Figure 5.4 (A) shows the absorption spectrum of the perovskite/PIP film and its electroluminescence in a device structure. The PeLEDs display a strong green electroluminescence at 534 nm with a narrow full-width at half-maximum of 19 nm. There is negligible absorption of the green perovskite emission by the PIP polymer. As shown in Figure 5.4 (B), electroluminescence from a representative device is uniform across the entire device pixel with no sign of large-scale inhomogeneity, demonstrating that the emission from perovskite nanocrystals is uniformly distributed across the spin-coated film.

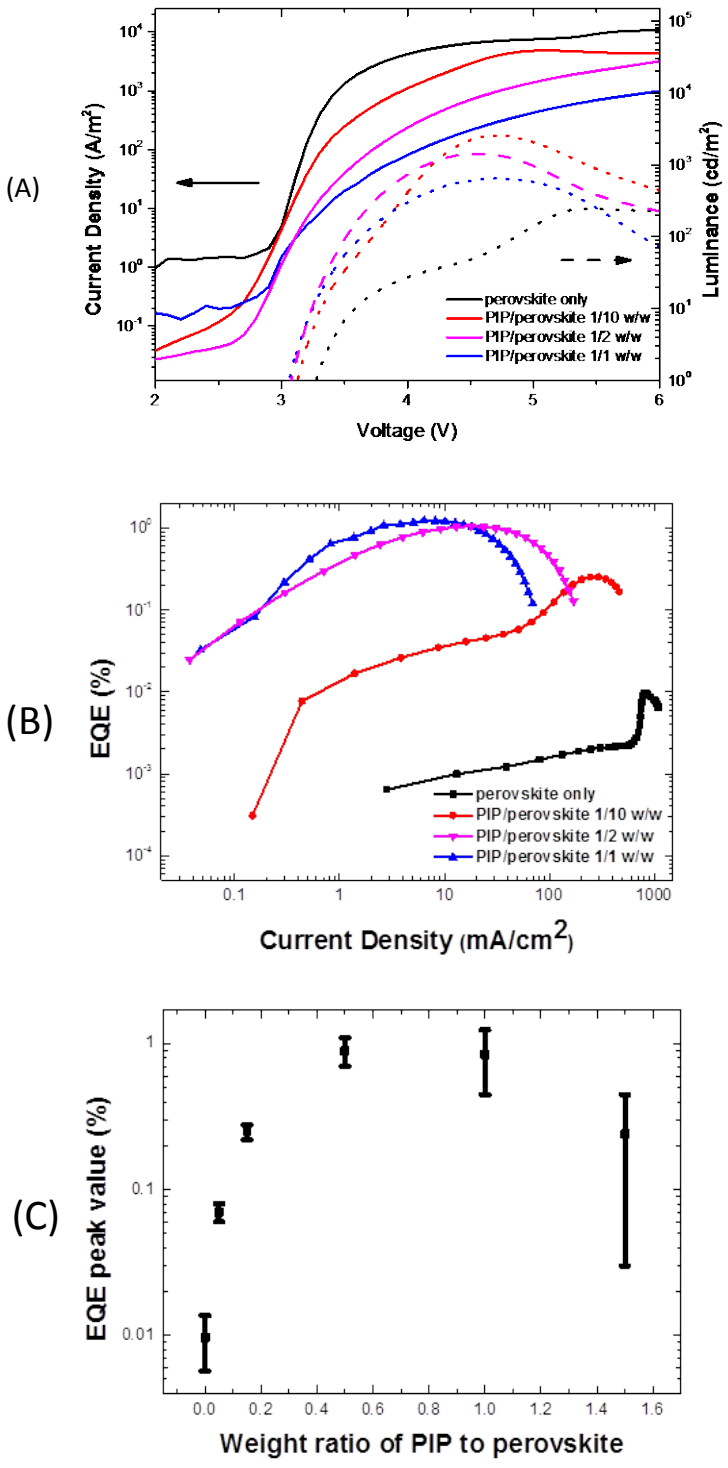

Figure 5.5 (A) Current density (solid line) vs. voltage and luminance (dashed line) vs. voltage characteristics of PeLEDs. (B) External quantum efficiency vs. current density characteristics of PeLEDs. (C) External quantum efficiency peak value vs. $CH_3NH_3PbBr_3$/PIP weight ratio (the error bar are statistics from 10-20 devices at each weight ratio point).

Figure 5.5(A) shows the luminance and current density versus voltage characteristics of devices with PIP: perovskite weight ratios of 1:10, 1:2 and 1:1 as well as a control device with only perovskite in the emissive layer (no PIP added). Through the increase in the blending ratio of PIP, the current density is reduced at each driving voltage and the luminance is enhanced, thereby leading to a dramatic enhancement in device efficiency. For instance, in the 1:2 ratio device, a current density of 31 mA cm^{-2} is required to produce a luminance of 200 cd m^{-2}, but much larger current densities of 5800 mA cm^{-2} and 570 mA cm^{-2} are required for the perovskite-only and the 1:10 ratio devices respectively to achieve the same luminance. Figure 5.5(B) shows the corresponding external quantum efficiency (EQE) of the respective devices. With the addition of PIP, the devices show a clear increase in quantum efficiency. In particular, the EQE increased by more than 2 orders of magnitude, from 0.01% in devices without PIP, to 1.2% in devices with a 1:1 PIP to perovskite ratio.

We further investigated the PIP: perovskite composite LEDs over a wider range of mixing ratios and plotted their device performance in Figure 5.5 (C). The best peak EQE of ~1% is achieved between a 1:2 and 1:1 PIP to perovskite ratio. This represents a 10-fold enhancement of device efficiency over the previous report [11, 12]. At higher ratios, the device efficiency drops and the variance in device performance increases. Some devices that contained large polymer fractions were too resistive and failed to work. We show in Figure 5.6 that PIP-only devices were completely insulating.

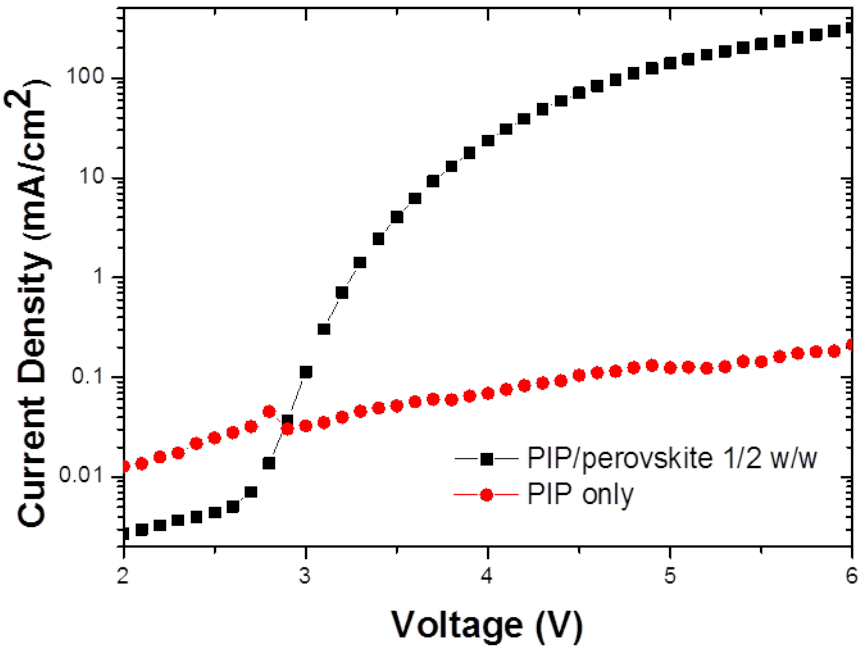

Figure 5.6 Comparison of current density vs. voltage characteristics of PIP: perovskite 1/2 w/w and PIP-only devices.

These device studies and the SEM characterisations suggest that the 1:2 ratio film provides optimal PIP coverage and effectively blocks pinholes or electrical shunting paths. This leads to low current losses and significantly enhanced device efficiency. The polymer coverage in the 1:10 ratio films is thinner and possibly incomplete in some areas, and therefore provides less protection against current losses. Since the perovskite and PIP composite devices emit efficiently and uniformly up to a 1:1 blend ratio, it is reasonable to assume that the perovskite nanocrystals extend across the thickness of these films, forming electrical contact with both the PEDOT: PSS and the F8 layers.

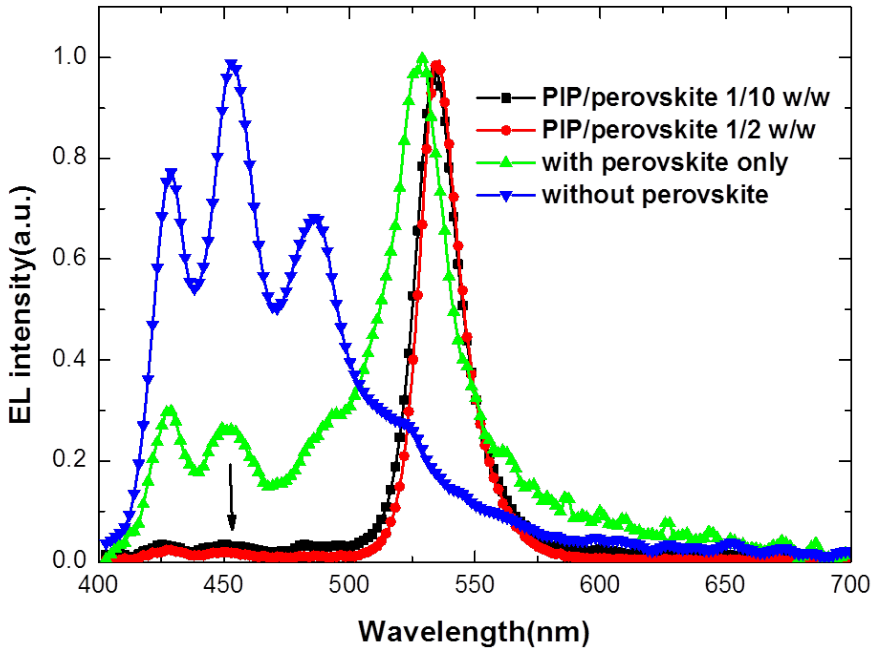

Figure 5.7 EL spectra of F8 LED, perovskite-only and PIP/perovskite blend LEDs. All spectra were taken at 5 V bias.

We further investigated the effects of PIP addition on the electroluminescence spectra of the PeLEDs. As shown in Figure 5.7, an F8 contribution to electroluminescence could be observed between 400 nm and 500 nm for the perovskite-only devices (no PIP). This F8 emission most likely arises from hole injection directly from PEDOT: PSS into the F8. In contrast, F8 electroluminescence was effectively shut off in the PIP: perovskite PeLEDs and clean perovskite emission was obtained, consistent with suppression of hole injection into the F8. Combined with the improvement in efficiency, this demonstrates that the PIP is remarkably effective in preventing contact between F8 and PEDOT: PSS.

5. 6 Conclusion

In this chapter we have shown unambiguously that luminescent perovskite nanocrystals can be embedded in a pinhole-free matrix of dielectric polymer to give superior light-emitting diode performance. This technique is completely solution processed and remarkably simple, and could potentially be extended to perovskite

solar cells to deal with current leakage problems. This incorporation of a polymer matrix further gives the device an added advantage of flexibility for an otherwise brittle perovskite material.

It is certainly interesting and perhaps surprising that a crystalline perovskite material can form and associate so well with a polymeric mixture without the need for any complex surface modification, and still retain its remarkable optoelectronic properties. This is possibly granted by the unique inorganic-organic hybrid nature of the organometal halide perovskites. We expect this extraordinary compatibility of perovskites with organic materials, coupled with their respectable light-emitting and optoelectronic performance to make them valuable for a range of flexible displays and lighting applications.

We expect the performance will be enhanced by further device engineering, The structure employed in this chapter is yet to be fully optimized[20]. For example, PEDOT is not a good electron blocker, to improve the hole-injection and electron blocking an intermediate layer is always used in highly efficient quantum dot light emitting diodes [21].

We note that after the publication of this work, follow-up works in different directions were reported. Wong et al. grew $CH_3NH_3PbX_3$ arrays directly on substrate, and demonstrated LED devices [22]. Ying et al. synthesized colloidal perovskite nanoplatelets, and fabricate bright light emitting diode with spin-coated PVK:PBD layer as a blocking layer [23]. Li et al. fabricated a single-layer perovskite LED with perovskite/poly(ethylene oxide), with no need of polymer charge-transport layers [24]. Masi et al. systematically studied the composite morphology of perovskite with wider range of polymers such as poly(methyl methacrylate) (PMMA), polystyrene, and poly[2-methoxy-5-(2-ethylhexyloxy)-1,4-phenylenevinylene (MEH-PPV) composites [25].

References

1. Li, G., Tan, Z.-K., Di, D., Lai, M.L., Jiang, L., Lim, J.H.-W., Friend, R.H., and Greenham, N.C., *Efficient Light-Emitting Diodes Based on Nanocrystalline Perovskite in a Dielectric Polymer Matrix.* Nano letters, **15**, 2640-2644(2015).
2. Burroughes, J.H., Bradley, D.D.C., Brown, A.R., Marks, R.N., Mackay, K., Friend, R.H., Burns, P.L., and Holmes, A.B., *Light-emitting diodes based on conjugated polymers.* Nature, **347**, 539-541(1990).
3. Greenham, N.C., Moratti, S.C., Bradley, D.D.C., Friend, R.H., and Holmes, A.B., *Efficient light-emitting diodes based on polymers with high electron affinities.* Nature, **365**, 628-630(1993).
4. Colvin, V.L., Schlamp, M.C., and Alivisatos, A.P., *Light-emitting diodes made from cadmium selenide nanocrystals and a semiconducting polymer.* Nature, **370**, 354-357(1994).
5. Coe, S., Woo, W.-K., Bawendi, M., and Bulovic, V., *Electroluminescence from single monolayers of nanocrystals in molecular organic devices.* Nature, **420**, 800-803(2002).
6. Lee, M.M., Teuscher, J., Miyasaka, T., Murakami, T.N., and Snaith, H.J., *Efficient Hybrid Solar Cells Based on Meso-Superstructured Organometal Halide Perovskites.* Science, **338**, 643-647(2012).
7. Burschka, J., Pellet, N., Moon, S.-J., Humphry-Baker, R., Gao, P., Nazeeruddin, M.K., and Gratzel, M., *Sequential deposition as a route to high-performance perovskite-sensitized solar cells.* Nature, **499**, 316-319(2013).
8. Liu, M., Johnston, M.B., and Snaith, H.J., *Efficient planar heterojunction perovskite solar cells by vapour deposition.* Nature, **501**, 395-398(2013).
9. Stranks, S.D., Eperon, G.E., Grancini, G., Menelaou, C., Alcocer, M.J.P., Leijtens, T., Herz, L.M., Petrozza, A., and Snaith, H.J., *Electron-Hole Diffusion Lengths Exceeding 1 Micrometer in an Organometal Trihalide Perovskite Absorber.* Science, **342**, 341-344(2013).
10. Ball, J.M., Lee, M.M., Hey, A., and Snaith, H.J., *Low-temperature processed meso-superstructured to thin-film perovskite solar cells.* Energy & Environmental Science, **6**, 1739-1743(2013).

11. Schmidt, L.C., Pertegás, A., González-Carrero, S., Malinkiewicz, O., Agouram, S., Mínguez Espallargas, G., Bolink, H.J., Galian, R.E., and Pérez-Prieto, J., *Nontemplate Synthesis of CH3NH3PbBr3 Perovskite Nanoparticles.* Journal of the American Chemical Society, **136**, 850-853(2014).
12. Tan, Z.-K., Moghaddam, R.S., Lai, M.L., Docampo, P., Higler, R., Deschler, F., Price, M., Sadhanala, A., Pazos, L.M., Credgington, D., Hanusch, F., Bein, T., Snaith, H.J., and Friend, R.H., *Bright light-emitting diodes based on organometal halide perovskite.* Nat Nano, **9**, 687-692(2014).
13. Kim, Y.H., Cho, H., Heo, J.H., Kim, T.S., Myoung, N., Lee, C.L., Im, S.H., and Lee, T.W., *Multicolored Organic/Inorganic Hybrid Perovskite Light-Emitting Diodes.* Advanced Materials, **27**, 1248-1254(2015).
14. Chen, Q., Zhou, H., Hong, Z., Luo, S., Duan, H.-S., Wang, H.-H., Liu, Y., Li, G., and Yang, Y., *Planar Heterojunction Perovskite Solar Cells via Vapor-Assisted Solution Process.* Journal of the American Chemical Society, **136**, 622-625(2013).
15. Dowland, S., Lutz, T., Ward, A., King, S.P., Sudlow, A., Hill, M.S., Molloy, K.C., and Haque, S.A., *Direct Growth of Metal Sulfide Nanoparticle Networks in Solid-State Polymer Films for Hybrid Inorganic–Organic Solar Cells.* Advanced Materials, **23**, 2739-2744(2011).
16. Salim, T., Sun, S., Abe, Y., Krishna, A., Grimsdale, A.C., and Lam, Y.M., *Perovskite-based solar cells: impact of morphology and device architecture on device performance.* Journal of Materials Chemistry A, **3**, 8943-8969(2015).
17. Kitazawa, N., *Preparation and optical properties of nanocrystalline (C6H5C2H4NH3) 2PbI4-doped PMMA films.* Journal of materials science, **33**, 1441-1444(1998).
18. Wei, Y., Lauret, J., Galmiche, L., Audebert, P., and Deleporte, E., *Strong exciton-photon coupling in microcavities containing new fluorophenethylamine based perovskite compounds.* Optics Express, **20**, 10399-10405(2012).
19. Minges, M.L., *Electronic materials handbook: packaging*. Vol. 1: Asm International(1989)
20. Tan, Z.-K., Moghaddam, R.S., Lai, M.L., Docampo, P., Higler, R., Deschler, F., Price, M., Sadhanala, A., Pazos, L.M., Credgington, D., Hanusch, F., Bein,

T., Snaith, H.J., and Friend, R.H., *Bright light-emitting diodes based on organometal halide perovskite.* Nature nanotechnology, 2014).

21. Dai, X., Zhang, Z., Jin, Y., Niu, Y., Cao, H., Liang, X., Chen, L., Wang, J., and Peng, X., *Solution-processed, high-performance light-emitting diodes based on quantum dots.* Nature, **515**, 96-99(2014).
22. Wong, A.B., Lai, M., Eaton, S.W., Yu, Y., Lin, E., Dou, L., Fu, A., and Yang, P., *Growth and Anion Exchange Conversion of CH3NH3PbX3 Nanorod Arrays for Light-Emitting Diodes.* Nano letters, **15**, 5519-5524(2015).
23. Ling, Y., Yuan, Z., Tian, Y., Wang, X., Wang, J.C., Xin, Y., Hanson, K., Ma, B., and Gao, H., *Bright Light-Emitting Diodes Based on Organometal Halide Perovskite Nanoplatelets.* Advanced Materials, 2015).
24. Li, J., Bade, S.G.R., Shan, X., and Yu, Z., *Single-Layer Light-Emitting Diodes Using Organometal Halide Perovskite/Poly (ethylene oxide) Composite Thin Films.* Advanced Materials, **27**, 5196-5202(2015).
25. Masi, S., Rizzo, A., Aiello, F., Balzano, F., Uccello-Barretta, G., Listorti, A., Gigli, G., and Colella, S., *Multiscale morphology design of hybrid halide perovskites through a polymeric template.* Nanoscale, **7**, 18956-18963(2015).

Chapter 6

Quantum Confined Photoluminescence Characteristics in Organometal Halide Perovskite

The first efficient organolmetal halide perovskite solar cells were based on perovskite nanocrystals synthesised by spin-coating onto an Al_2O_3 [1] or TiO_2 [2] scaffold. Now that light-emitting applications are of interest, it is important to fully understand the optical properties of the nanocrystals. Following the progress reported in Chapter 5, where perovskite nanocrystals are formed in-situ in a polymer matrix; in this chapter we are interested in fabricating perovskite nanocrystals through a one-step synthesis by spin-coating from a perovskite precursor/alumina nano-particle blend solution. In the composite films formed, we achieved improved PLQE and environmental stability. Structural studies show that sub-10 nm perovskite crystals are formed within a dense alumina matrix. Spectroscopic studies show that the composite films have 25 % PLQE at high excitation power density, and have longer life time than the perovskite-only film.

6.1 Introduction

In Chapter 5, we introduced methods to form perovskite nanocrystals in an insulating polymer matrix, and achieved two orders of magnitude improvement on EQE performance in PeLED. In the SEM images in chapter 5, the polymer/perovskite composite was a mixture of domains with different degrees of crystallinity, thus the overall PLQE of the composite was found to be worse than that of pure perovskite films. Also, the size of the nanocrystal domains is tens of nanometres, much bigger

than the Bohr radius of excitons in perovskite (~5 nm) [3], such that quantum confinement effects are not expected.

In this chapter, we substitute the PIP polymer matrix with an alumina matrix fabricated from alumina nanoparticles. This hard matrix enables better crystallization of perovskite during deposition, and the films show higher photoluminescence efficiency than pure perovskite or polymer/perovskite composite film.

6.2 Material and film preparation

The alumina-nanoparticle dispersion (20 wt. % in isopropanol), milky and viscous, was ordered from Sigma Aldrich. The provider reported that the size of the alumina nanoparticles is less than 50 nm (measured by dynamic light scattering).

$CH_3NH_3PbBr_3$ precursor solution was prepared by mixing 3:1 molar ratio CH_3NH_3Br:$PbBr_2$ at a starting concentration of 5% w/w in DMF. The $CH_3NH_3PbBr_3$ precursor solution was then mixed with alumina nanoparticle dispersion at different ratios to reach different weight ratios of perovskite precursor to alumina. The mixture solutions were then spin-coated onto the spectrosil substrates, and these freshly-prepared samples were characterized within 24 hours. All the photoluminescence (PL), photoluminescence quantum efficiency (PLQE) and time-correlated single photon counting (TCSPC) characterizations were done in air. The PLQE at 1000 mW/cm^2 was measured using the integrating-sphere method as introduced in Chapter 3. For the rest of PLQE measurement, the samples were photo-excited by a 405 nm laser while the laser's power density was controlled by a filter wheel and monitored by an optical power metre. The PL intensities were first measured directly (without integrating sphere) using a focus lens and a spectrometre. These PL intensities were then converted to PLQE by calibration using the PLQE value at 1000 mW/cm^2.

6.3 Results

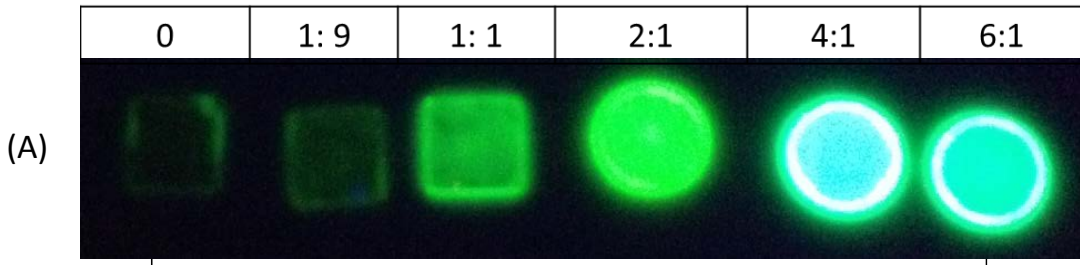

(A)

(B)

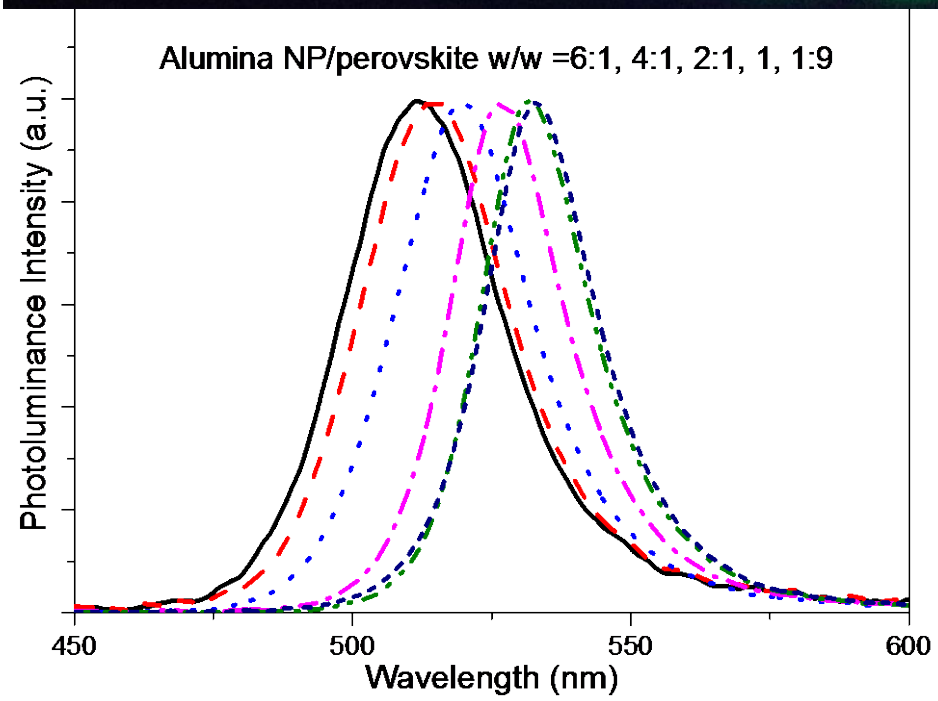

(C)

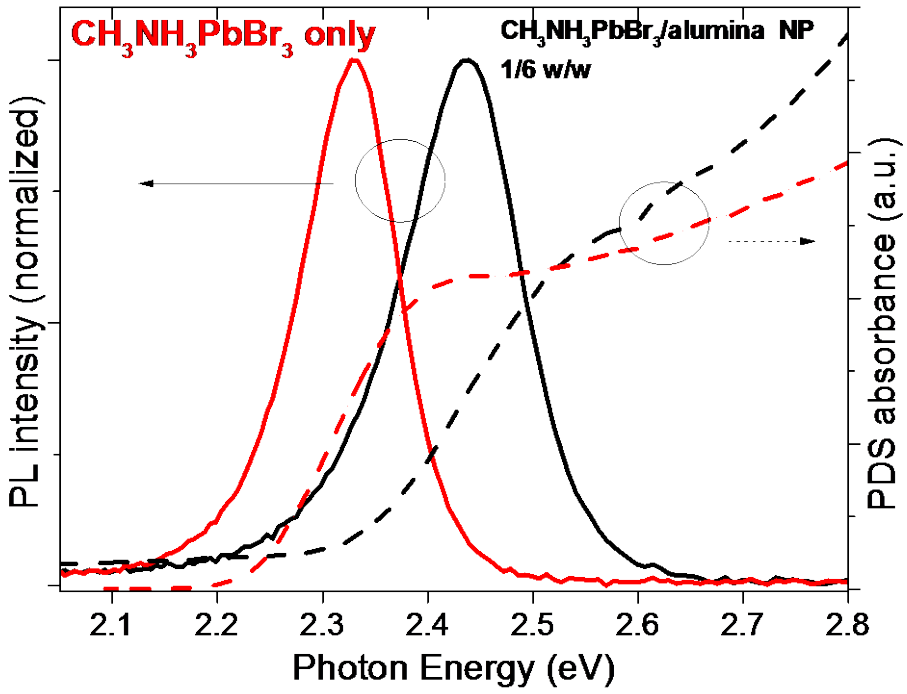

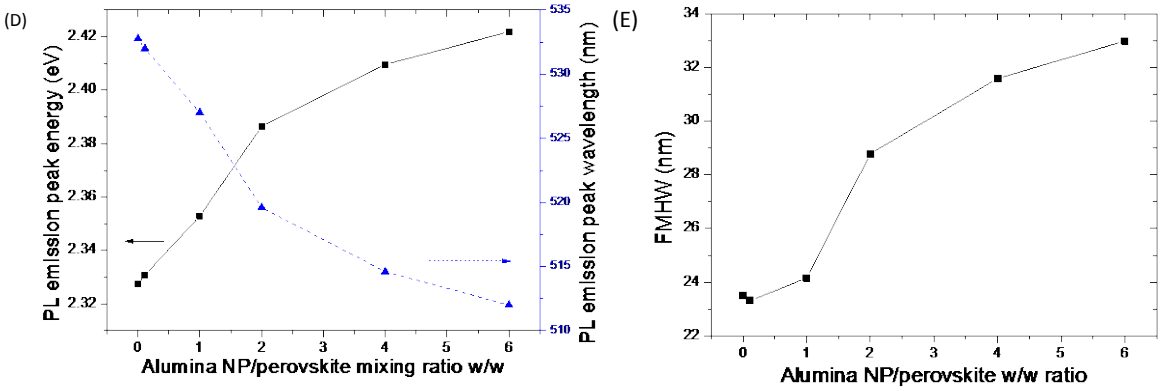

Figure 6.1 (A) Image of the photoluminescence of alumina/perovskite films at different blending ratios. (B) Combined PDS absorption spectra with PL emission spectra of perovskite-only film and perovskite/alumina 1/6 composite film. (C) Photoluminescence spectra of Alumina/perovskite composite films at different ratios. (D) Emission wavelength and energy as a function of blending ratio. (E) FWHM of the PL spectra as a function of blending ratio.

Figure 6.1(A) shows a photograph of the PL of a series of spin-coated films under the same 365 nm UV illumination. Films with zero or low alumina content showed less luminescence. This could not be accounted to the difference in their absorption; so here it is clear that the PLQE increases with alumina content. It is also clear that there is a blue-shift in the emission spectrum as the alumina content is increased from 1:1 to 6:1. The stability of the PL is also improved with alumina loading; the pure perovskite films were found to lose their luminescence in a few hours at dark, but above an alumina/perovskite-blending ratio of 1:1, the composite films are stable for months.

Figure 6.1(B) shows the PL spectra of the films. The PL-peak wavelength is found to decrease as the blending ratio of alumina increases, consistent with the qualitative observations. The PL-peak wavelength shifts from 533 nm to 513 nm, as the blending ratio increase from zero to 6:1, as shown in Figure 2(D). Another interesting observation is the change of the bandwidth of the PL spectra in the composite films (Figure 6.1(D)). The perovskite-only and 1:9 alumina/perovskite composite films have a sharp PL emission peak of ～23 nm FWHM; the peak was broadened to ～33 nm FWHM in the 6:1 alumina/perovskite composite film.

Absorptions of the films were measured by photothermal deflection spectroscopy (PDS). PDS is a sensible technique independent of sample scattering [4]. The resultant absorption curves together with the PL emission spectra were plotted in the inset of Figure 6.1(B). The PL and absorption spectra shift together to the blue as the alumina content increases. As alumina neither absorbs nor emits light in the measured wavelength range, this shift must be due to the intrinsic band-edge shift of the perovskite. Figure 6.1(D) shows the band-edge shift of perovskite material is tuneable from 2.3 eV to 2.4 eV and thus by ~100 meV.

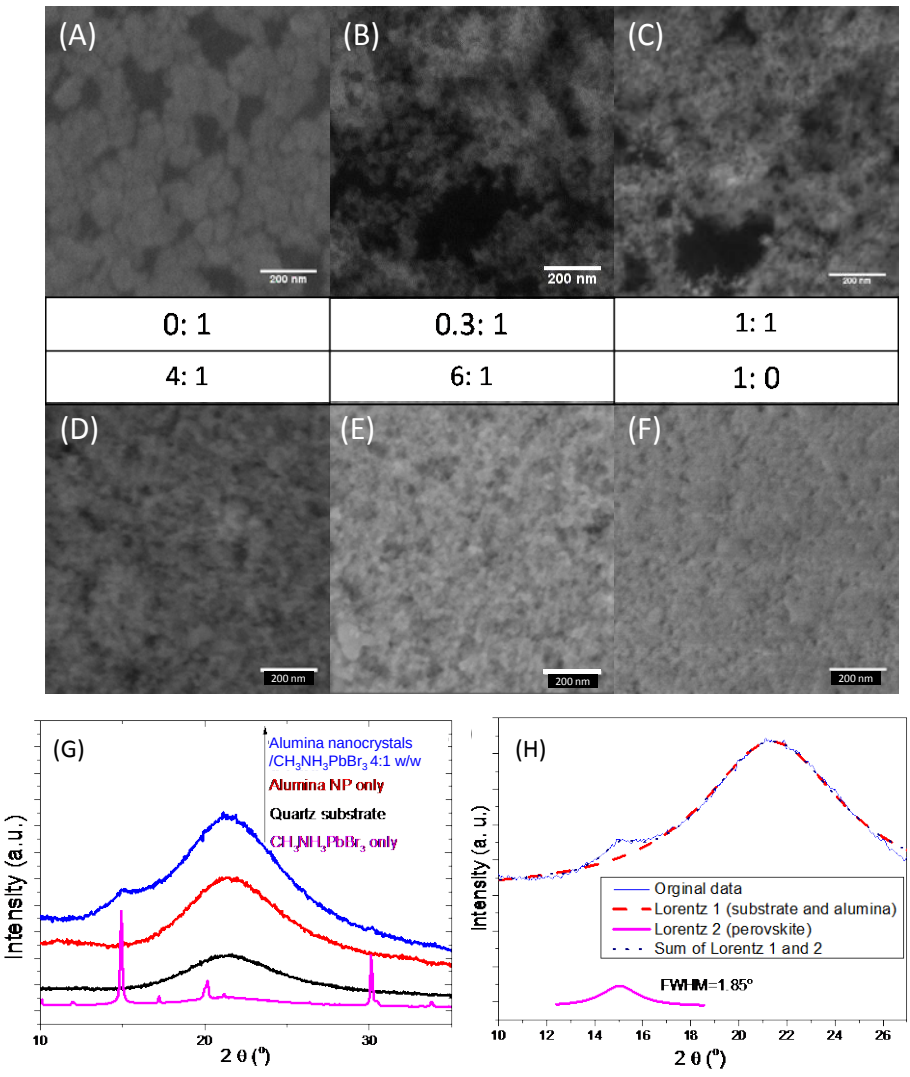

Figure 6.2 (A-F) Top-view SEM images of aluminium/perovskite nanoparticle films. These films were prepared on conductive Glass/ITO/PEDOT-PSS substrate to avoid charging issue. Note: the numbers between the images indicate weight ratio of alumina nanoparticle versus perovskite precursor in the starting solutions. (G) XRD spectra of the substrate, and of $CH_3NH_3PbBr_3$ only, alumina nanoparticle and 4:1 alumina/perovskite composite films. (H) Fitted peaks of the XRD spectrum for the 4:1 alumina/perovskite composite film.

The morphologies of our films were characterized by scanning electron microscopy (SEM), as shown in Figure 6.2. The perovskite-only film (Figure 6.2(A)) comprised of ～100 nm grains; this morphology with poor coverage and grain formation is as expected, as the quick crystallization of spin-coated perovskite is well known to cause rough film morphology[5]. When 30% w/w alumina nanoparticles were blended to the perovskite solution, these grains disappeared (Figure 6.2 (B)). Instead, we observed patches of rough aggregates composed of ～10-20 nm nanocrystals. These crystals are likely to be alumina nanoparticles as their sizes are consistent with the provider's report. No perovskite grains were observed, indicating perovskite was mixed with alumina nanocrystals into a fine composite. The good association between alumina and perovskite is also consistent with a previous report mentioning perovskite is more compatible with polar and hydrophilic surfaces than other types of surfaces [6]. We observed slight brightness contrast between different regions which probably shows different degrees of alumina/perovskite aggregations. As the blending ratio of alumina/perovskite increased to above 1:1, the composite films started to uniformly and fully cover the substrates with no obvious sign of spatial inhomogeneity, as shown by the SEM images in Figure 6.5 (C-E). SEM image of the alumina-only film is shown in Figure 6.5 (F), the alumina nanoparticles were densely packed in, without any distinguishable nano-pores at the resolution of our SEM.

To further study the structures in the composite films, we carried out XRD measurements on a composite film (4:1 alumina/perovskite w/w) as well as the control samples, as shown in Figure 6.2 (G). The XRD spectra of both the perovskite-only and the composite films have characteristic peaks at 14.9^{o} and 30.1^{o}, confirming formation of the perovskite crystal structure. The perovskite peaks in the composite film are broadened compared with that in the perovskite-only film, indicating existence of small-size crystals. By fitting these peaks with Lorentz functions as shown in Figure 6.2 (H), the FWHM of the peak at $2\theta = 14.9^{o}$ is calculated to be 1.85^{o}. Allowing for the instrumental broadening FWHM 0.16^{o} as determined from the standard sample and applying the corrected peak broadening in a Scherrer Equation, we estimated the average sizes of perovskite crystals to be 5.4 nm.

Combining the characterizations by SEM and XRD, it is clear the perovskite/alumina composite films are composed of a densely-packed alumina nanoparticle matrix containing perovskite nanocrystals. The sizes of the perovskite crystals were tuned from ~100 nm to ~5 nm, corresponding to PL emission peaks ranging from 533 nm to 513 nm.

To verify whether the PL shift is from quantum confinement from these ~5 nm nanocrystals, we applied a model developed by Brus based on 'effective mass approximation', in this approximation, an exciton is considered to be confined to a spherical volume of the crystallite[7]:

$$E_g(NC) = E_g(bulk) + \frac{\pi^2\hbar^2}{2\mu a^2} + E(binding),$$

where $E_g(NC)$ is the band-edge exciton energy of the nanocrystals, $E_g(bulk)$ is the band-edge exciton energy of the bulk material, $\frac{\pi^2\hbar^2}{2\mu a^2}$ is the confinement energy. $E(binding)$ is the exciton binding energy. $\hbar = 1.054 \times 10^{-34} J\ s$, is reduced Planck's constant, m_r is the reduced effective mass and a is the radius of the nanocrystal. In our case, $m_r = 0.13\, m_0$ [3], and $a = 2.7$ nm . We acquired the confinement energy $\frac{\pi^2\hbar^2}{2\mu a^2}$ to be 0.40 eV. Binding energy in bulk $CH_3NH_3PbBr_3$ was reported to be -0.084 eV, while the binding energy in 4 nm radius $CH_3NH_3PbBr_3$ quantum dots was reported to be -0.32 eV [8]. The magnitude resulted from the theoretical prediction (tens to hundreds meV) qualitatively fits our experimental result (~0.1 eV). The derivation from our experimental results may be because the sizes of our perovskite nanocrystals are not well defined. We noticed that the energy shift of PL in our samples (0.09 eV) than ref [8] (0.01 eV) which may cause error in our calculation.

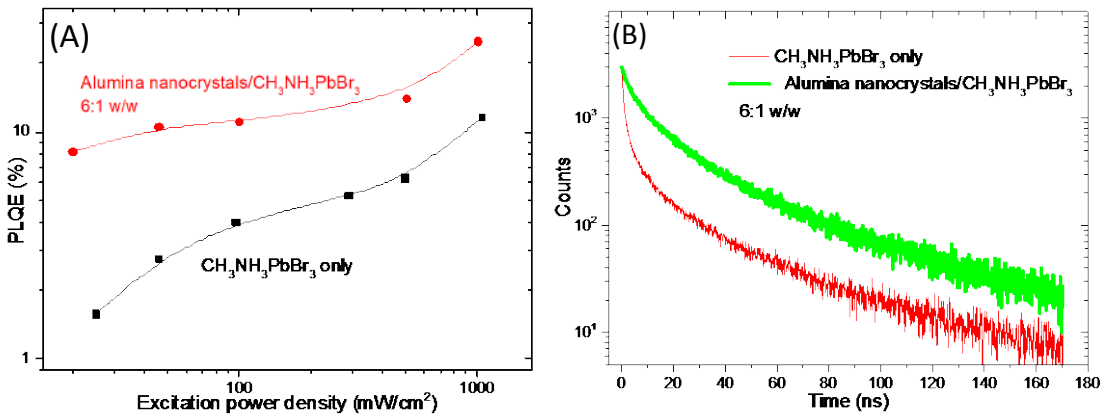

Figure 6.3 (A) PLQE of the perovskite-only film and the alumina/perovskite composite film versus excitation power density. (B) PL decay curves of the perovskite-only film and the alumina/perovskite composite film

To further explore the photoluminescence in the composite films, we measured PLQE as a function of photo-excitation power density and plotted the curves for both the perovskite-only and the composite films in Figure 6.3 (A).

As reported by Deschler et al. [9], in bulk perovskite $CsPbI_{3-x}Cl_x$, the recombination at low excitation power density is monomolecular (trap-assisted charge recombination), and at higher excitation power density it is bimolecular (free-carrier recombination). In our experiment, the PLQE of $CH_3NH_3PbBr_3$-only film increased slowly between 30 and 500 mW/cm^2, but it increased more steeply above 500 mW/cm^2. The former may be related to a significant monomolecular trap-assisted recombination[10]; the latter may be related to more contribution from biomolecular recombination.

Comparing to the PLQE of the perovskite-only film, the PLQE of the composite film is higher (8.2% at 30 mW/cm^2 and 25% at 1000 mW/cm^2) compared to that in perovskite-only film (1.6% at 30 mW/cm^2 and 11% at 1000 mW/cm^2). This is consistent with efficient recombination between electrons and holes confined in individual nanocrystals [11, 12], giving essentially monomolecular dynamics.

Since the measurement is carried out by tuning laser power from high excitation intensity to low excitation intensity, the exposure of the samples to high laser power cause degradation of the sample, which may explain the sharp increase just before 1000 mW/cm^2.

The PL lifetime was acquired by TCSPC. As shown in Figure 6.3 (B), PL lifetime was 1.2 ns in the perovskite-only film, and was 9.7 ns in the composite film.

We estimated the excitation per quantum dot in the first layer of the composite film at continuous excitation power density of 1000 mW/cm^2, using the absorbance of the perovskite film (for a ~50 nm perovskite film, absorbance is ~0.15 at 405 nm). The laser was able to excite 10000 excitons per second per quantum dot. Considering lifetime of each exciton was less than 100 ns, the average steady-state excitons per quantum dot was less than 0.01 exciton per dot, such that multiple-exciton processes are unlikely.

We made some efforts to employ this alumina/perovskite composite in a LED structure. At low alumina blending ratio (Figure 6.2 (B)), the LED shorted at very low bias, indicating the morphology of these films is rough, causing leakage pathways. At high blending ratios (Figure 6.2 (C-E)) the device was insulating, indicating that the perovskite quantum dots in the alumina matrix were not well connected vertically.

6.5 Conclusion

We have shown here ~5 nm perovskite nanocrystals can be directly synthesized by spin-coating from perovskite-precursor/alumina-nanoparticle blend solution. Quantum-confinement caused the wavelength of the composite films to blue-shift by as much as 20 nm. The photoluminescence of the composite films is more efficient and environmentally more stable than the perovskite-only film. Spectroscopic studies indicate that the PLQE of the composite film is 25% at high excitation power density and the composite films have longer PL life time than the perovskite-only film.

References

1. Lee, M.M., Teuscher, J., Miyasaka, T., Murakami, T.N., and Snaith, H.J., *Efficient hybrid solar cells based on meso-superstructured organometal halide perovskites.* Science, **338**, 643-647(2012).
2. Kim, H.-S., Lee, C.-R., Im, J.-H., Lee, K.-B., Moehl, T., Marchioro, A., Moon, S.-J., Humphry-Baker, R., Yum, J.-H., and Moser, J.E., *Lead iodide perovskite sensitized all-solid-state submicron thin film mesoscopic solar cell with efficiency exceeding 9%.* Scientific reports, **2**, 2012).
3. Tanaka, K., Takahashi, T., Ban, T., Kondo, T., Uchida, K., and Miura, N., *Comparative study on the excitons in lead-halide-based perovskite-type crystals* $CH_3NH_3PbBr_3$ $CH_3NH_3PbI_3$. Solid state communications, **127**, 619-623(2003).
4. Sadhanala, A., Deschler, F., Thomas, T.H., Dutton, S.n.E., Goedel, K.C., Hanusch, F.C., Lai, M.L., Steiner, U., Bein, T., and Docampo, P., *Preparation of Single-Phase Films of* $CH_3NH_3Pb(I_{1-x}Br_x)_3$ *with Sharp Optical Band Edges.* The Journal of Physical Chemistry Letters, **5**, 2501-2505(2014).
5. Schwartz, R.W., *Chemical solution deposition of perovskite thin films.* Chemistry of Materials, **9**, 2325-2340(1997).
6. Salim, T., Sun, S., Abe, Y., Krishna, A., Grimsdale, A.C., and Lam, Y.M., *Perovskite-based solar cells: impact of morphology and device architecture on device performance.* Journal of Materials Chemistry A, **3**, 8943-8969(2015).
7. Chukwuocha, E.O., Onyeaju, M.C., and Harry, T.S., *Theoretical studies on the effect of confinement on quantum dots using the brus equation.* 2012).
8. Zheng, K., Zhu, Q., Abdellah, M., Messing, M.E., Zhang, W., Generalov, A., Niu, Y., Ribaud, L., Canton, S.E., and Pullerits, T., *Exciton Binding Energy and the Nature of Emissive States in Organometal Halide Perovskites.* The Journal of Physical Chemistry Letters, **6**, 2969-2975(2015).
9. Deschler, F., Price, M., Pathak, S., Klintberg, L.E., Jarausch, D.-D., Higler, R., Hüttner, S., Leijtens, T., Stranks, S.D., and Snaith, H.J., *High photoluminescence efficiency and optically pumped lasing in solution-processed mixed halide perovskite semiconductors.* The Journal of Physical Chemistry Letters, **5**, 1421-1426(2014).

10. Stranks, S.D., Burlakov, V.M., Leijtens, T., Ball, J.M., Goriely, A., and Snaith, H.J., *Recombination kinetics in organic-inorganic perovskites: Excitons, free charge, and subgap states.* Physical Review Applied, **2**, 034007(2014).

11. Schmidt, L.C., Pertegás, A., González-Carrero, S., Malinkiewicz, O., Agouram, S., Mínguez Espallargas, G., Bolink, H.J., Galian, R.E., and Pérez-Prieto, J., *Nontemplate synthesis of $CH_3NH_3PbBr_3$ perovskite nanoparticles.* Journal of the American Chemical Society, **136**, 850-853(2014).

12. Zhang, F., Zhong, H., Chen, C., Wu, X.-g., Hu, X., Huang, H., Han, J., Zou, B., and Dong, Y., *Brightly Luminescent and Color-Tunable Colloidal $CH_3NH_3PbX_3$ (X= Br, I, Cl) Quantum Dots: Potential Alternatives for Display Technology.* ACS nano, **9**, 4533-4542(2015).

Chapter 7

This chapter is restructured from a published paper [1]. This work was carried out in collabration with Florencia Wisnivesky Rocca Rivarola, Nathaniel J. L. L. Davis, Sai Bai, Tom C. Jellicoe, Francisco de la Pena, Shaocong Hou, Caterina Ducati, Feng Gao, and supervised by Richard H. Friend, Neil C. Greenham, Zhi-Kuang Tan. G.Li developed the crosslinking method, performed most experiments and data analyses. F. W. R. Rivarola carried out the TEM characterization and analysis. N. J. L. K. Davis, T. C. Jellico and G. Li synthesized and optimized perovskite crystals. S. Bai synthesized and optimized ZnO nanoparticles. S. Hou, G. Li and Z. K. Tan collected and analysed the FTIR data. F. D. L. Peña and F. W. R. Rivarola generated the EELS mapping images. C. Ducati supervised the work of F. W. R. Rivarola and F. D. L. Peña. F. Gao supervised the work of S. Bai. Z.K.Tan initiated the project. Z.K.Tan, N.C.Greenham and R.H.Friend. guided the whole project.

Highly-Efficient Perovskite Nanocrystal Light-Emitting Diodes Enabled by a Universal Cross-linking Method

Metal-halide perovskite semiconductors have attracted significant research interest, due to a combination of low-cost solution processability and remarkable performance in optoelectronic devices. In 2014, infrared and visible electroluminescence was demonstrated in methylammonium lead halide perovskites, using a charge-confined diode structure to achieve effective radiative recombination. However, the use of methylammonium halide, which is a chemical combination of gaseous methylamine and hydrogen halide, necessarily limits the thermal stability of these perovskite devices. Replacing methylammonium with inorganic cesium offers the perovskite extra thermal stability up to its melting at ~500 °C, but makes it more intractable towards solution processing. Recently, Protesescu et al. demonstrated the synthesis of cesium lead halide perovskite nanocrystals, following the traditional approaches of growing and stabilizing semiconductor particles in the presence of

aliphatic ligands. These perovskite nanocrystals are highly luminescent and emit over the full visible range, making them ideal candidates for luminescent display applications. Here, we show the preparation of highly-efficient perovskite light-emitting diodes (PeLED) using solution-processed nanocrystals. We apply a new trimethylaluminum (TMA) vapour-based cross-linking method to render the nanocrystal films insoluble, thereby allowing the deposition of subsequent charge-injection layers without the need for orthogonal solvents. The resulting near-complete nanocrystal film coverage, coupled with the natural confinement of injected charges within the perovskite crystals, facilitate electron-hole capture and give rise to a remarkable electroluminescence yield of more than 5%.

7.1 Background

Over the past two decades, research into semiconductor nanocrystals has led to their well-controlled syntheses [2, 3], as well as an interesting array of luminescent device and phosphor applications [4-8]. Nanocrystals generally benefit from solution-processability, bandgap tunability by the quantum size effect [9], narrow-width emission, and high photo- and electro-luminescence yield. Recent success in the synthesis of cesium lead halide perovskite nanocrystals has opened up interesting opportunities towards the photo-physical investigations of these materials, and further allows their commercial exploitation in the form of full-color flat panel displays and lighting [10]. So far, perovskite nanocrystals are shown to have color-pure emission, close to unity photoluminescence yield and low lasing thresholds [11]. The synthetic steps are generally straightforward, and the easy control of halide content allows the perovskite bandgaps to be tailored, both by chemical compositions as well as by quantum size effects.

7.2 LED Device Fabrication

We demonstrate strong and color-tunable electroluminescence from cesium lead halide perovskite nanocrystals in a light-emitting diode structure. Figure 7.1(A) shows the device architecture of our perovskite nanocrystal light-emitting diode, and Figure 7.1(B) shows the energy-level diagram of the materials within the device stack. Here,

our electron-injection layer comprises a film of zinc oxide (ZnO) nanocrystals, directly deposited on an indium tin oxide (ITO)-coated glass substrate [12]. The cesium lead halide nanocrystals were solution-coated onto the ZnO film as the emissive layer. Due to the presence of aliphatic ligands on the nanocrystals, the perovskite film remains soluble to organic solvents, which limits the deposition of subsequent charge-injection layers using solution methods. We employed a new trimethylaluminum (TMA) vapour-phase crosslinking technique to fix the nanocrystal film in place, thereby enabling us to solution-cast a layer of TFB polymer(poly[(9,9-dioctylfluorenyl-2,7-diyl)-co-(4,4′-(N-(4-sec-butylphenyl)diphenylamine)]) above without washing the nanocrystals off. TFB serves primarily as a hole-injection and electron-blocking layer. A thin, high work-function molybdenum trioxide (MoO_3) interlayer and silver electrode were vacuum-thermal evaporated to complete the device.

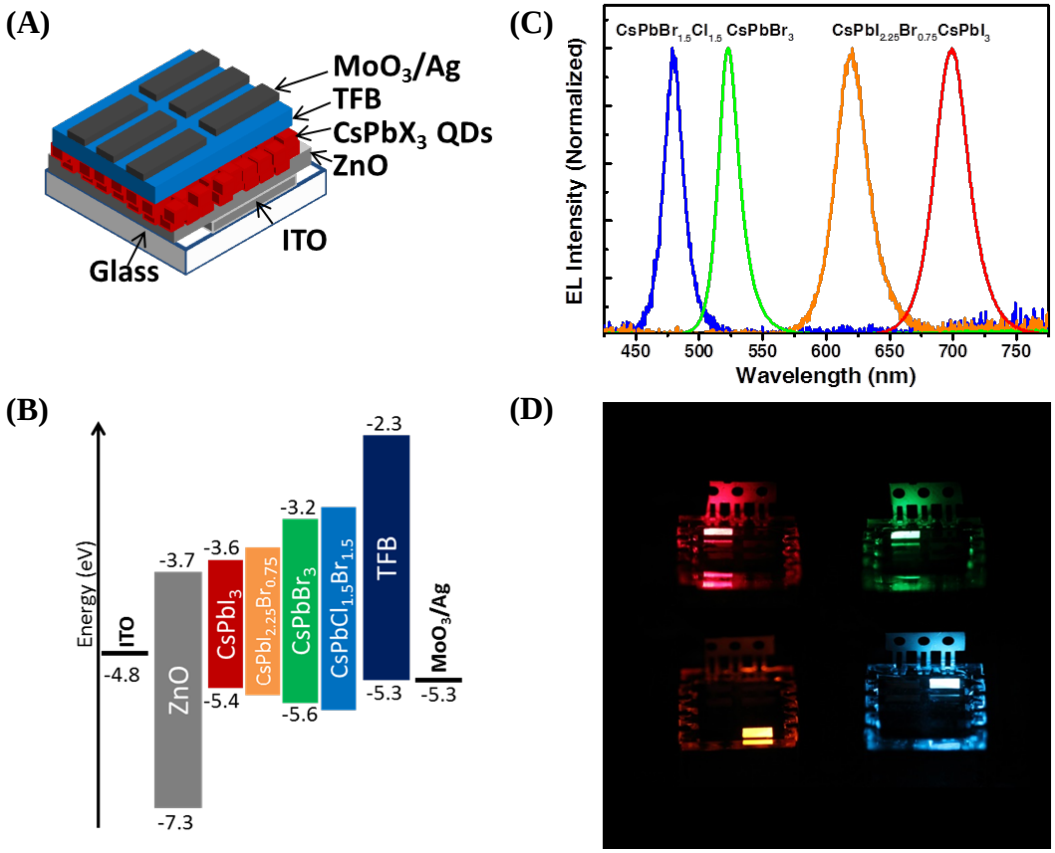

Figure 7.1 (A) Perovskite nanocrystal light-emitting diode with ITO/ZnO/$CsPbX_3$/TFB/MoO_3/Ag device architecture, where X represents I, Br or Cl. (B) Energy-level diagram showing the valence and conduction band levels of

the materials in the device. Energy levels were estimated from literature values, without taking into account the quantum size effects [13, 14]. Bandgap energies were estimated from the EL emission peaks. (C) Electroluminescence spectra of red, orange, green and blue emitting perovskite nanocrystal LEDs. (D) Images of perovskite nanocrystal LEDs in operation.

Detailed device fabrication steps:

7 mg/ml ZnO nanoparticle dissolved in ethanol was spin-coated on ITO substrate at 1500 rpm for 30 s, before being annealed in an inert glovebox at 100 °C for 10 minutes. 10 mg/ml perovskite QDs dissolved in hexane was spin-coated at 1000 to 8000 rpm for 20 s in air to give a 15-60 nm film. After drying for 10 minutes, they are taken to the ALD chamber for treatment. TFB dissolved in toluene was then spin-coated on top at 2000 rpm for 30 s in glovebox to give a 50 nm thin film. 5 nm MoO_3 and 80 nm Ag were then thermal evaporated in a high-vacuum of below 5×10^{-6} mbar.

As shown in Figure 7.1(C) and 7.1(D), our perovskite nanocrystal devices show saturated and colour-pure emission. We control the perovskite bandgap, primarily by tailoring the halide composition, and achieve electroluminescence across a wide range of the visible spectrum. Our red, orange, green and blue devices emit at wavelengths of 698 nm, 619 nm, 523 nm and 480 nm, respectively. All devices exhibit narrow-width emission, with their full-width at half maxima (FWHM) in the range of 17 to 31 nm. The red and green LEDs were made, respectively, from the pure iodide and pure bromide perovskites, while the orange and blue LEDs were made from mixed-halide perovskites, with $CsPbI_{2.25}Br_{0.75}$ and $CsPbBr_{1.5}Cl_{1.5}$ compositions, respectively.

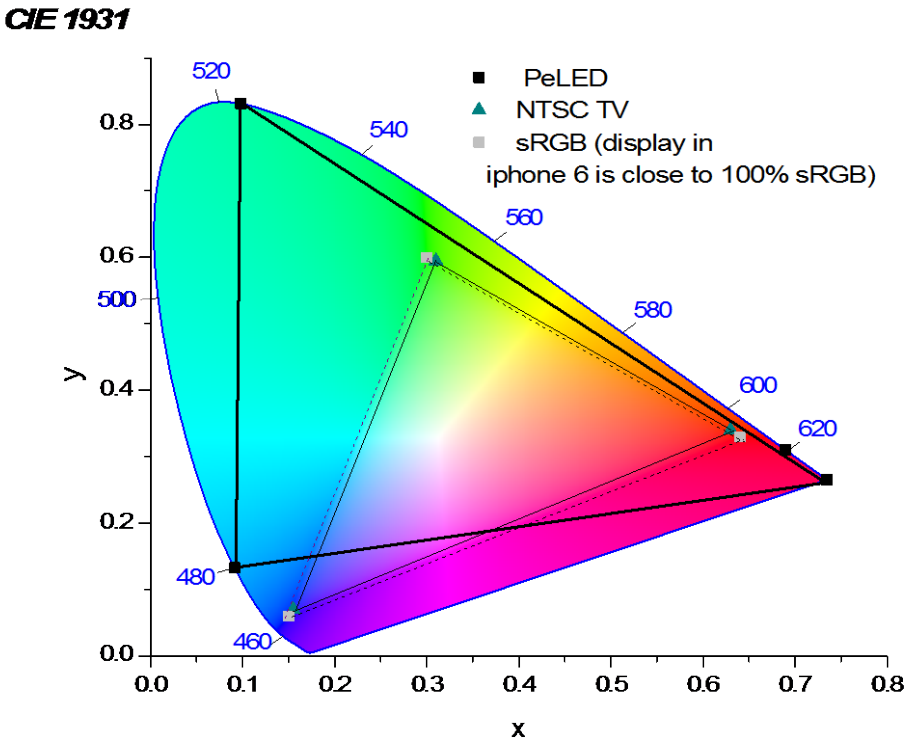

Figure 7.2 Comparison of the colour gamut of our PeLED with the current technology on market.

We plot the emission of our LEDs on the CIE 1931 diagram together with sRGB and NTSC standards, as shown in Figure 7.2. The colour saturation of our PeLEDs is higher, and the gamut formed by our red, green and blue LEDs is much larger than the current industry standard.

7.3 Cross-linking method and characterization

The crosslinking of the perovskite nanocrystals was critical towards the realization of our device structure. Traditionally, nanocrystals have been crosslinked, or made insoluble, using ligand exchange techniques, where shorter-chain bi-functionalized organic ligands (eg. diamines or dithiols) were applied to replace the longer-chain oleyl ligands [15, 16]. However, the replacement with smaller ligands often creates cracks and gaps within the nanocrystal film, which could lead to electrical shunts and reduced device performance. Closer packing of the nanocrystals could also lead to the self-quenching of the nanocrystals and a lower photoluminescence yield [17], often caused by a more effective Förster resonant energy transfer (FRET) to non-radiative sites [18]. Here, crosslinking is achieved by exposing the perovskite nanocrystal film to short pulses of TMA vapour within an enclosed vacuum chamber at room temperature, followed by standing the treated film in ambient air (Figure 7.3). This creates a well-connected network of aluminum oxide/hydroxide that links the nanocrystals together, hence rendering them insoluble. This vapour-phase technique does not involve ligand exchange processes, and is therefore useful in crosslinking the nanocrystals without altering the original crystal arrangements, thereby allowing much of the film's original structural and electronic properties to be preserved. The photoluminescence spectra of the nanocrystals also remain unchanged after the TMA treatment, hence confirming that the crosslinking has no effect on their optical bandgap. (Note that we use a slightly-modified TMA treatment procedure for the blue-emitting nanocrystals - see Figure 7.4).

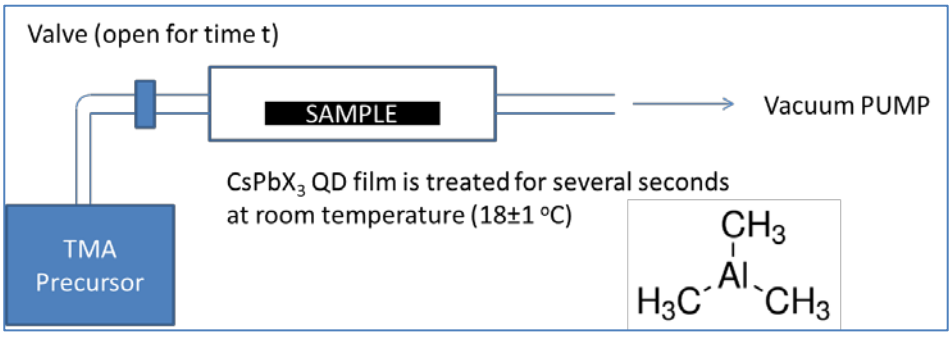

Figure 7.3 Illustration off the setup to crosslink the perovskite quantum dots. Note: the films were left in air for a few minutes to complete the reaction of TMA.

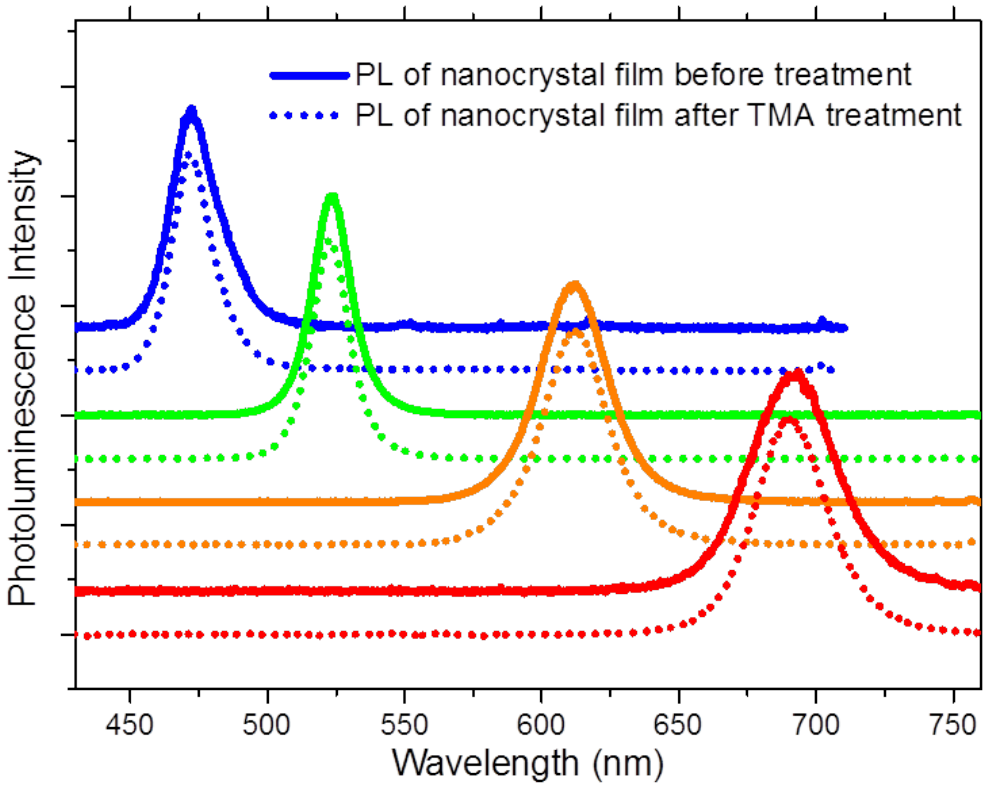

Figure 7.4 PL emission spectra of perovskite nanocrystal films before and after TMA treatment. From top to bottom: $CsPbBr_{1.5}Cl_{1.5}$, $CsPbBr_3$, $CsPbI_{2.25}Br_{0.75}$ and $CsPbI_3$.

Note: PL of $CsPbI_{2.25}Br_{0.75}$ was observed to slightly red-shift upon prolonged (>20 s) TMA treatment. PL of $CsPbBr_{1.5}Cl_{1.5}$ red-shifts under typical TMA treatment procedures, but reducing the TMA partial pressure to below ~0.005 mbar and introducing pulses of water vapour between TMA pulses helps to preserve the optical properties of $CsPbBr_{1.5}Cl_{1.5}$.

Detailed cross-linking steps:

A BENEQ TFS20 atomic layer deposition (ALD) system was used for the vapour-phase crosslinking treatment. High purity trimethylaluminium (TMA) was purchased from SAFC Hitech. Deposition temperature was set at 18±1 °C, which is also the typical ambient room temperature. Reactor chamber was pumped down below 0.2 mbar before starting the process. TMA was applied in short pulses at a partial pressure of ~0.01 mbar. The dosage of TMA was controlled by varying the

total length of TMA pulses between 0.25 s and 20 s. The duration of each pulse was limited to 1s, hence a 10s dosage is, for instance, achieved with 10×1s pulses.

In order to investigate the effectiveness of crosslinking, we varied the exposure of the perovskite nanocrystals to different pulse durations of TMA vapour, and measured the nanocrystal retention upon washing with toluene. The crystal retention ratio was determined by the ratio of absorbance at the first absorption peak of the nanocrystal films. As shown in Figure 7.5(A), the crosslinking was remarkably rapid even at room temperature, and a near complete retention of nanocrystals was achieved in less than 0.5 s of TMA exposure. The inset SEM images show a significant wash-off for the non-crosslinked nanocrystals, while the TMA-treated nanocrystals were completely retained after washing. Interestingly, we observe a corresponding increase in the photoluminescence quantum efficiency (PLQE) of $CsPbI_3$ and $CsPbBr_3$ with TMA treatment, but a decrease in the case of $CsPbBr_{1.5}Cl_{1.5}$ (see Figure 7.5(B)). This PL enhancement is particularly remarkable for the $CsPbI_3$ nanocrystals, raising its PLQE by more than a factor of 3, from ~25% in the untreated film to ~85% in the TMA-treated film. We note that this is possibly one of the highest PLQEs achieved in a non-core-shell structured nanocrystal thin film.

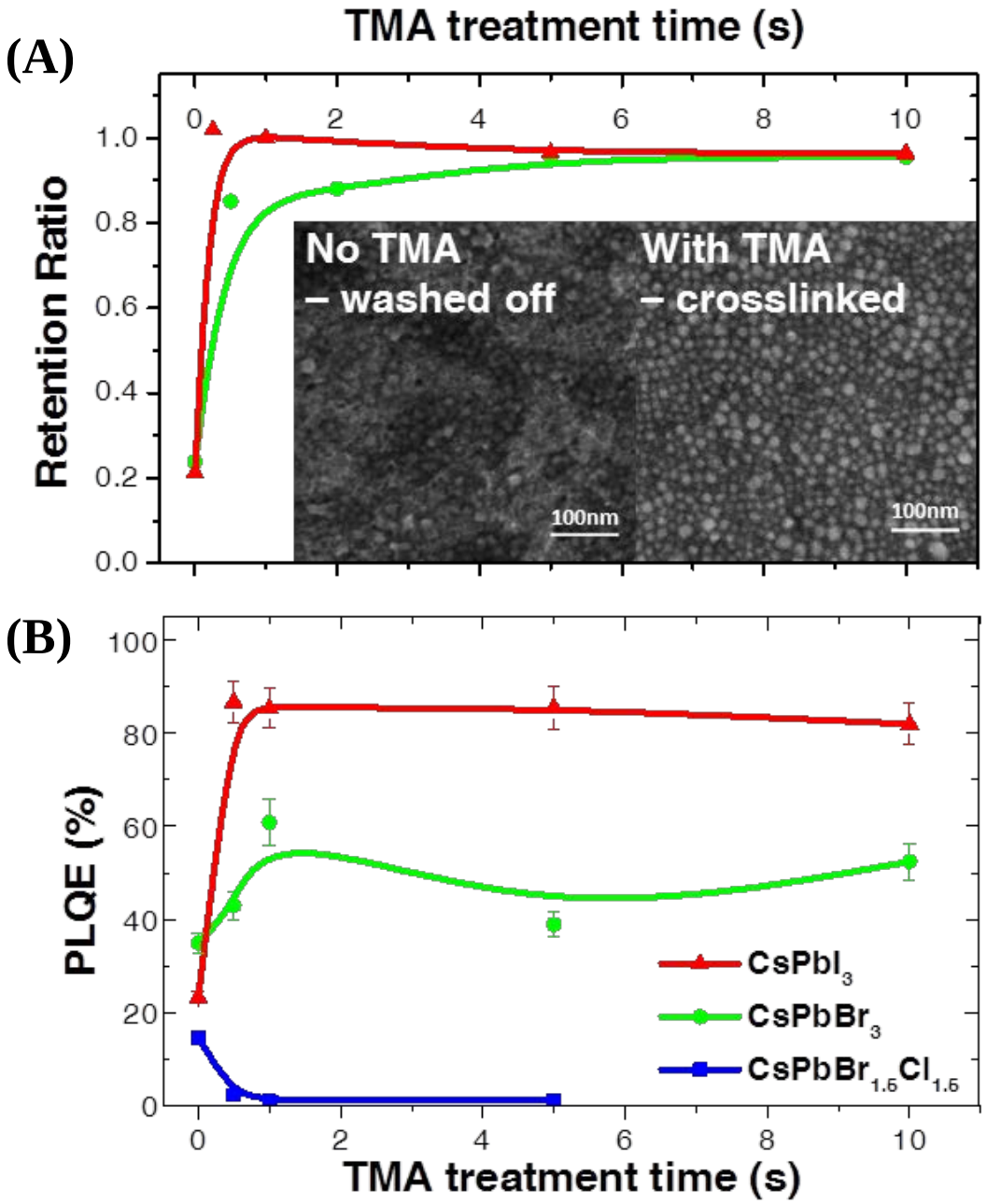

Figure 7.5 (A) Retention ratio of TMA-treated and non-treated perovskite nanocrystal upon washing with toluene, plotted against the duration of TMA treatment. Inset images show the SEM micrographs of washed off and crosslinked perovskite nanocrystals ($CsPbI_3$), upon washing with toluene (B) Photoluminescence quantum efficiency (PLQE) of perovskite nanocrystals, plotted against the duration of TMA crosslinking treatment

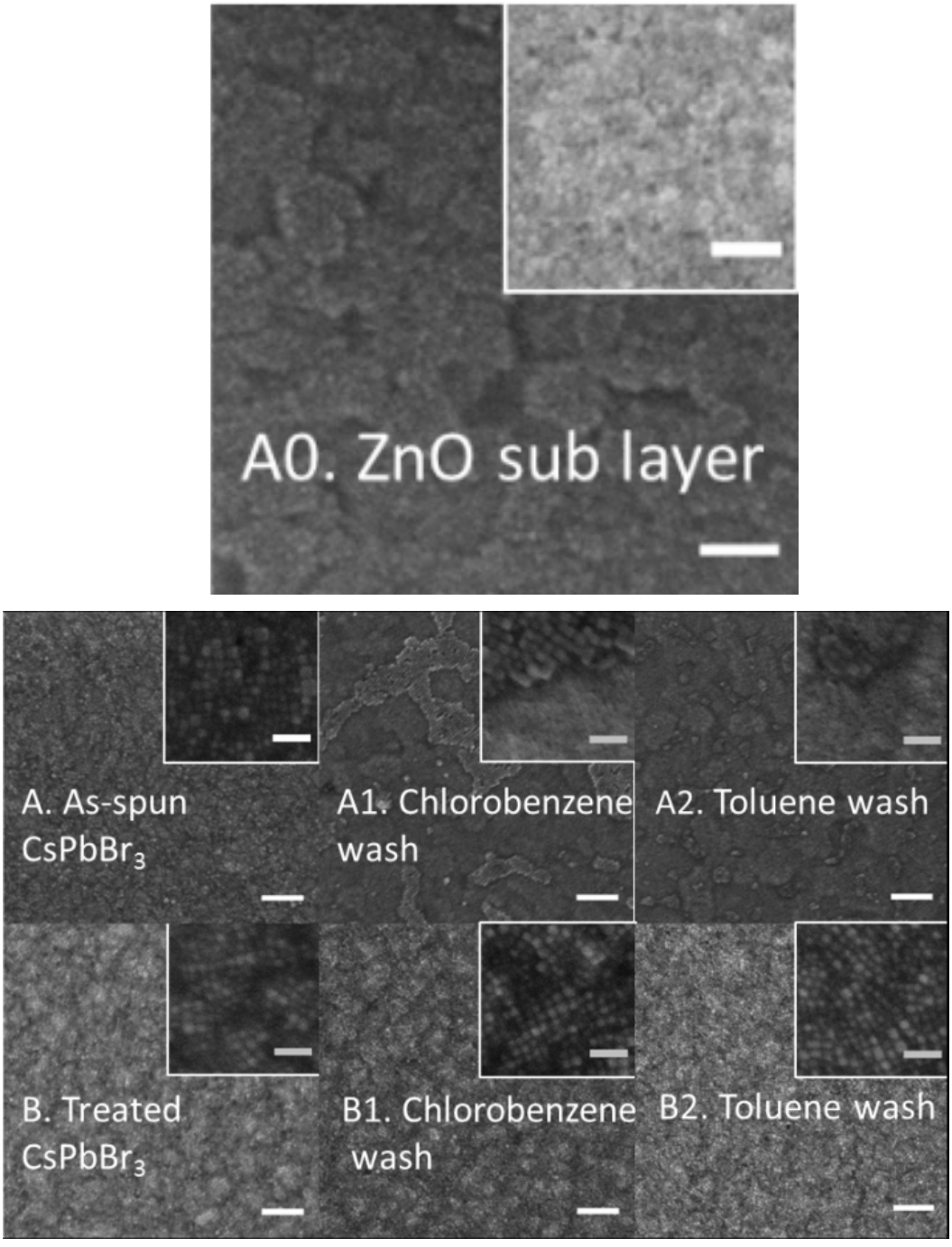
A0. ZnO sub layer
A. As-spun $CsPbBr_3$
A1. Chlorobenzene wash
A2. Toluene wash
B. Treated $CsPbBr_3$
B1. Chlorobenzene wash
B2. Toluene wash

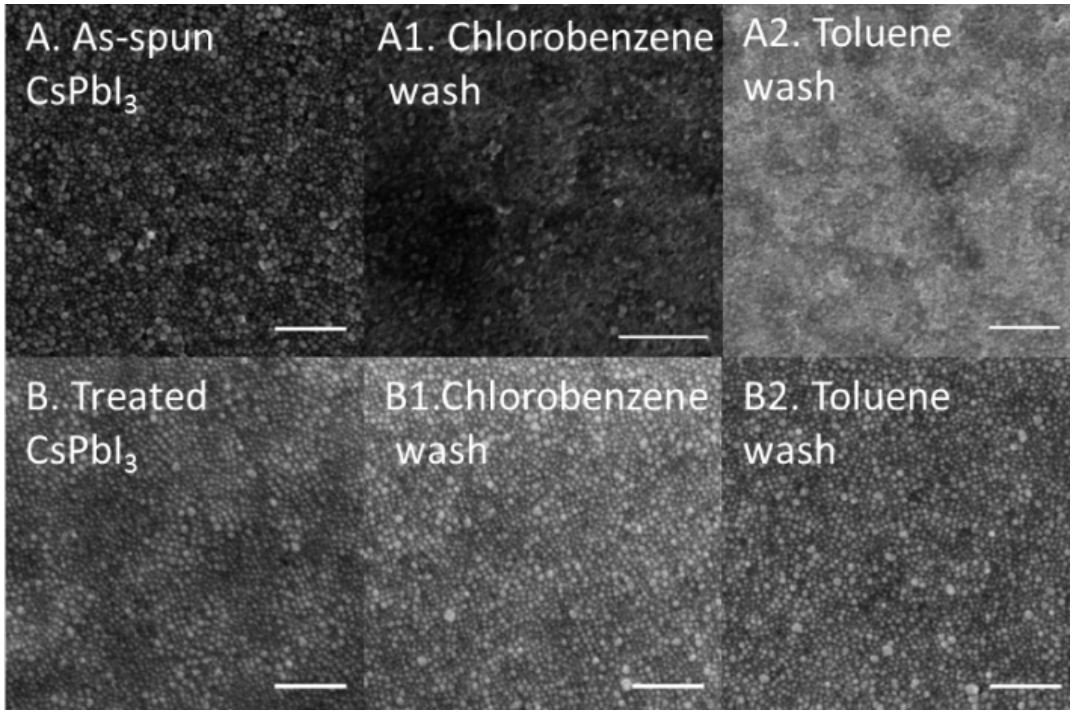

Figure 7.6 Top-view SEM images: (A0) ITO/ZnO, (A) ITO/ZnO/$CsPbBr_3$ and washed film of (A) by (A1) chlorobenzene and (A2) toluene; (B) ITO/ZnO/$CsPbBr_3$ film treated with TMA for 5 seconds and washed film of (B) by (B1) chlorobenzene and (B2) toluene. Scale bar for main image and inset are 200 nm and 50 nm, respectively. Bottom SEM images:(A) ITO/ZnO/$CsPbI_3$ and washed film of (A) by (A1) chlorobenzene and (A2) toluene; (B) ITO/ZnO/$CsPbI_3$ film treated with TMA for 10 seconds and washed film of (B) by (B1) chlorobenzene and (B2) toluene. Scale bar for main image and inset are 200 nm and 50 nm, respectively.

More detailed SEM images of the crosslinked film upon washing off with different organic solvents are shown in Figure 7.6. The chlorobenzene-washed un-treated films only have a few patches of nanocrystals remaining (Top A1, Bottom A1), the toluene washed un-treated samples have almost all the crystals washed away (Top A2, Bottom A2). After crosslinking, the washing by chlorobenzene or toluene does not show obvious impact on film coverage and morphology (Top B1/B2, Bottom B1/B2).

In an attempt to unravel the origins of the PL enhancement, we took high-resolution transmission electron microscopy (HRTEM) images (Figure 7.7 (A)) and high-angle annular dark field scanning TEM (HAADF-STEM) images (Figure 7.6 (B))

of the $CsPbI_3$ perovskite nanocrystals before and after the TMA treatment. The nanocrystals show an average size of 19 nm (see Figure 7.8 (A)), which points to minimal quantum confinement in their electronic bandgap [10]. We analyzed the spacing distribution between the nanocrystals in the HRTEM images, and found the average crystal spacing to increase from 1.6 nm to 1.9 nm upon TMA treatment. We note that a spacing of 1.6 nm between the crystals represents approximately 0.55 ligand attachment per unit cell of the perovskite lattice. The spacing distribution analysis is shown in Figure 7.8 (B).

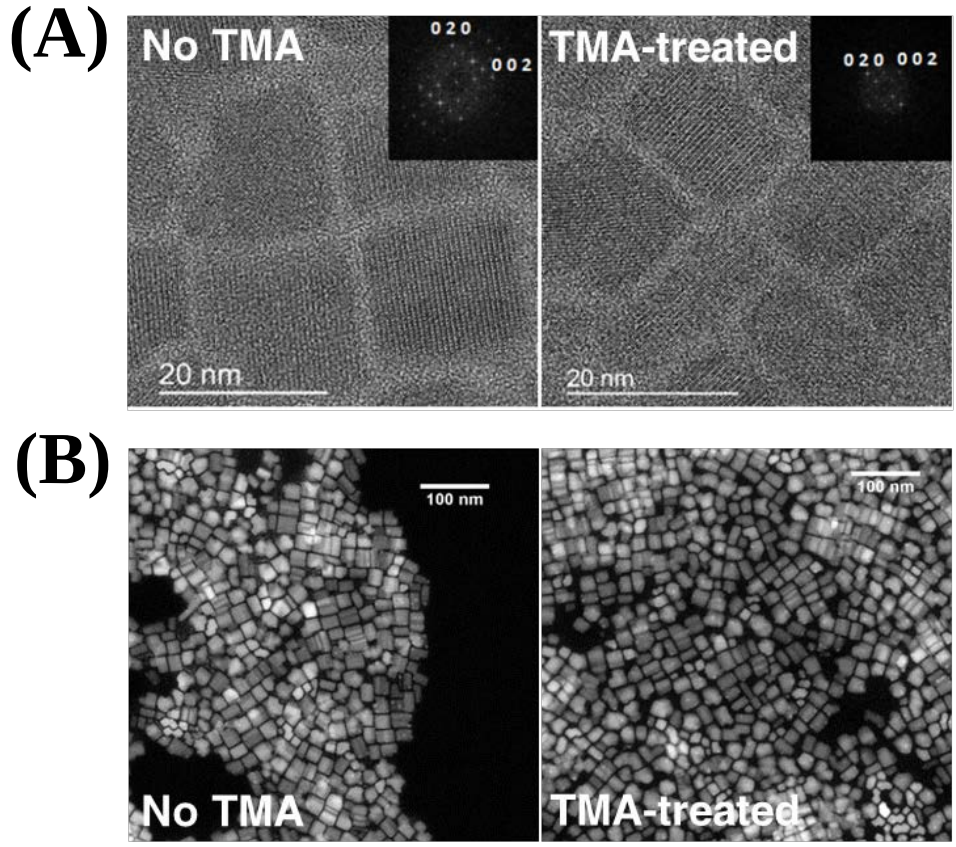

Figure 7.7 (A) High-resolution TEM (HRTEM) images of untreated and TMA-treated $CsPbI_3$ nanocrystals. The insets show the Fast Fourier Transform (FFT) for the nanocrystals. Both samples were imaged on the [1 0 0] zone axis. (B) High-angle annular dark field scanning TEM (HAADF-STEM) images of untreated and TMA-treated $CsPbI_3$ nanocrystals The TEM images show that the nanocrystals are well dispersed and single crystalline.

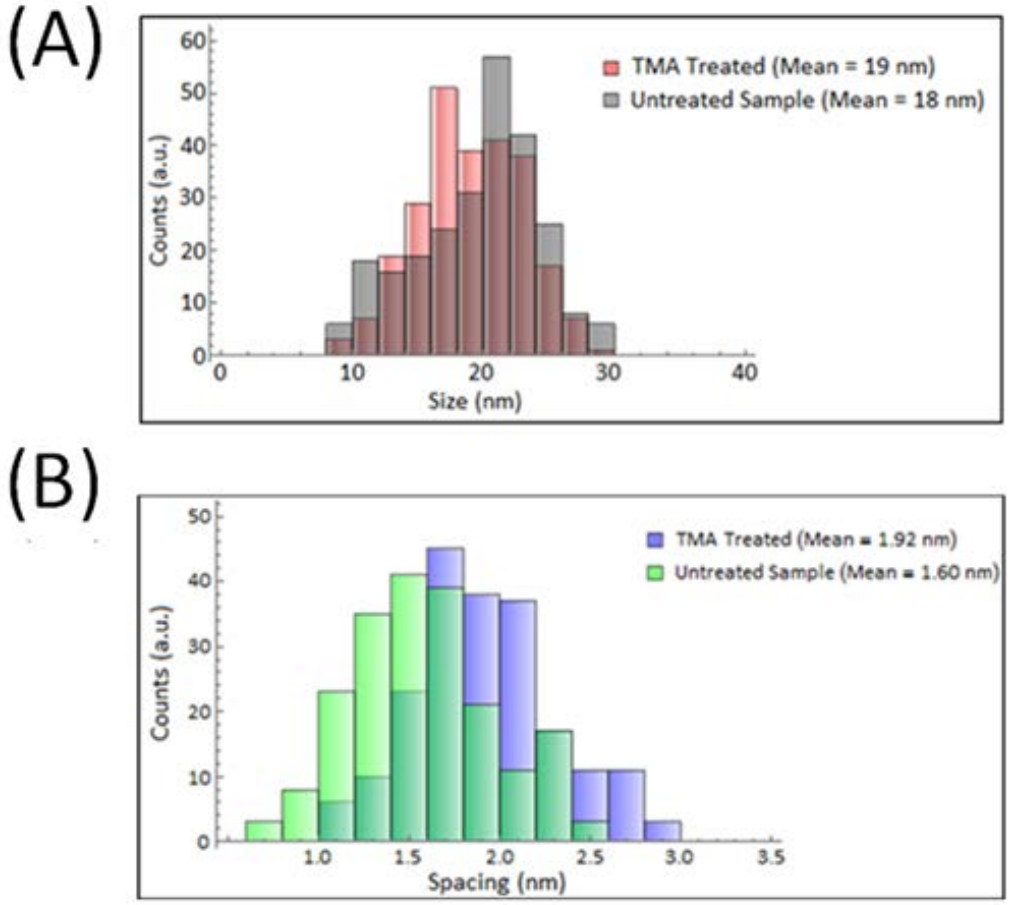

Figure 7.8 (A) Nanocrystal size distribution for the untreated and TMA-treated $CsPbI_3$. The particle size was determined by individually measuring the nanocrystal size on the HAADF-STEM images. (B) Nanocrystal spacing distribution for untreated and TMA-treated $CsPbI_3$. The spacing was determined from the HRTEM images. Analysis of the nanocrystal spacing for the treated and untreated samples shows an average increase of 0.3 nm after TMA treatment.

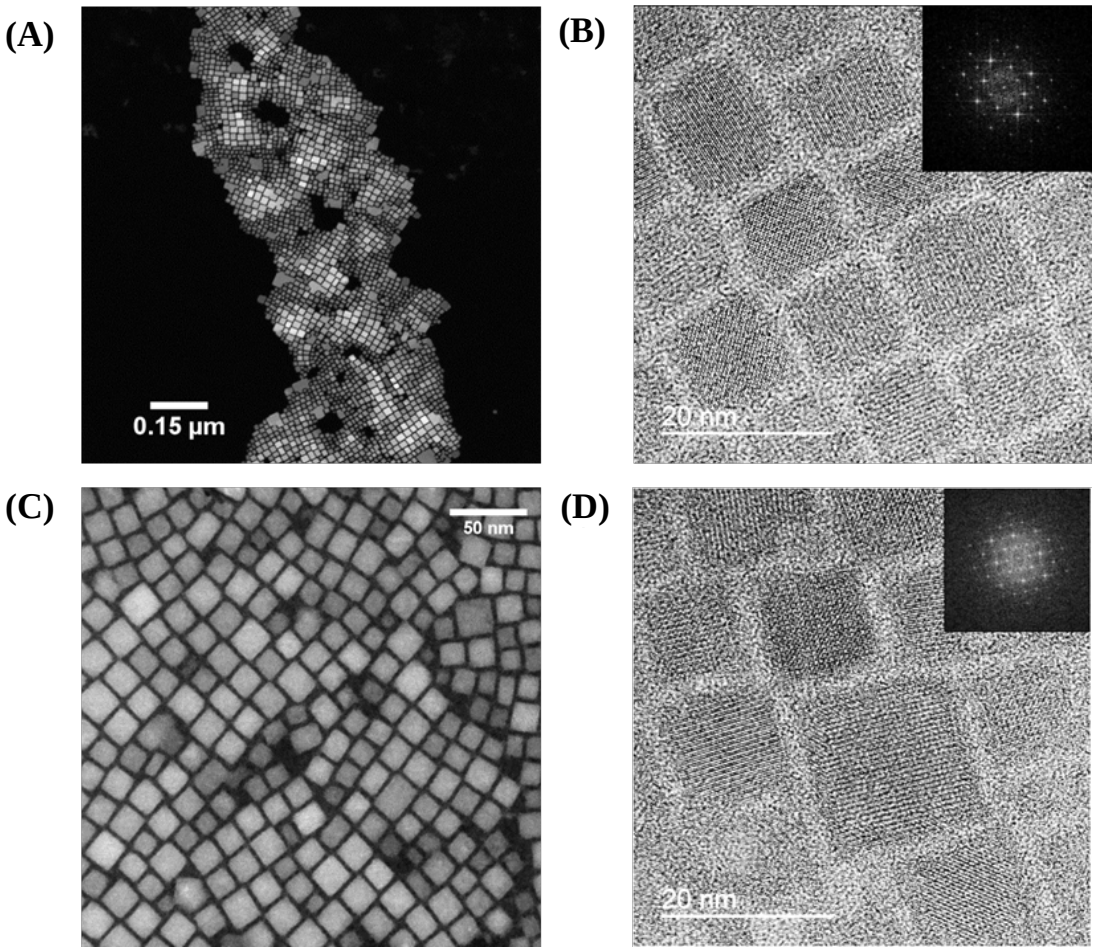

Figure 7.9 (A) HAADF-STEM and (B) HRTEM images of untreated $CsPbBr_3$ nanocrystals. (C) HAADF-STEM and (D) HRTEM of TMA-treated $CsPbBr_3$ nanocrystals.

The TEM images of the treated and untreated $CsPbBr_3$ nanocrystals are shown in Figure 7.9. The crystals are intact under the TMA treatment. The average size of the crystals is 9 nm in diameter.

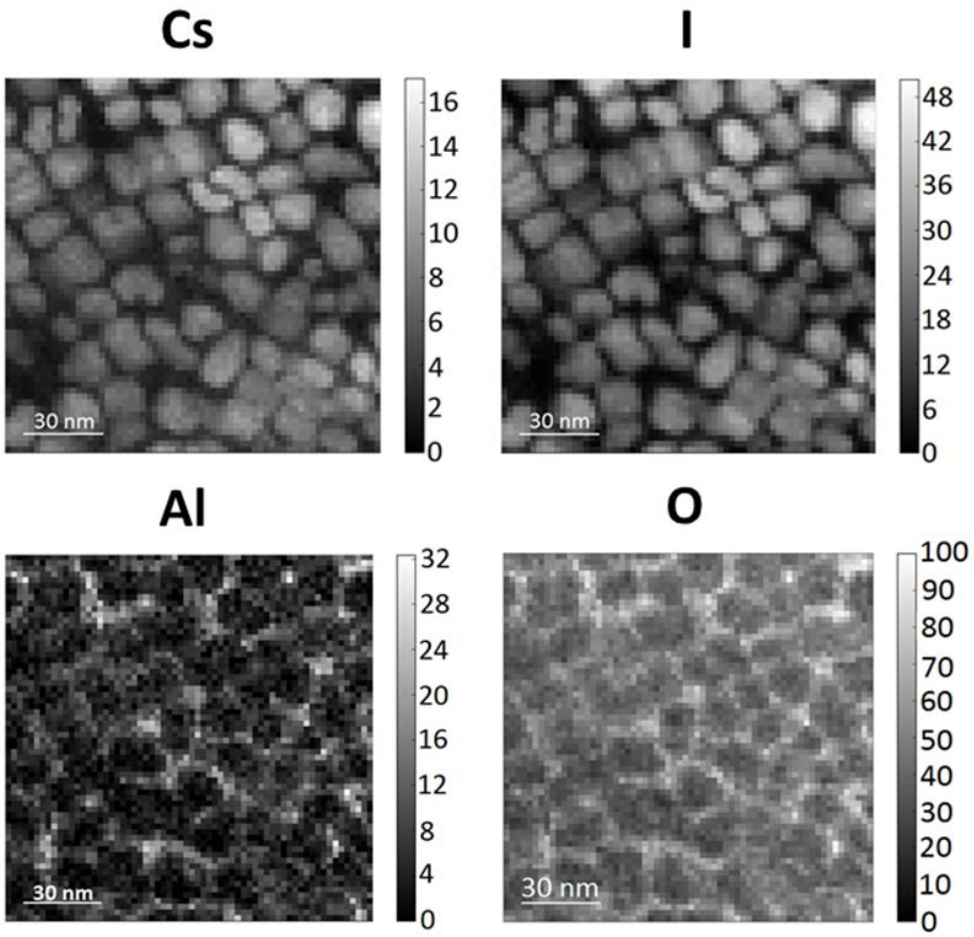

Figure 7.10 Cesium, iodine, aluminum and oxygen elemental maps obtained by quantitative analysis of an EELS spectrum image. Intensity units are arbitrary but the same for all maps.

We further analyzed the distribution of main elements within the samples using electron energy loss spectroscopy (EELS) mapping (Figure 7.10) The EELS maps show that aluminum and oxygen elements are located primarily in the gaps between the cesium and iodine rich nanocrystal domains, thereby indicating that the TMA treatment successfully creates an alumina network that covers all areas surrounding and in-between the crystals. The intercalation of alumina among the ligands, therefore, accounts for the small increase in the crystal spacing. While this 0.3 nm increase in spacing may lead to a smaller degree of PL quenching by FRET, it is unlikely to fully account for the 3-fold enhancement in PL yield. The changes in PL are therefore likely to be chemical in nature, where the introduction of TMA chemically passivates the nanocrystal surface and leads to a reduction in PL-quenching defects [19].

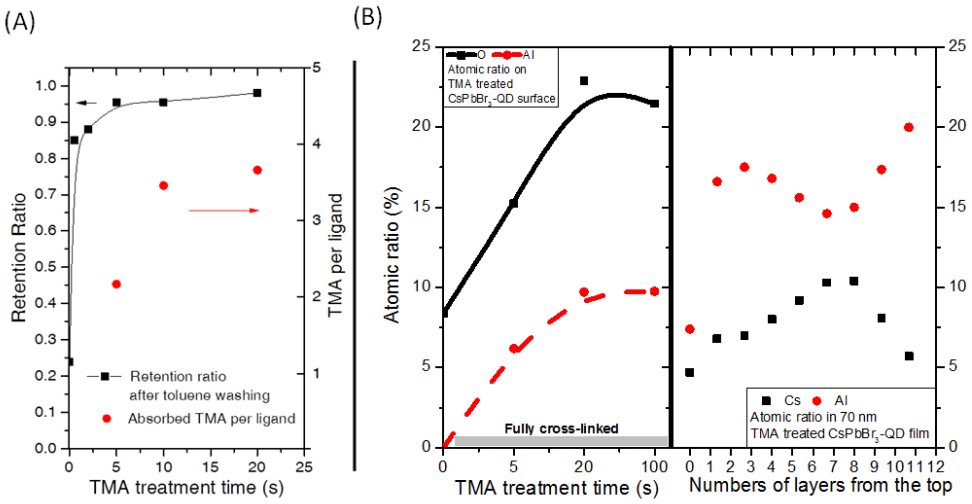

Figure 7.11 (A) Comparison of retention ratio and number of TMA absorbed per ligand. Number of TMA absorbed per ligand is estimated by atomic ratio of Al to C. (B) Atomic ratio of Al/(Al+O+C+Cs+Pb+Br) plotted against TMA treatment time. Atomic ratios are determined by x-ray photoelectron spectroscopy (XPS) measurements. (C) XPS depth profile of Al and Cs atomic ratios of a 70 nm $CsPbBr_3$ film, treated with TMA over 20 s. XPS measurements were performed in an ultrahigh-vacuum chamber (ESCALAB 250Xi) using an XR6 monochromatic X-ray source.

To further verify that the aluminum is incorporated between the crystal spacing and not just above the nanocrystal film, we measured the x-ray photoelectron spectra (XPS) of the sample as a function of film depth, The depth profile XPS was acquired by characterizing the nanocrystal films while an argon beam was in-situ applied to etch down the film. The etching rate is calculated by the thickness of the film (measured by AFM (~70 nm)) and the etching-through time (determined by where the peak of Cs atomic ratio is reached), assuming the etching rate is a constant. We found aluminum to be quite evenly distributed throughout the entire nanocrystal film thickness (Figure 7.11).

7.4 Cross-linking mechanism

To elucidate the chemical crosslinking mechanism, we measured the infra-red (IR) transmittance spectra of the oleic-acid- and oleylamine- capped nanocrystal samples before and after the TMA treatment. For comparison, we also measured the IR spectra of the organic ligands, and plotted them on the same graph in Figure 7.12. Three distinct changes could be observed in the IR spectra following the TMA treatment. 1) A broad peak centered around 3450 cm^{-1} is produced in all the TMA-treated samples, signally the presence of O-H stretch. This confirms hydroxide surface terminations as expected for an AlO_x network, and the role of ambient water in the crosslinking process. 2) Another broad peak appears around 630 cm^{-1}, and this is characteristic of vibrational modes in alumina [20]. 3) A strong and sharp band appears at 1576 cm^{-1} (for samples containing oleic acid), which can be assigned to weakened C=O stretching. This is particularly clear in the case of TMA-treated oleic acid. It is likely that the bonding of the carboxylate group to the strongly Lewis acidic aluminum causes the C=O bond to be weakened, thereby giving a lower than usual stretching frequency. Interestingly, the C=O stretching band does not appear in the pristine nanocrystal samples, but only emerges after TMA treatment. This is likely to be due to the coordination of the carboxylate group to the nanocrystals, thereby diminishing its double-bond character.

With this information, we propose a likely reaction mechanism for the crosslinking process as shown in Figure 7.12. The introduction of TMA coordinates and reacts with the carboxylate and amino groups of the ligands, adjacent to the nanocrystals. The subsequent exposure to ambient moisture hydrolyzes the remaining methyl-aluminum to give a network of alumina and aluminum hydroxide that are covalently bonded to the ligands. It is likely that the alumina that is formed next to the crystal surface successfully passivates the surface defects, thereby enhancing the crystals' photoluminescence yield. The strongly reactive TMA appears to be benign towards the iodide and bromide perovskites, but causes some level of damage to the chloride perovskites, hence resulting in a degradation of PL in the latter.

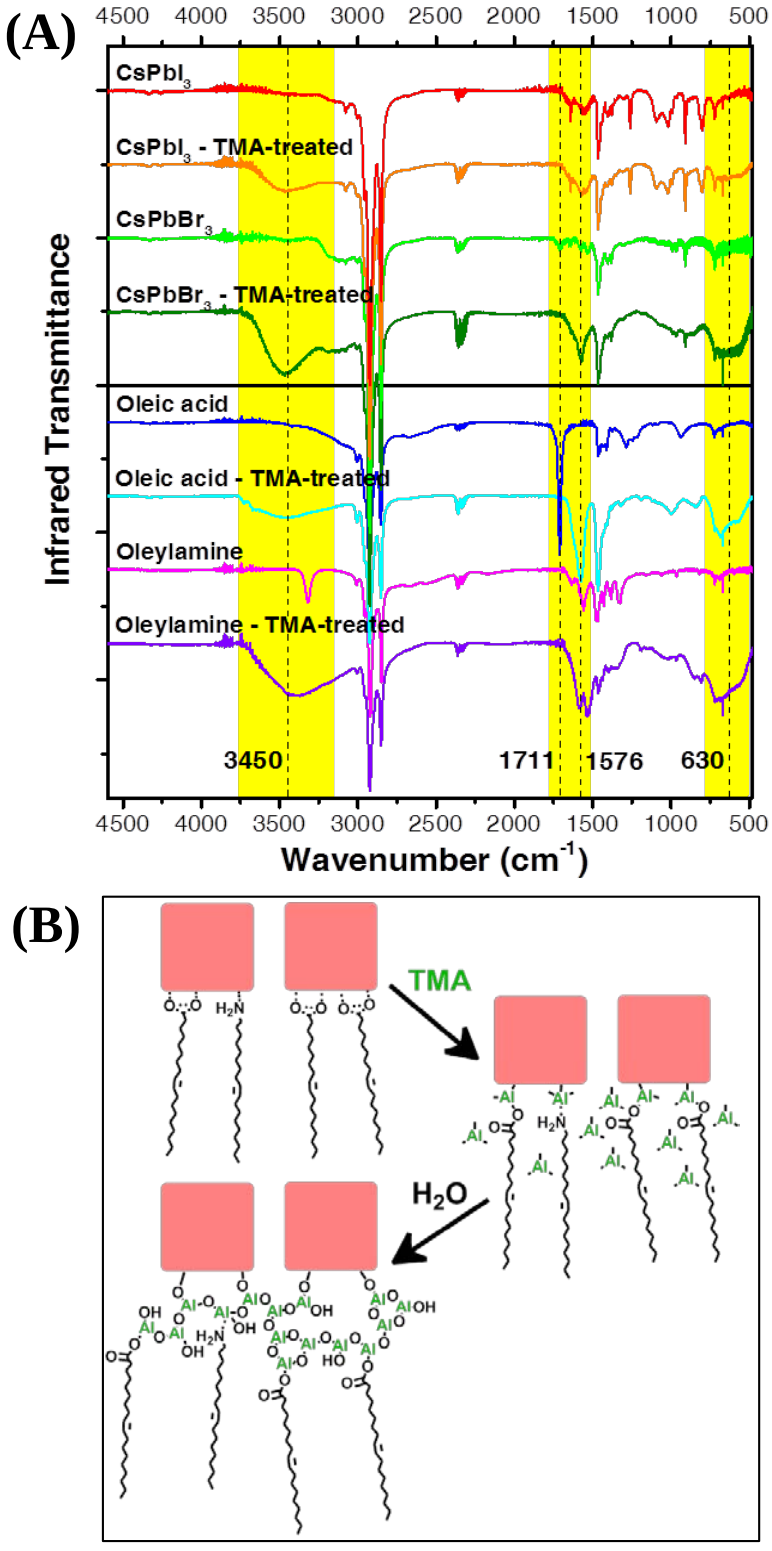

Figure 7.12 (A) Fourier transform infra-red (FTIR) spectra of perovskite nanocrystals and their ligands before and after TMA treatment (B) Reaction schematic of the TMA crosslinking process

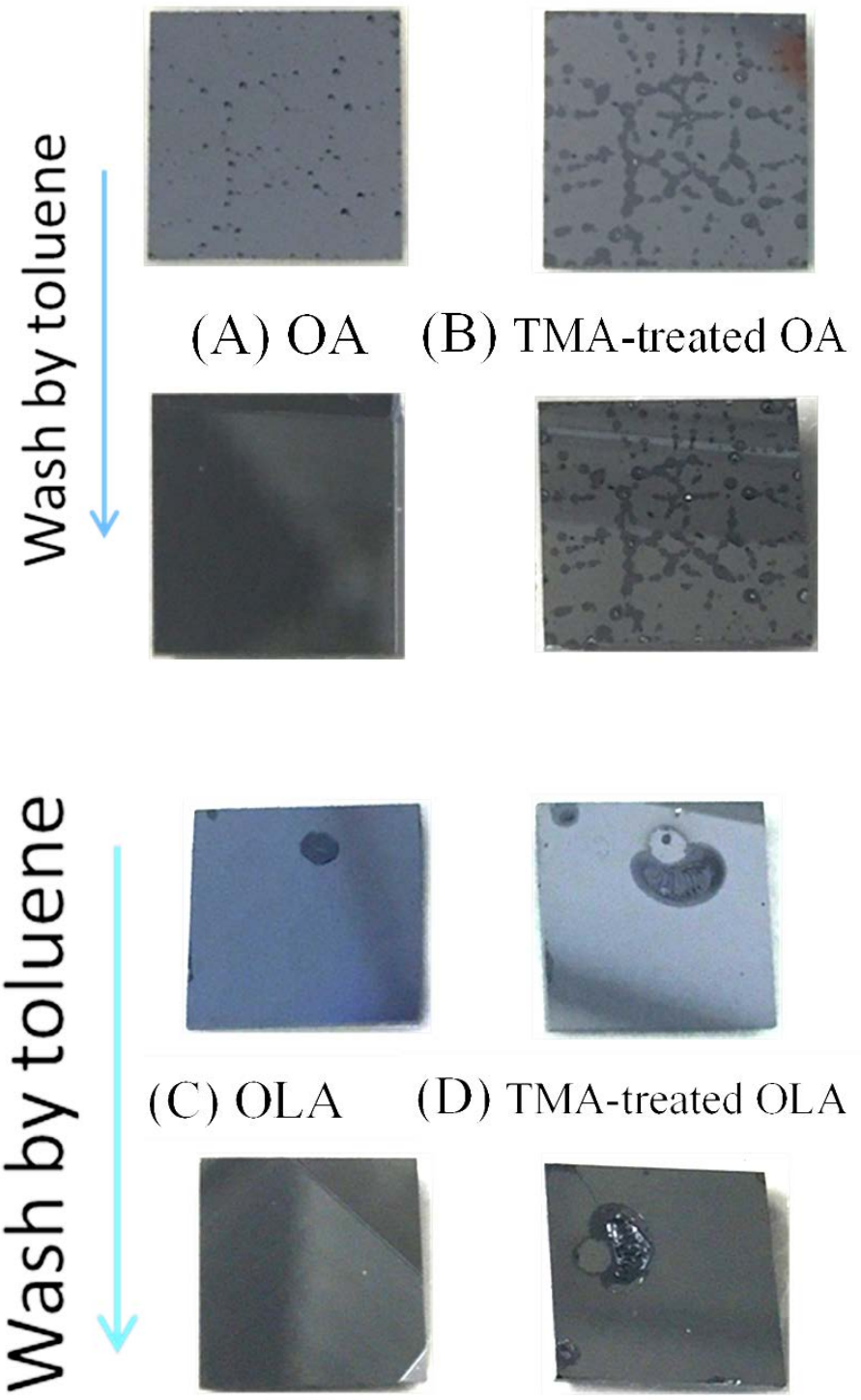

Figure 7.13 Photograph of (A) OA droplets deposited from solution in toluene, (B) TMA-treated OA droplets, (C) OLA droplets deposited from solution in toluene, (D) TMA-treated OLA droplets. Droplets were subsequently washed with toluene to test for crosslinking. Image contrast has been enhanced.

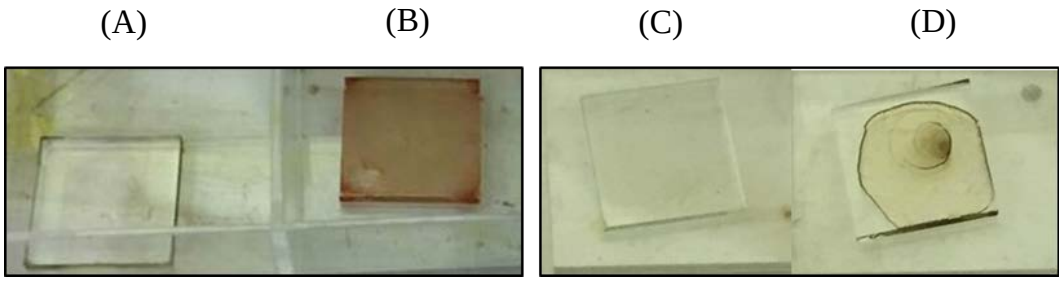

Figure 7.14 (A) CdSe quantum dot (QD) film washed by toluene. (B) TMA-treated CdSe QD film washed by toluene. (C) PbS QD film washed by toluene. (D) TMA-treated PbS QD film washed by toluene.

To further verify the role of ligands in this crosslinking process, we attempted to wash-off TMA-treated oleic acid and oleylamine (i.e. no nanocrystals) with toluene. We show in Figure 7.13 that the ligands were crosslinked and insoluble upon TMA treatment, hence confirming that the ligands are chemically incorporated into the alumina network across the entire nanocrystal film. In order to prove the generality of our crosslinking technique, we treated thin films of CdSe and PbS nanocrystals with TMA, and demonstrate them to be insoluble to organic solvents upon treatment (see Figure 7.14). We note here, more details of this passivation and crosslinking treatment yet to be clear in our further work e.g. how much percentage of ligands are actually ripped off from nanocrystal surface and in what structure are aluminum attached to nanocrystals.

7.5 Device Performance

The TMA crosslinking method has enabled us to make high-performance light-emitting devices using these nanocrystalline lead halide perovskites. Figure 7.15 (A) to (D) shows the detailed device characteristics of our perovskite nanocrystal LEDs. High luminance levels of 2335 and 1559 cd m^{-2} were achieved in our green and orange-emitting devices, respectively, at current densities of 831 and 852 mA cm^{-2}. As shown in Figure 7.15 (B), charge injection turns on efficiently close to the bandgap voltage of the perovskite. To demonstrate the importance of our crosslinking method, we plotted the current-voltage characteristics of the non-TMA-treated $CsPbI_3$ device, and show that the current density is more than an order of magnitude higher than the crosslinked counterpart, even at similar or lower luminance levels. This is a

clear indication of current leakage [21], which is a result of voids created from the wash-off of the perovskite nanocrystals.

We achieved remarkable external quantum efficiencies (EQE), as high as 5.7%, in the crosslinked red-emitting $CsPbI_3$ device, more than an order of magnitude higher than the non-crosslinked device (see Figure 7.15 (C)). Correcting for out-coupling losses, We used the relation $IQE=2n^2$ EQE to calculation the IQE [22]. We chose the refractive index of glass to be 1.5 and assume light to be isotopically emitted to the glass substrate. The internal quantum efficiency is calculated to be approximately 26%.We note that our $CsPbI_3$ device emits at 698 nm, close to the edge of human eye sensitivity, and therefore gives only a modest luminance level of 206 cd m^{-2} at a current density of 755 mA cm^{-2}. We observed that the EQE of the nanocrystal devices decrease generally with the widening of the perovskite bandgap. This is in line with the trends of a lower PLQE in our green and blue-emitting materials (see Figure 7.15 (B)). The less-ideal charge injection into larger bandgap perovskites could also result in the lower device efficiencies. Figure 7.15 (D) gives a summary of the key performance parameters of our nanocrystal LEDs.

During our investigation of the mixed-halide perovskite nanocrystals ($CsPbI_{2.25}Br_{0.75}$ and $CsPbBr_{1.5}Cl_{1.5}$), we noticed that their emission red-shifts during device operation, and return slowly towards their original state after resting (Figure 7.16). This emission shift is not observed in the pure halide samples. This may be related to previous observations on photoluminescence shifts in mixed-halide perovskites upon photo-excitation, which was suggested to be due to phase segregation into purer halide phases [23]. We note that our films consist of spatially-separated nanocrystals, and any phase segregation or halide rearrangements could therefore occur only within a small domain of less than 20 nm. We further show in Figure 7.16 that the EL shifts are completely consistent with the PL shifts, thereby confirming that these shifts are a result of intrinsic changes within the perovskites, and not due to a change in the device charge injection properties during operation.

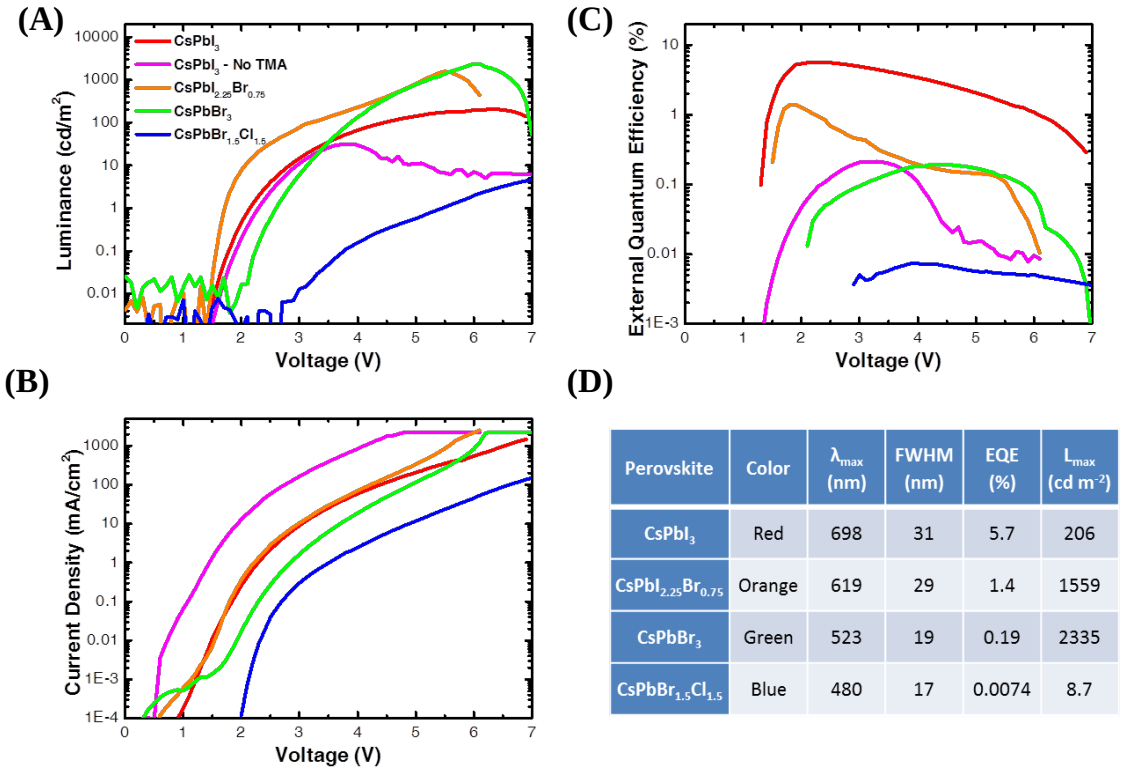

Perovskite	Color	λ_{max} (nm)	FWHM (nm)	EQE (%)	L_{max} (cd m^{-2})
$CsPbI_3$	Red	698	31	5.7	206
$CsPbI_{2.25}Br_{0.75}$	Orange	619	29	1.4	1559
$CsPbBr_3$	Green	523	19	0.19	2335
$CsPbBr_{1.5}Cl_{1.5}$	Blue	480	17	0.0074	8.7

Figure 7.15 (A) Luminance vs. voltage plots of perovskite nanocrystal LEDs. (B) Current density vs. voltage plots of perovskite nanocrystal LEDs. (C) External quantum efficiency vs. voltage plots of perovskite nanocrystal LEDs. (D) Table of summary of perovskite nanocrystal LED performance.

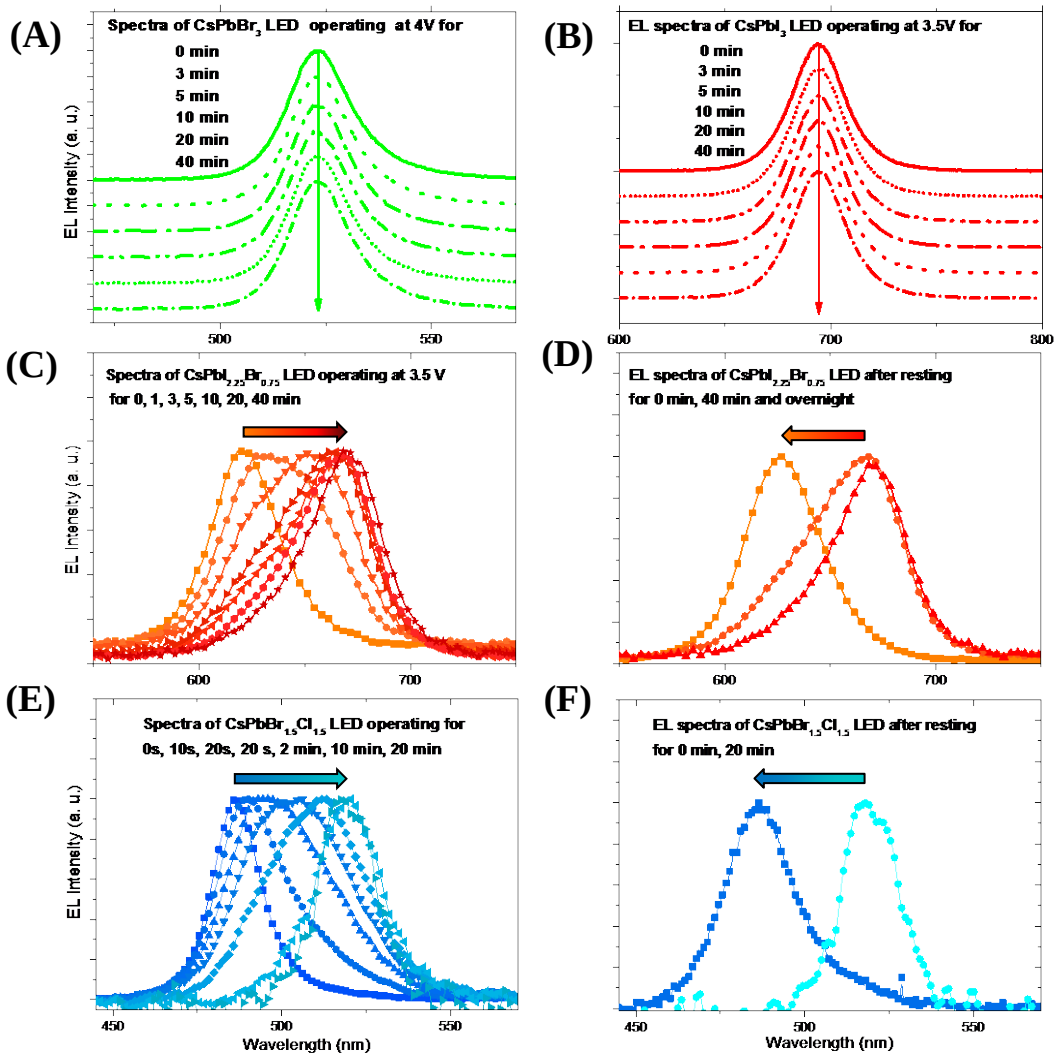

Figure 7.16 The evolution of EL spectra over operation time. (A) EL spectra of $CsPbBr_3$ LED operated at 4 V. (B) EL spectra of a $CsPbI_3$ LED operated at 3.5 V. (C) EL spectra of $CsPbI_{2.25}Br_{0.75}$ LED operated at 3.5 V, showing a gradual red-shift. (D) EL spectra of $CsPbI_{2.25}Br_{0.75}$LED after resting, showing a reversal of the red-shift. (E) EL spectra of $CsPbBr_{1.5}Cl_{1.5}$LED operated at 5.5 V, showing a gradual red-shift. (F) EL spectra of$CsPbBr_{1.5}Cl_{1.5}$ LED after resting, showing a reversal of the red-shift.

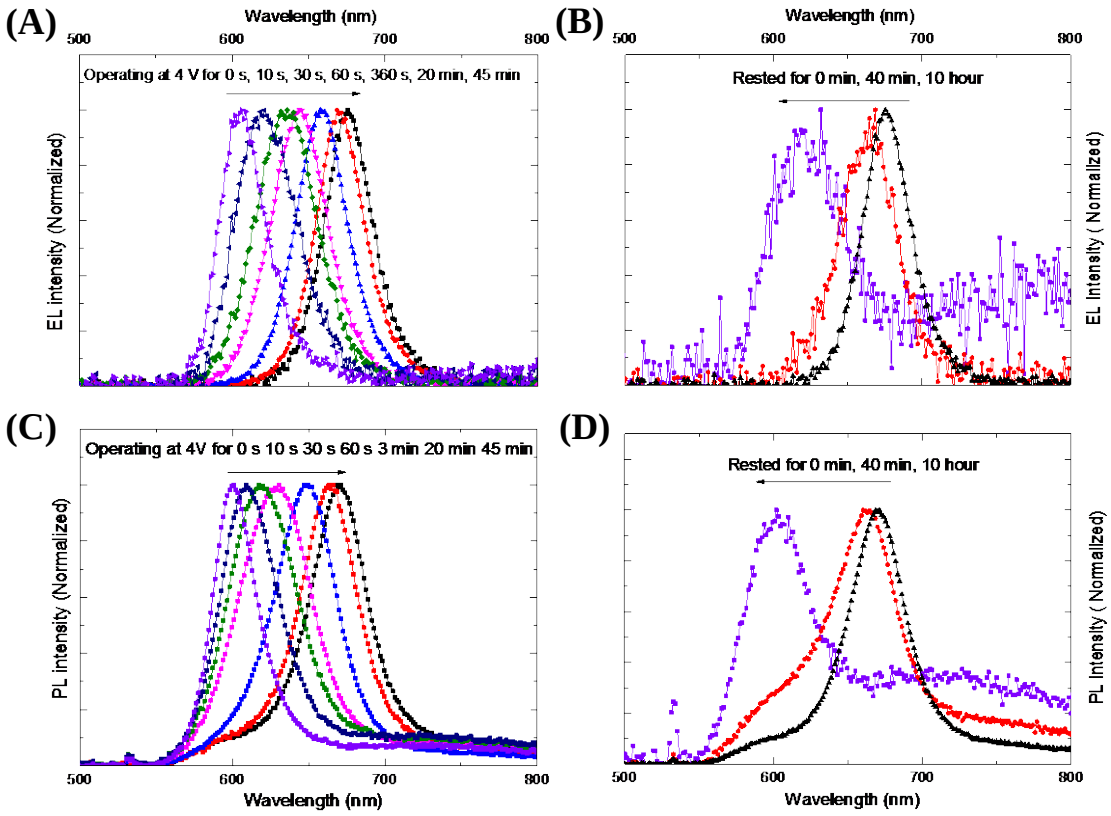

Figure 7.17 Comparison of EL and PL spectra of $CsPbI_{2.25}Br_{0.75}$within the same time window during the LED operation (EL and PL spectra were taken alternatively using the same optical setup) (A) EL spectra of LED, showing a gradual red-shift over time. (B) EL spectra of LED after resting, showing a reversal of the red-shift. (C) PL spectra of the LED, showing a consistent red-shift with the EL. (D) PL spectra of the LED after resting, showing a consistent reversal of the red-shift. The device pixels were photo-excited with a 532 nm CW laser during PL measurements. The laser peak is filtered off with an optical long-pass filter.

7.6 Conclusion and discussion

We have shown a new crosslinking method with TMA vapour solved the washing-off problem to solution-process the newly emerging perovskite nanoparticle material and certainly will be helpful to solve problems in nanoparticle system alike such as CdSe and PbSe quantum dots. The method is also tested to be extendable to other gases such as diethylznic.

Chemically compatibility of TMA vapour to surfaces of the Br- and the I- based perovskite enables the maintain or enhancement of PLQE, yielding a best value of ~85% in TMA treated $CsPbI_3$ quantum dot films.

Based on this method we successfully fabricated full-colour perovskite nanocrystal light-emitting diodes with best EQE above 5%, which are to the date best-performing perovskite nano-crystal LEDs.

We first found that mixed halide perovskite nanocrystal LED exhibits instability on emission spectrum over operation time, which might indicates structural change (such as halide migration and lattice strain) under the electrical injection or under electrical field. Clarification of the mechanism by X-ray technique is under way. This instability might hinder the mixed halide perovskite LEDs toward commercial use, and new material chemistry is yet expected to solve this problem.

References

1. Li, G., Rivarola, F.W.R., Davis, N.J., Bai, S., Jellicoe, T.C., de la Peña, F., Hou, S., Ducati, C., Gao, F., and Friend, R.H., *Highly Efficient Perovskite Nanocrystal Light-Emitting Diodes Enabled by a Universal Crosslinking Method.* Advanced Materials(2016). DOI: 10.1002/adma.201600064
2. Murray, C.B., Norris, D.J., and Bawendi, M.G., *Synthesis and characterization of nearly monodisperse CdE (E = sulfur, selenium, tellurium) semiconductor nanocrystallites.* Journal of the American Chemical Society, **115**, 8706-8715(1993).
3. Murray, C.B., Kagan, C.R., and Bawendi, M.G., *Synthesis and Characterization of Monodisperse Nanocrystals and Close-packed Nanocrystal Assemblies.* Annual Review of Materials Science, **30**, 545-610(2000).
4. Colvin, V.L., Schlamp, M.C., and Alivisatos, A.P., *Light-emitting diodes made from cadmium selenide nanocrystals and a semiconducting polymer.* Nature, **370**, 354-357(1994).
5. Coe, S., Woo, W.-K., Bawendi, M., and Bulovic, V., *Electroluminescence from single monolayers of nanocrystals in molecular organic devices.* Nature, **420**, 800-803(2002).
6. Mashford, B.S., Stevenson, M., Popovic, Z., Hamilton, C., Zhou, Z., Breen, C., Steckel, J., Bulovic, V., Bawendi, M., Coe-Sullivan, S., and Kazlas, P.T., *High-efficiency quantum-dot light-emitting devices with enhanced charge injection.* Nat Photon, **7**, 407-412(2013).
7. Dai, X., Zhang, Z., Jin, Y., Niu, Y., Cao, H., Liang, X., Chen, L., Wang, J., and Peng, X., *Solution-processed, high-performance light-emitting diodes based on quantum dots.* Nature, **515**, 96-99(2014).
8. Shirasaki, Y., Supran, G.J., Bawendi, M.G., and Bulovic, V., *Emergence of colloidal quantum-dot light-emitting technologies.* Nat Photon, **7**, 13-23(2013).
9. Rossetti, R., Hull, R., Gibson, J.M., and Brus, L.E., *Excited electronic states and optical spectra of ZnS and CdS crystallites in the ≈15 to 50 Å size range: Evolution from molecular to bulk semiconducting properties.* The Journal of Chemical Physics, **82**, 552-559(1985).

10. Protesescu, L., Yakunin, S., Bodnarchuk, M.I., Krieg, F., Caputo, R., Hendon, C.H., Yang, R.X., Walsh, A., and Kovalenko, M.V., *Nanocrystals of Cesium Lead Halide Perovskites ($CsPbX_3$, X= Cl, Br, and I): Novel Optoelectronic Materials Showing Bright Emission with Wide Color Gamut.* Nano letters, 15, 3692-3696(2015).

11. Yakunin, S., Protesescu, L., Krieg, F., Bodnarchuk, M.I., Nedelcu, G., Humer, M., De Luca, G., Fiebig, M., Heiss, W., and Kovalenko, M.V., *Low-threshold amplified spontaneous emission and lasing from colloidal nanocrystals of caesium lead halide perovskites.* Nat Commun, **6**, 8065(2015).

12. Wang, J., Wang, N., Jin, Y., Si, J., Tan, Z.K., Du, H., Cheng, L., Dai, X., Bai, S., and He, H., *Interfacial Control Toward Efficient and Low-Voltage Perovskite Light-Emitting Diodes.* Advanced Materials, **27**, 2311-2316(2015).

13. Noh, J.H., Im, S.H., Heo, J.H., Mandal, T.N., and Seok, S.I., *Chemical Management for Colorful, Efficient, and Stable Inorganic–Organic Hybrid Nanostructured Solar Cells.* Nano letters, **13**, 1764-1769(2013).

14. Hwang, J., Kim, E.-G., Liu, J., Brédas, J.-L., Duggal, A., and Kahn, A., *Photoelectron Spectroscopic Study of the Electronic Band Structure of Polyfluorene and Fluorene-Arylamine Copolymers at Interfaces.* The Journal of Physical Chemistry C, **111**, 1378-1384(2007).

15. Cho, K.-S., Lee, E.K., Joo, W.-J., Jang, E., Kim, T.-H., Lee, S.J., Kwon, S.-J., Han, J.Y., Kim, B.-K., Choi, B.L., and Kim, J.M., *High-performance crosslinked colloidal quantum-dot light-emitting diodes.* Nat Photon, **3**, 341-345(2009).

16. Ehrler, B., Walker, B.J., Böhm, M.L., Wilson, M.W.B., Vaynzof, Y., Friend, R.H., and Greenham, N.C., *In situ measurement of exciton energy in hybrid singlet-fission solar cells.* Nat Commun, **3**, 1019(2012).

17. Chang, T.-W.F., Maria, A., Cyr, P.W., Sukhovatkin, V., Levina, L., and Sargent, E.H., *High near-infrared photoluminescence quantum efficiency from PbS nanocrystals in polymer films.* Synthetic Metals, **148**, 257-261(2005).

18. Kagan, C.R., Murray, C.B., Nirmal, M., and Bawendi, M.G., *Electronic Energy Transfer in CdSe Quantum Dot Solids.* Physical Review Letters, **76**, 1517-1520(1996).

19. Barkhouse, D.A.R., Pattantyus-Abraham, A.G., Levina, L., and Sargent, E.H., *Thiols Passivate Recombination Centers in Colloidal Quantum Dots Leading to Enhanced Photovoltaic Device Efficiency.* ACS nano, **2**, 2356-2362(2008).

20. Tarte, P., *Infra-red spectra of inorganic aluminates and characteristic vibrational frequencies of AlO4 tetrahedra and AlO6 octahedra.* Spectrochimica Acta Part A: Molecular Spectroscopy, **23**, 2127-2143(1967).

21. Hoye, R.L., Chua, M.R., Musselman, K.P., Li, G., Lai, M.L., Tan, Z.K., Greenham, N.C., MacManus-Driscoll, J.L., Friend, R.H., and Credgington, D., *Enhanced Performance in Fluorene-Free Organometal Halide Perovskite Light-Emitting Diodes using Tunable, Low Electron Affinity Oxide Electron Injectors.* Advanced Materials, **27**, 1414-1419(2015).

22. Greenham, N.C., Friend, R.H., and Bradley, D.D.C., *Angular Dependence of the Emission from a Conjugated Polymer Light-Emitting Diode: Implications for efficiency calculations.* Advanced Materials, **6**, 491-494(1994).

23. Hoke, E.T., Slotcavage, D.J., Dohner, E.R., Bowring, A.R., Karunadasa, H.I., and McGehee, M.D., *Reversible photo-induced trap formation in mixed-halide hybrid perovskites for photovoltaics.* Chemical Science, **6**, 613-617(2015).

Chapter 8

Conclusion and future work

8.1 Photovoltaic cells

We have demonstrated that nano-patterning enables us to use several new material systems for photovoltaic applications, such as PbSe quantum dots, low-band gap polymers and singlet-fission materials.

The future possible work may lie with singlet fission research, which so far suffers from low efficiency in bilayer or bulk heterojunction solar cells. Our patterning methods will possibly enable high EQE in pentacene or TIPS-pentacene solar cells.

8.2 Light-emitting diodes

In this thesis, we have shown that

- Perovskite is compatible with a dielectric polymer and forms continuous film by spin-coating the perovskite/polymer blend solution. The perovskite nanocrystals formed in the polymer matrix exhibit excellent electroluminescence properties.
- Composite films prepared from perovskite/alumina nanoparticle blend solutions have higher PLQE and longer lifetime than perovskite-only films, which is caused by the confinement effect in the perovskite nanocrystals that formed in the alumina matrix.
- TMA treatments are able to crosslink $CsPbX_3$ nanocrystal films, and also lead to

enhanced PLQEs in $CsPbBr_3$ and $CsPbI_3$ nanocrystal films.

- Full-colour perovskite nanocrystal LEDs can be realised, with the highest EQE above 5% in a $CsPbI_3$ LED.

Future work may lie in the following directions:

- Spectroscopy study of the perovskite nanocrystal LEDs:
  1. Transient electroluminance study.
  2. In-situ PLQE studies of the active layer under operation in a device.
  3. In-situ TCSPC studies of the active layer under operation in a device.
  4. Life time and luminance mapping of the device to examine the EL uniformity.
- Device engineering of the perovskite nanocrystal LED:
  1. Optimize the electron- and hole- transport layer.
- Structural and spectral instability studies on mixed halide perovskites:
  1. Use synchrotron X-rays to analyse the structural change in mixed halide perovskite under illumination and charge injection.

List of publications generated from the thesis

1. Efficient Light-Emitting Diodes Based on Nanocrystalline Perovskite in a Dielectric Polymer Matrix

Guangru Li, Zhikuang Tan, Dawei Di, May Ling Lai, Jonathan Hua-wei Lim, Richard H Friend, Neil C Greenham*

Nano letters 15 (4), 2640-2644, 2015

2. Highly-Efficient Perovskite Nanocrystal Light-Emitting Diodes Enabled by a Universal Cross-linking Method

Guangru Li, Nate J. L. K. Davis, Florencia Wisnivesky Rocca Rivarola, Bai Sai, Tom C. Jellico, ShaocongHou, Francisco de la Peña, Caterina Ducati, Feng Gao, Richard H. Friend Neil C. Greenham* , and Zhi-Kuang Tan*

Advanced Materials DOI: 10.1002/adma.201600064 16 March 2016

3. Size-dependent Photon Emission from Organometal Halide Perovskite Nanocrystals Embedded in an Organic Matrix

Dawei Di*, Kevin P Musselman, ***Guangru Li***, AdiSadhanala, Yulialeskaya, Qilei Song, Zhi-Kuang Tan, May Ling Lai, Judith L MacManus-Driscoll, Neil C Greenham, Richard H Friend*.

The journal of physical chemistry letters 6 (3), 446-450, 2015

4. Enhanced Performance in Fluorene-Free Organometal Halide Perovskite Light-Emitting Diodes using Tunable, Low Electron Affinity Oxide Electron Injectors

Robert LZ Hoye, Matthew R Chua, Kevin P Musselman, ***Guangru Li***, May-Ling Lai, Zhi-Kuang Tan, Neil C Greenham, Judith L MacManus-Driscoll, Richard H Friend, Dan Credgington*.

Advanced Materials 27 (8), 1414-1419, 2015

5. Electroluminescent Device

*UK Patent Application No. 1421133.8 (*28, Nov, 2014)

6. Perovskite Quantum Dot Phosphor

UK Patent Application No. 1519269.3, (30, Oct, 2015)

(Cognation Patent filing: Perovskite Quantum Dot Phosphor *UK Patent Application No. 1511490.3,* (30, June, 2015))

Submitted:

1. **Lead-Free Perovskite Light-Emitting Diodes WithTunable Near-Infrared Emission**

May Ling Lai, Timothy Tay, Aditya Sadhanala, Sian Dutton, ***Guangru Li***, Zhi-Kuang Tan*, Richard H. Friend